Estimation of Bluff Body Transient Aerodynamic Loads Using an Oscillating Model Rig

by

S. Mansor

A Doctoral Thesis

Submitted in partial fulfillment of the requirement for the award
Doctor of Philosophy of Loughborough University

April 2006

Dedication

To my Family .....

Abstract

A method for the estimation of transient aerodynamic data from dynamic wind tunnel tests has been developed and employed in the study of the unsteady response of simple automotive type bodies. The experimental setup consists of the test model mounted to the oscillating model facility such that it is constrained to oscillate with a single degree of freedom of pure yawing motion. The yaw position is recorded from a potentiometer and the time response provides the primary measurement. Analysis of the wind-off and wind-on response allows the transient aerodynamic loads to be estimated. The frequency of oscillation, (synonymous with the frequency of disturbing wind input) is modified by altering the mechanical stiffness of the facility.

The effects of Reynolds number and oscillation frequency are considered and the model is shown to exhibit damped, self-sustained and self-excited behaviour. The transient results are compared with a quasi-steady prediction based on conventional tunnel balance data and presented in the form of aerodynamic magnification factor. The facility and analysis techniques employed are presented and the results of a parametric study of model rear slant angle and of the influence of C-pillar strakes is reported. The results are strongly dependent on shape but for almost all rear slant angles tested the results show that the transient response exceeds that predicted from steady state data. The level of unsteadiness is also significantly influenced by the rear slant angles. The addition of C-pillar strakes is shown to stabilise the flow with even small strakes yielding responses below that of steady state.

From the simulation results the self-sustained oscillation is shown to occur when the aerodynamic damping cancels the mechanical damping. The unsteadiness in the oscillation can be simulated by adding band-limited white noise with an intensity close to that of the turbulence intensity found in the wake. From vehicle crosswind simulation results the aerodynamic yaw moment derivative and its magnification factor are shown to be the important parameters influencing the crosswind sensitivity and path deviation.

Acknowledgements

List of Contents

List of Figures

List of Tables

Nomenclature

A	- model frontal area	m^2
As	- model side area	m^2
C_a	- aerodynamic damping	$Nms.rad^{-1}$
CD	- aerodynamic drag coefficient	
cg	- centre of gravity	
Cn	- aerodynamic yaw moment coefficient	
cp	- centre of pressure	
C_r	- mechanical damping	$Nms.rad^{-1}$
Cy_β	- aerodynamic side force derivative	rad^{-1}
Cy_r	- aerodynamic side force damping derivative	rad^{-1}
Cn_β	- aerodynamic yaw moment derivative	rad^{-1}
Cn_r	- aerodynamic yaw damping derivative	rad^{-1}
Cy	- aerodynamic side force coefficient	
f	- oscillation frequency	Hz
f_n	- natural frequency	Hz
f_d	- damped frequency	Hz
I_{zz}	- model rig yaw moment of inertia	$kg.m^2$
K_a	- aerodynamic stiffness	$Nm.rad^{-1}$
K_m	- reduced frequency	
K_r	- mechanical stiffness	$Nm.rad^{-1}$
Krf	- front wheel cornering stiffness	$N.rad^{-1}$
Krr	- rear wheel cornering stiffness	$N.rad^{-1}$
K_s	- linear spring stiffness	Nm^{-1}
ℓ	- model characteristic length	m
ℓcp	- distance between cp and cg	m
ℓwb	- wheel base length	m
ℓf	- distance between front axle to cg	m
ℓr	- distance between rear axle to cg	m
m	- mass of the model	kg
N_β	- aerodynamic yaw moment stiffness	$Nm.rad^{-1}$
$N_{\beta c}$	- chassis yaw moment stiffness	$Nm.rad^{-1}$
$\hat{N}_\beta$	- dynamic normalised aerodynamic stiffness	$Nm.rad^{-1}/kg.m^2$
N_a	- aerodynamic yaw moment	Nm
N_r	- aerodynamic yaw moment damping	$Nms.rad^{-1}$
N_{rc}	- chassis yaw moment damping	$Nms.rad^{-1}$
$\hat{N}_r$	- dynamic normalised aerodynamic damping	$Nms.rad^{-1}/kg.m^2$
r	- yaw rate	$rad\ s^{-1}$
r_{max}	- maximum yaw rate	$rad\ s^{-1}$
$r_{(t=1s)}$	- yaw rate after 1 second	$rad\ s^{-1}$
r_f	- yaw rate disturbance	$rad\ s^{-1}$

St	- Strouhal number	
N_f	- yaw moment fluctuation	Nm
T	- period of oscillation frequency of wind-on	s
$t_{1/2}$	- time to half amplitude of wind-on	s
T_o	- period of oscillation of wind-off	s
$t_{1/2_o}$	- time to half amplitude of wind-off	s
$t_{(r\,max)}$	- time at maximum yaw rate	s
u, v, w	- forward, lateral and vertical speed	m.s^{-1}
V	- wind tunnel velocity	m.s^{-1}
V_x	- wind tunnel axial velocity	m.s^{-1}
V_y	- wind tunnel lateral velocity	m.s^{-1}
V_z	- wind tunnel vertical velocity	m.s^{-1}
V_f	- lateral velocity fluctuation	m.s^{-1}
V_w	- crosswind velocity	m.s^{-1}
Y_β	- aerodynamic side force stiffness	N.rad^{-1}
$Y_{\beta c}$	- chassis side force stiffness	N.rad^{-1}
Y_r	- aerodynamic side force damping	Ns.rad^{-1}
Y_{rc}	- chassis side force damping	Ns.rad^{-1}
β	- model yaw angle	deg
$\dot{\beta}$	- model yaw velocity	deg/s
$\ddot{\beta}$	- model yaw acceleration	deg/s^2
β_f	- yaw angle fluctuation	deg
β_w	- relative crosswind angle	deg
ρ	- air density	kg.m^{-3}
θ	- model angle of rotation	deg
ϕ	- phase angle	deg
ψ	- crosswind angle with respect to vehicle forward speed	deg
ζ	- damping ratio	
ω	- oscillation frequency	rad.s^{-1}
ω_d	- damped frequency	rad.s^{-1}
ω_n	- natural frequency	rad.s^{-1}

rms	- root means square (RMS)	
psd	- power spectral density (PSD)	unit^2/Hz
pdf	- probability density function (PDF)	

Chapter 1

Introduction

1.1 Overview

The transient or unsteady aerodynamic forces and moments applied to road vehicles have been the subject of investigation for many years due to the associated implications on vehicle safety and refinement. One area that has received considerable attention over recent years is the measurement of transient aerodynamic forces and moments in yawed conditions. This has been particularly important because the development of streamlined or low drag car bodies, that satisfy demands for good fuel economy, has tended to result in cars with increased sensitivity to crosswind disturbances. This additional sensitivity arises because the drag reduction techniques have generally involved rounding off the front end profiles and the region around the rear pillar. In the presence of crosswinds this can give rise to differences between front and rear side force and hence generate significant yaw moments that tend to destabilise the vehicle.

Where the aerodynamic loads are sufficient to cause path deviation the effects can be limited through good suspension design or even, more recently, with active steering control. However the loads are dealt with, a full understanding of the aerodynamic inputs can only serve to improve the control. Under unsteady conditions the added

body curvature in low drag designs can also lead to uncertain and variable flow separation, resulting in unsteady aerodynamic loads. Though these loads may not destabilise the vehicle sufficiently to cause path deviation they can lead to a feeling of poor refinement, characterised as buffeting. These effects cannot be readily controlled through an active approach and so a full understanding is of concern to the vehicle manufacturer.

The effects of aerodynamic forces and moments on driving stability are most noticeable in crosswind or side wind gust scenarios. In such conditions the forces and moments can fluctuate influencing the vehicle's directional stability and controllability. The lift force and pitching moments have an impact in determining the controllability even in the absence of crosswind and are particularly important for high performance race cars. Side force, yaw moment and to some degree roll moment are important to the safety and comfort of passenger cars. However, for passenger cars the side force and yaw moments are known to be the primary concerns in crosswind aerodynamics.

The side force and yaw moment aerodynamic data is usually given in the form of aerodynamic coefficients. For stability analysis it is convenient to then represent these coefficients in terms of derivatives, Hucho and Emmelmann [31], given by the gradient of the coefficient with respect to yaw angle (i.e. the rates at which the coefficients vary with yaw angle).

Conventionally, vehicle dynamic simulation has used a quasi-steady estimation of the aerodynamic input to provide an estimate of transient loads. However, aerodynamic refinement has now reached a stage that it is believed that the transient effects may in some instances be significant, for example in high-speed manoeuvres or during crosswind gust situations. The requirement to provide accurate aerodynamic data is increasing and becoming very important in the prediction of the vehicle dynamic response to unsteady aerodynamic loads.

There is clearly a need to improve our understanding of the unsteady case and for the development of techniques to measure and quantify a vehicle's susceptibility to crosswind inputs at an early stage in the vehicle development process. The complexity

associated with crosswind stability is reflected by the number of tests and evaluation methods found in the literature.

At full scale two main sources of information are commonly available. Steady state tunnel tests (Figure 1.1) conducted at yaw generate useful initial data but there is insufficient evidence at present to adequately correlate this with performance in a transient situation.

Figure 1.1 Vehicle in MIRA's full-scale wind tunnel, [41].

Figure 1.2 shows steady-state results of side force and yaw moment coefficients obtained from a full-scale wind tunnel test of three passenger cars. All three cars show that the side force and yaw moment coefficients vary linearly with yaw angle. The results may be used to make comparison between vehicles but do not necessarily provide any insight into the true transient behaviour.
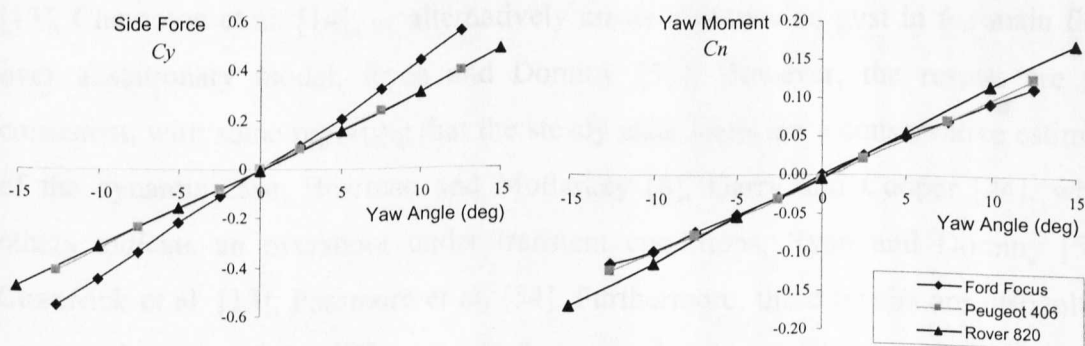
Figure 1.2 Steady-state side force and yaw moment versus yaw angle from MIRA's full-scale tunnel.

Alternatively, the transient crosswind sensitivity can be measured by driving the full scale vehicle through an artificial gust generated by a collection of fans or jets (refer to Figure 1.3).
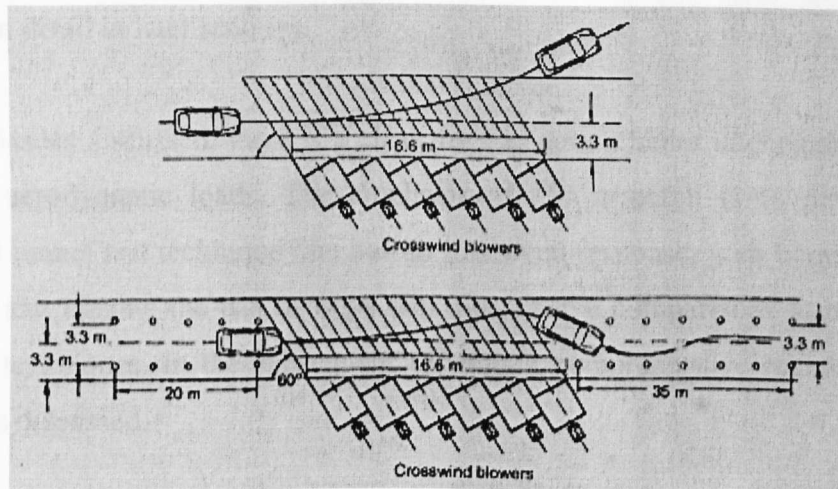
Figure 1.3 Assessment of crosswind sensitivity. Driving speed 36 m/s, side wind 22 m/s, Hucho [30].

During the test the crosswind performance can be assessed by simply considering the lateral deviation, or through more complete measurements of lateral acceleration, yaw rate etc. The disadvantage of the method is that it cannot be performed until a stage in the vehicle development process when it is too late to implement the appropriate changes.

A number of authors have reported work that attempts to simulate transient conditions using scale model wind tunnel tests. These include techniques that oscillate the flow over a stationary model, Bearman and Mullarkey [8], Passmore et al. [54]; move the model in steady flow, Garry and Cooper [24], Macklin et al. [42], Chadwick et al. [13], Chemoton et al. [14]; or alternatively create a crosswind gust in the main flow over a stationary model, Ryan and Dominy [59]. However, the results are not consistent, with some reporting that the steady state loads are a conservative estimate of the dynamic case, Bearman and Mullarkey [8], Garry and Cooper [24], while others indicate an overshoot under transient conditions, Ryan and Dominy [59], Chadwick et al. [13], Passmore et al. [54]. Furthermore, these results are difficult to compare because of the differences in the type of tests, models, the approach to the analysis and the method of presenting the results. One of the recurrent problems with many of these methods is the signal to noise ratio, especially with moving models. In many cases the measurement noise can be reduced with stationary models by introducing oscillating flow or an additional gust from a jet. However the signal to

noise ratio may remain poor if the gust amplitude is not large. All of these techniques are reviewed in detail in later sections.

Based on the issues discussed, there is a clear need to gain a better understanding of the unsteady aerodynamic loads. The emphasis of this research is to develop a dynamic wind tunnel test technique that has an improved response, with better signal to noise ratio and operate the test in ways that allow some comparisons to be made with existing techniques. In the subsequent sections a comprehensive review of all areas related is discussed.

1.2 Unsteady Aerodynamics

Moving vehicles are subject to unsteady wind inputs arising from ambient wind, the interaction of ambient wind with the topology and the presence of other vehicles. Because of the bluff body shape of the vehicles the aerodynamic characteristics are strongly influenced by flow separation. The majority of the flow fields are in the form of wakes, vortices and turbulent buffeting. The characteristic and the interaction of the flow characteristics with the vehicle motion makes the study of the unsteady aerodynamics very complex.

The variety of unsteady flows is large, and includes transient regimes, impulsive starts, manoeuvring, periodic flow, and flows that are intrinsically unsteady because of the mechanism of vortex shedding from bluff bodies, Fillipone [21], [22]. In many practical cases the vortex shedding is the dominant contributor to the unsteady aerodynamics.

For road vehicles a crosswind is the primary source of the asymmetrical flows that deflect a vehicle from its intended path. In real life, the crosswind is actually unsteady or gusty wind. The moving vehicle under gusty wind may experience random changes in the magnitudes and directions (vectors) of the resultant winds. A number of researchers have attempted to simulate these aerodynamic inputs in the wind tunnel. However the use of wind tunnels to simulate the transient or unsteady aerodynamics is still not an established technique.

1.2.1 Flow Induced Oscillation

In general wind tunnel models experience unsteadiness associated with turbulence and vortex shedding in the wake flow. When a rigid bluff body model is mounted elastically in the wind tunnel, as the air flows over the body, two kinds of excitations are generally admitted, the first is due to the vortex shedding, and the second is an induced oscillation arising from the movement of the model, known as galloping. Induced oscillation can be treated as self-excited wind forces and the wind tunnel model will normally experience a self-sustained oscillation. In the situation of very low damping the excitation is due to the random effect of turbulent flow.

The unsteady wake behind a bluff body is an example of flow subject to this type of phenomenon. The term 'bluff' most commonly refers to bodies where their aerodynamic characteristics are strongly influenced by flow separation. The major contribution to the aerodynamic forces is generated from the low pressure in the wake of the body. This creates interest in the investigation of the wake dynamics as the source of force due to pressure differences. The wake dynamics depend highly on the Reynolds number. While the wake is steady for very small Reynolds numbers, laminar vortex shedding occurs for intermediate Reynolds numbers, and the wake becomes turbulent at high Reynolds numbers. Accordingly, the forces vary depending on the wake dynamics. Siegel [63] suggested that for a given Reynolds number, however, the wake dynamics can be altered, for example, by changing the geometry of the body.

1.2.2 Strouhal-Reynolds Number and Vortex Shedding

The phenomenon of vortex shedding from bluff bodies has been studied since the pioneering work of Strouhal and von Karman in the mid 1800's. Usually the studies involve tests on cylinders or spheres at very low speed and the vortex shedding is clearly defined. At higher speed the oscillation phenomenon exhibits fully turbulent and periodic characteristics. A unique relationship exists between Reynolds number and a dimensionless parameter involving the shedding frequency. This parameter, known as the Strouhal number, is the non-dimensional parameter defining the similitude of periodic flows, and it is defined as,

$$St = \frac{f\,\ell}{V}$$ (1.1)

where f is the vortex shedding frequency in Hertz, ℓ is the bluff body characteristic length and V is the mean free stream velocity.

Periodic vortex shedding remains a characteristic of the flow across a very wide range of Reynolds numbers. For a circular cylinder (Figure 1.4), Strouhal number is almost constant at $St \approx 0.21$ in the Reynolds number range of $400 < Re < 3\text{x}10^5$. At higher Reynolds numbers, of $3\text{x}10^5 < Re < 3\text{x}10^6$, the laminar boundary layer has undergone turbulent transition and wake is narrower and disorganised, and for $Re > 3\text{x}10^6$ the shedding frequency becomes discernible again, Lienhard [40], Blevin [11]. The Reynolds number ranges in Figure 1.4 are only approximate, as they depend on the free stream turbulence and surface roughness.
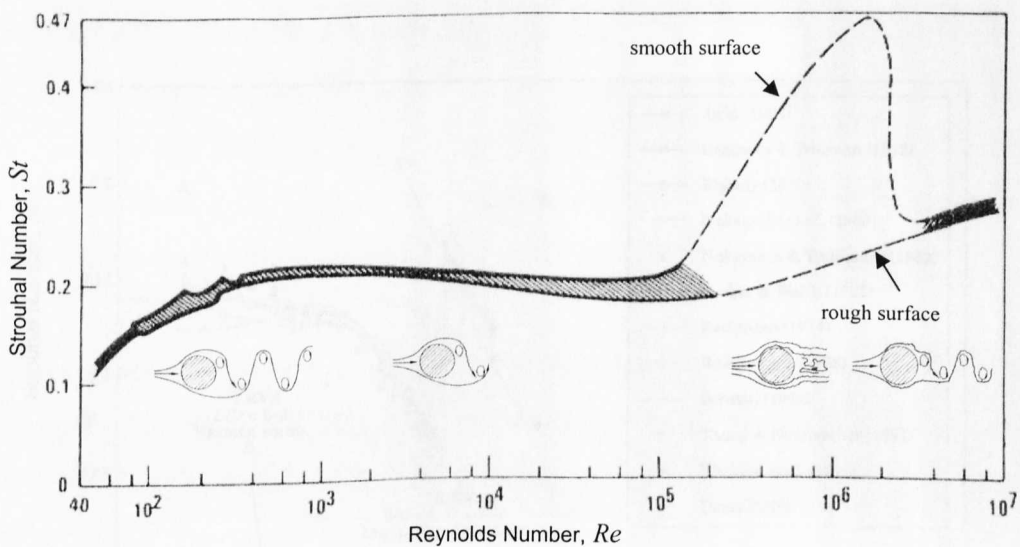
Figure 1.4 The Strouhal-Reynolds number relationship for circular cylinder, Lienhard [40], Blevin [11].

In the wake of almost all two-dimensional bluff bodies, the formation of a von-karman vortex street can be observed for a wide range of Reynolds numbers. For three-dimensional bluff bodies, however, this is not the case. Instead, investigations indicate the existence of helical vortices in the wake, though only limited understanding of the dynamic behaviour of these wakes seems to exist. Siegel [63] suggested that the complex geometry of these problems makes it difficult to gain an understanding of the underlying physical mechanism.

1.2.3 Vortex Shedding of Rectangular Shape

Rectangular shape vortex shedding is different from that of circular cylinders in that the separation points are fixed at the sharp corners. However, reattachment may occur on high aspect ratio rectangular shapes (i.e. ratio of the length to width of the model).

Several studies have been carried out to examine the vortex shedding and induced oscillation for structural engineering, Blevin [11], Simiu and Scanlan [65]. They were interested in the induced oscillation on a variety of bridges, cables and buildings particularly at low Reynolds number (i.e. less than 10^6). Deniz and Staubli [19] compiled results from a number of vortex shedding experiments with non-oscillating rectangular cylinders of various aspect ratio with low freestream turbulence level (Figure 1.5). For aspect ratios (length/width) of 2-3 the vortex shedding Strouhal number is around 0.05 (based on the thickness of the cross-section).
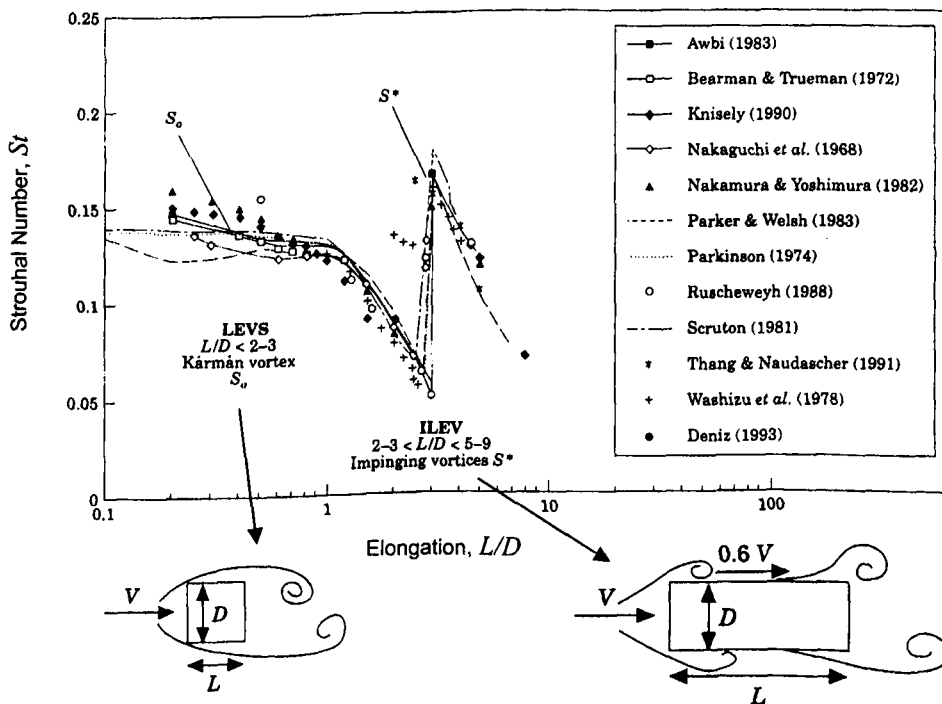
Figure 1.5 Variation of Strauhal number as a function of elongation ratio L/D from rectangular cylinder (LEVS–leading edge vortex shedding, ILEV-impinging leading edge vortices), Deniz and Staubli [19].

Morgenthal and McRobie [47] studied a 'lock-in' oscillation phenomenon which occurred when the vortex shedding frequency was close to the natural frequency of the rectangular cylinders. The induced oscillation of rectangular and square cylinders

in cross flow conditions has been investigated by Hemon and Santi [27], they found in both experimental and numerical work that the aeroelastic behaviour of a rectangular cylinder of aspect ratio two in a cross-flow produced a 'lock-in' Strouhal number of 0.085. Although there is also a relationship between the phase lag and Strouhal number but the correlation remains unclear.

In automotive related work, Khalighi et al. [37] conducted an experimental study of the unsteady wake behind a simple vehicle model at different free-stream velocities. The Reynolds number range in the tests is between 0.8×10^6 and 1.3×10^6. From the measurement of unsteady pressure signals on the model base of a square back they found dominant frequencies for different free-stream velocities that correspond to a Strouhal number of 0.07 (based on model height).

1.2.4 Transient Crosswind Effects

Many investigations of the transient aerodynamics of road vehicles have been published in the last 30 years, they largely deal with the transient aerodynamic forces and moments under crosswind or gust conditions. In addition, some investigations have tried to determine the relevance of these effects to driving stability.

The outcome of a crosswind acting on a car depends on the wind speed and direction, as well as its frequency, resulting from the wave length of the gust and the speed of the car. Howell [32], suggests that for a typical car travelling at motorway speeds, crosswind speeds less than 2.5 m/s may induce wander, up to 10 m/s they can cause buffeting where steering correction may be required, and at over 15 m/s the possibility of the vehicle being pushed out of its lane arises, creating a safety problem.

For typical driving conditions Watkins and Saunders [73] show that spectral results indicate the peak energy to be at approximately 1 Hz but showed that it could vary between 0.25 and 2.5 Hz. At motorway speeds this corresponds to reduced frequencies between approximately 0.09 and 0.9 which is equivalent to a gust wave length of 30 to 3 model lengths respectively. The reduced frequency is defined here as, [68], [22], [10], [23], [8], [54]:

$$Km = \frac{\pi f \ell}{V} \qquad (1.2)$$

If the vehicle is considered to be a simple dynamic system then its reaction to a gust input is maximised if the excitation frequency is close to its fundamental frequency. Goetz [25] divided the excitation frequency into three ranges according to its effect on the vehicle response (Figure 1.6).
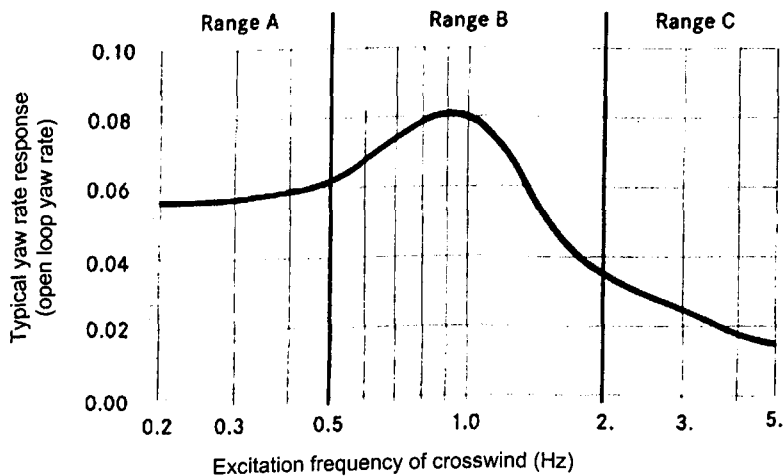
Figure 1.6 Typical car response to crosswind, Goetz [25].

1) Range 0.2 to 0.5 Hz relates to a steady or low frequency crosswind which leads to path deviation.

2) The range 0.5 to 2.0 Hz is most important for driving stability and handling. It is characterised by resonance effects and phase delays because it corresponds to the fundamental frequency of the lateral vehicle dynamics.

3) The frequency range of more then 2.0 Hz is characterised by the response decreasing with frequency. However, the loads may remain important as they effect the vehicle refinement. Within this range aerodynamic loads are noticed by the passengers as buffeting, shaking, or a rapid change of noise, but have little or no impact on path deviation.

The frequency range shown in Figure 1.6 which describes the behaviour and characteristics of response of a vehicle only serves as a simple approximation. In reality, these modes may act simultaneously and they may be coupling.

1.3 Review of Previous Related Tests

The majority of aerodynamic studies on cars have concentrated on the reduction of vehicle drag, to increase fuel efficiency and improve high-speed performance. However, the streamlining of cars to minimize drag leads to an increase in the vehicle's crosswind sensitivity. Steady state or time averaged wind tunnel testing has been used to help aerodynamicists in the estimation of crosswind aerodynamics, but the vehicle might behave differently and sometimes very poorly in transient cases.

Baker and Humphreys [3] present an assessment of the adequacy of various wind tunnel techniques to obtain aerodynamic data for ground vehicles in crosswind and provides some information regarding the viability of unsteady measurements using a moving model rig. In the paper he emphasised the requirement to conduct dynamic tests in order to obtain necessary unsteady data accurately. However in the test using a moving model rig the effect of model mounting on measured data requires further investigation.

Computational methods for determining the steady and unsteady flow field around cars is developing. Tran [69], Yamada and Ito [74], Khalighi et al. [37], Krajnovic and Davidson [39], presented comparisons between the computational and experimental flow field around simplified car-like shapes and showed some degree of agreement. However, it is not likely, in the medium term, to provide useful data for the assessment of crosswind sensitivity. This makes the experimental approach both necessary and very attractive.

The wind tunnel has proven to be the most effective tool to help the aerodynamicists during the development of vehicle shapes. But the use of wind tunnels to simulate the transient phenomenon is still not an established technique.

Macklin et al. [42] divided the methods for assessing the effect of crosswinds on road vehicle into three categories:

1) *Static-static* test – the vehicle is placed in the wind tunnel and force and moment measurements are taken from the static model rotated at various angles relative to the flow.

2) *Static-dynamic* test – the vehicle is placed in the wind tunnel and a gust is simulated either by varying the main gust profile or by using a secondary source and some sort of shutter mechanism.

3) *Dynamic-static* test – the vehicle or model itself is moved and the gust source is kept constant.

1.3.1 Static-static Test

The static or steady state tests are the conventional method to determine the aerodynamic coefficients from a stationary model in steady flow. The effect of a crosswind is made by measuring the forces and moments at various models yaw angles relative to the incoming flow. The aerodynamic derivatives, in this case are simply the gradient of forces and moment versus yaw angle. For example, the side force and yaw moment derivatives are given by:

Side force derivative: $\qquad \dfrac{dCy}{d\beta} = Cy_\beta$

Yaw moment derivative: $\qquad \dfrac{dCn}{d\beta} = Cn_\beta$

Generally, the side force and yaw moment derivatives (i.e. Cy_β and Cn_β) are approximately linear up to $\pm 20°$ yaw for both the squareback, notchback and fastback body shape, Macklin et al. [42]. Steady state wind tunnel tests generate useful initial data but there is insufficient evidence at present to adequately correlate this with transient performance. For an example of the data acquired in such a test refer to Figure 1.2.

1.3.2 Static-dynamic Test

Bearman and Mullarkey [8] generated sinusoidal gusts using oscillating aerofoil sections positioned upstream of the stationary model. The models used were based on those studied by Davis [18] and shown in Figure 1.7. A range of reduced frequencies was achieved by varying the tunnel speed from 10 to 24 m/s for three aerofoil oscillation frequencies of 3 Hz, 11 Hz and 19 Hz. The resulting reduced frequency ranges from 0.15 to 1.75, which is equivalent to wavelengths of 2 to 20 times the model length.
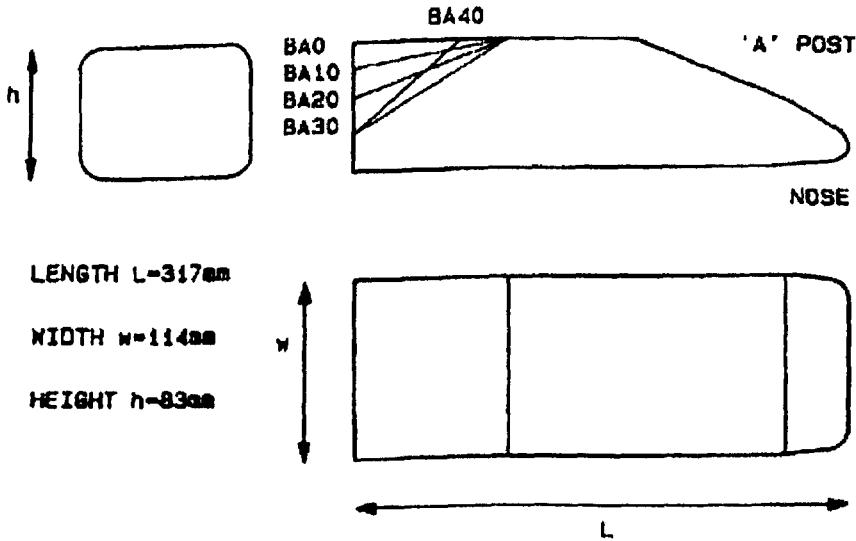
Figure 1.7 Schematic diagram of the model with the various rear end, Bearman and Mullarkey [8].

The static derivatives were measured from a conventional static-static test conducted at 24 m/s (Re= 4.5×10^5). Unsteady measurements of forces and moments using *strain gauges* were used to determine the transient side force and yaw moment. Results are presented in the form of an aerodynamic admittance function $X^2(Km)$ given by the ratio of dynamic power to the power predicted from quasi-steady data:

$$X^2(Km) = \frac{Sn(Km)}{\left(\dfrac{dCn}{d\beta}\right)^2_{qs} S_{\beta g}(Km)} \qquad (1.3)$$

where $Sn(Km)$ and $S_{\beta g}(Km)$ are the power spectral density of the yaw moment and gust amplitude at reduced frequency Km and $\left(\dfrac{dCn}{d\beta}\right)_{qs}$ is steady state gradient.

The experiments produced the unexpected result that at low frequencies the admittance did not appear to tend to unity for either side force or yaw moment. At higher frequencies the side force admittance was always less than unity, but the yaw moment admittance exceeded unity by approximately 12% at reduced frequencies of more than 1.2. Bearman and Mullarkey [8] concludes from the work that in general it is sufficient to make conventional steady state measurements as they provide a conservative estimate of the dynamic loads.

Passmore et al. [54] repeated the method used by Bearman and Mullarkey [8], generating a sinusoidal gust again using oscillating aerofoil sections positioned upstream of a stationary model. But used unsteady measurements of *surface pressure* to determine the transient side force and yaw moment on the same Davis model shape.

A range of reduced frequencies of between 0.09 and 0.71 based on the model length was achieved by varying the aerofoil oscillation frequency at a single tunnel speed of 22 m/s. The blockage ratio and the Reynolds number based on length were 2.3% and 1×10^6 respectively. The results were presented in the form of an aerodynamic magnification $\chi_a(Km)$ calculated by comparing the transient response with quasi-steady prediction as:

$$\chi_a(Km) = \frac{ACx(Km)}{\left(\dfrac{dCx}{d\beta}\right)_{qs} Ag(Km)} \tag{1.4}$$

where $ACx(Km)$ = amplitude at reduced frequency Km of force or moment.

                    $Ag(Km)$ = gust amplitude at reduced frequency Km .

                    $\left(\dfrac{dCx}{d\beta}\right)_{qs}$ = steady state gradient as Km tends to zero.

The transient yaw moment magnification exceeds the quasi-steady result across the frequency range by between 5% and 30%. The transient side force is generally significantly less than the quasi-steady value except at the lowest frequency tested. The trend seen by Bearman and Mullarkey [8], of reducing magnification factor at low reduced frequencies is not seen. In fact both the yaw moment and side force magnifications are well above unity at the lowest frequency tested.

Transient pressure measurement has also been recorded by Ryan and Dominy [59] on a stationary model mounted in an open jet wind tunnel and the gust effect provided from a second open jet at 30° relative incidence. The model shape used by Ryan and Dominy is shown in Figure 1.8.
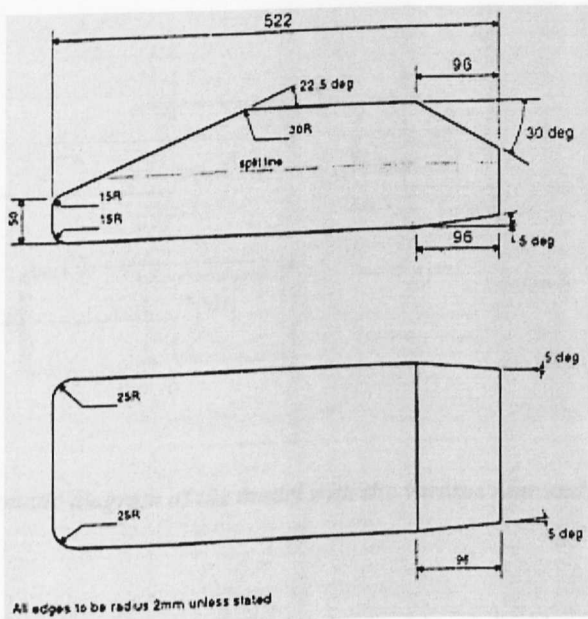
Figure 1.8 Schematic diagram of the model, Ryan & Dominy [59].

The Reynolds number based on model length was 3×10^5. The 3D model results showed that there was an 18% overshoot in the transient sideforce, and no overshoot for the yaw moment coefficient.

1.3.3 Dynamic-static Test

Garry and Cooper [24] oscillated a simplified rectangular prism representing a tractor-trailer model about its vertical axis at steady yaw rates in the range $0.25\,^\circ\,s^{-1}$ to $64^\circ\,s^{-1}$. Tested were conducted at 20 m/s giving a Reynolds number of 0.483×10^6. The dynamic forces and moments were measured using a 3-component *strain gauge balance*. The results showed that the magnitude of the drag, side force and yaw moment coefficients do not change significantly with rotational rates. However the dynamic measured coefficient versus yaw angle curve appears shifted by a phase angle when compared to the static data. The magnitude and sign of this phase shift are seen to be dependent on both yaw rate and model geometry.

Macklin et al. [42] conducted comparisons between static and dynamic coefficients from tests on three basic configurations as shown in Figure 1.9. In this study the model itself moves along a track across a wind tunnel working section.
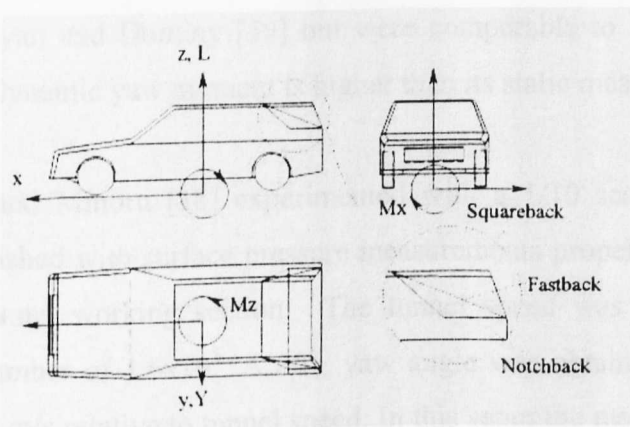
Figure 1.9 Schematic diagram of the model with the various rear end, Macklin, Garry, Howell [42].

The data was presented using an approximated model velocity because during the test the model accelerates across the working section. The Reynolds number varied from 3.4×10^5 at zero yaw, to 4.7×10^5 at $45°$. A 5-component foil *strain-gauged balance* was used to measure the forces and moments. In general data from static tests are shown to compare well with that from the dynamic tests at yaw angles below $15°$, but at higher yaw angles, the dynamic values of the forces and moments became larger than the static values. However side force results showed similar results between the static and dynamic measurements up to about $30°$ yaw, and then the dynamic results continue to rise, whilst the static results tended to a constant value. The yaw moment and roll moment results were plotted for static, mean dynamic and peak dynamic situation. Yaw moment results showed all three cases to be similar up to about $15°$ yaw. However, above this the mean dynamic and static remained similar for square back and fast back, whilst the mean dynamic values were higher than the static case for the notch back. The peak dynamic values were significantly higher for all cases. Roll moment results showed similar values between static and dynamic for notch back, whilst the dynamic results were slightly higher above $35°$ yaw for square back and fast back.

The overshoot in the transient side force and zero overshoot for the yaw moment found by Ryan and Dominy [59] in static-dynamic test is in contrast to the work published by Macklin et al. [42] in which they found, at $30°$ yaw, the static and dynamic side forces were comparable for all shapes. However, the dynamic yaw moments were much increased. The findings of Passmore et al. [54] also oppose the

results of Ryan and Dominy [59] but were comparable to Macklin et al. [42] who agreed that dynamic yaw moment is higher than its static measurement equivalent.

Kobayashi and Minoru [38] experimented with a 1/10 scale model of a one box vehicle furnished with surface pressure measurements propelled along a rail crossing the wind tunnel working section. The tunnel speed was set at 7 m/s to give a Reynolds number of 1.6×10^5. A $30°$ yaw angle was obtained by setting the model velocity at 4 m/s relative to tunnel speed. In this setup the model yaw angle is fixed at $30°$ and it is difficult to compare the transient results with conventional static tests. Kobayashi found that the peak yaw moment on entering a crosswind gust was approximately double that of the constant (steady state) region, a result also noticed by Macklin et al. [42] when applied to a passenger car. Kobayashi and Minoru [38] also found that the increase in front slant angle generally increased the overall yaw moment coefficient.

Chadwick et al. [13] conducted similar tests as in Macklin et al. [42] using the same basic facility. In this test the transient force and surface pressure data was measured on a range of simple geometric shapes at a test speed of approximately 13 m/s (Re=3.5×10^5). The yaw angle varied from $5°$ to $25°$ yaw with $5°$ increment. He found that the edge radiusing of the model has the effect of increasing the steady state yaw moment due to increased localised pressures. At higher yaw angles, a steady state was not achieved during the time it took to traverse the gust. The transient peak yaw moments on gust entry and exit of a sharp edge model was caused by the formation and collapse of the leeward separation bubble. One of the interesting results was the damped oscillations seen in the transient yaw moment investigation.

1.3.4 Dynamic Oscillatory Test

The application of an oscillatory test rig to estimate the dynamic rotary stability derivatives of model airplanes has been used in the aeronautical field since the 1950's. Experimental work on an oscillating model by Bird et al. [10], Beam [6], and Fisher [23] was not intended to simulate the unsteady cases but rather focused on the estimation of angular rate derivatives and stability problem, Watkins et al. [72].

However, the concept of these dynamic tests can be expanded to simulate the unsteady or transient response of vehicle models.

An advantage of the dynamic test is that it is able to estimate the angular velocity derivatives (i.e. derivative with a function of velocity or angular rate). Russell [57] used the free oscillation tests to estimate the yaw rate derivatives of side force Cy_r and yaw moment Cn_r of a crude wedge-shape racing car and a conventional saloon car. The results were then applied to study the vehicle lateral stability. However, he did not particularly associate this technique with the study of unsteady aerodynamics and therefore covered only a small range of reduced frequencies. He observed that there was no trend in the results due to variation of Reynolds number in the range 0.5×10^6 to 1.0×10^6 based on model length, or due to variation in the reduced frequency range 0.09 to 0.31. Although he was not specifically interested in the static derivatives of Cy_β and Cn_β, the results showed that the values of dynamic Cy_β were 60-80% higher than static values. The difference was attributed to oscillatory effects. One phenomenon observed was that in some cases the models could sustain an oscillation of small constant amplitude, suggesting that the damping may be dependent upon amplitude of oscillation.

1.3.5 Correlation with Strouhal Number

When bluff bodies are exposed to an air flow, a stream of alternating vortices can be formed. Alternating aerodynamic forces are produced on the body from the alternating flow fields of the vortex shedding. The dimensionless frequency of the vortex shedding is called Strouhal number, St which is given in Equation (1.1).

Barnard [4] provides a basic relationship between Strouhal number and basic shapes. For instance, the Strouhal number for a long-span circular cylinder is around 0.2. For a flat plate held broadside to the flow it is around 0.145. As the span of the body reduces, the shedding becomes unsteady, and eventually a well-defined street will not be found.

Previous works considering the transient response of road vehicles does not show a clear correlation or relationship between the model configurations and Strouhal

number (i.e. reduced frequency). Sims-William and Dominy [66] examined for periodic unsteadiness by computing the autospectral density function of pressure data at each tapping by identifying the peaks. They found that the shedding frequency in the wake was not clear. Pressure measured on the parallel sides of the model showed significant unsteadiness at Strouhal numbers (based on twice the front corner radius of the model) between 0.17 and 0.2.

Later in 2001, Sims-Williams et al. [67] investigated unsteady structures in the wake of a hatchback car and found that the unsteadiness demonstrated only low coherence and weak periodicity and was very sensitive to external influence such as tunnel flow quality and turbulence intensities. It was also observed that the unsteady structure in the wake involves the alternate strengthening of the two C-pillar vortices in an asymmetrical fashion. This effect is also repeated by Passmore et al. [54].

1.4 Effect of Body Geometry on Crosswind Stability

For yaw stability the vehicle yaw moment curve must have a negative slope and vice versa for instability. Figure 1.10 shows the comparison between the unstable and stable configurations based on basic shapes.
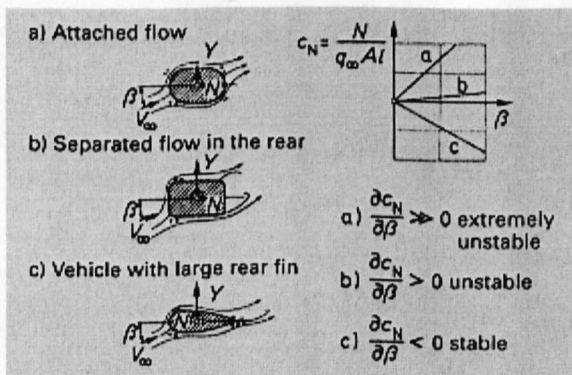
Figure 1.10 Aerodynamic stability in crosswind, Hucho [30].

The difficulty in vehicle development is that the tendency toward lower drag vehicle means a shift from typical b) type shapes to a). Shapes of form c) are not practical for road vehicles so all real vehicle tend to have unstable yaw moment characteristics.

1.4.1 Effect of Front-end Shape

Figure 1.11 shows the influence of front-end shape on the yaw moment, Hucho [30].
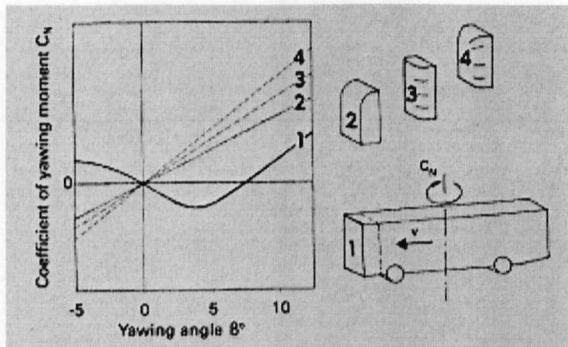
Figure 1.11 Influence of the front-end shape on the yaw moment crosswind, Hucho [30].

The square shape with sharp edges is depicted having less sensitivity to yaw moment. However, as the yaw angle increases from zero, the yaw moment gradient is negative for yaw angle less than $3°$, and then the yaw moment derivative changes to positive gradient for yaw angle greater than $5°$. As the front-end shape develops larger curves the positive yaw moment gradient becomes greater.

Matsuno et al. [45] investigated the effect of leading-edge profile on self-induced oscillation of 45-degree delta wings using a free-to-roll test. The effect of unsteady aerodynamics on the roll angle is measured using a potentiometer for different pitch angles. One of the techniques he used to study the unsteady oscillation was by phase-plane plot. It shows the round leading-edge profile changed the flow pattern from separated flow to an attached flow, thus affecting the characteristics of the induced oscillation. For a sharp leading-edge, the separation point is almost fixed, which is different when compared to a round leading-edge where the separation point moves around. Therefore he concluded that the change of moment coefficient in the sharp leading-edge becomes milder than that in the round leading-edge.

1.4.2 Effect of Rear Slant Angle and Longitudinal Edges

A general theme which has emerged is that increasing yaw moment is associated with reducing drag. Howell [32] tested a simple model shown in Figure 1.12 in the wind tunnel under steady state conditions to study the effect of rear slant angle, and the effect of C-pillar radius.
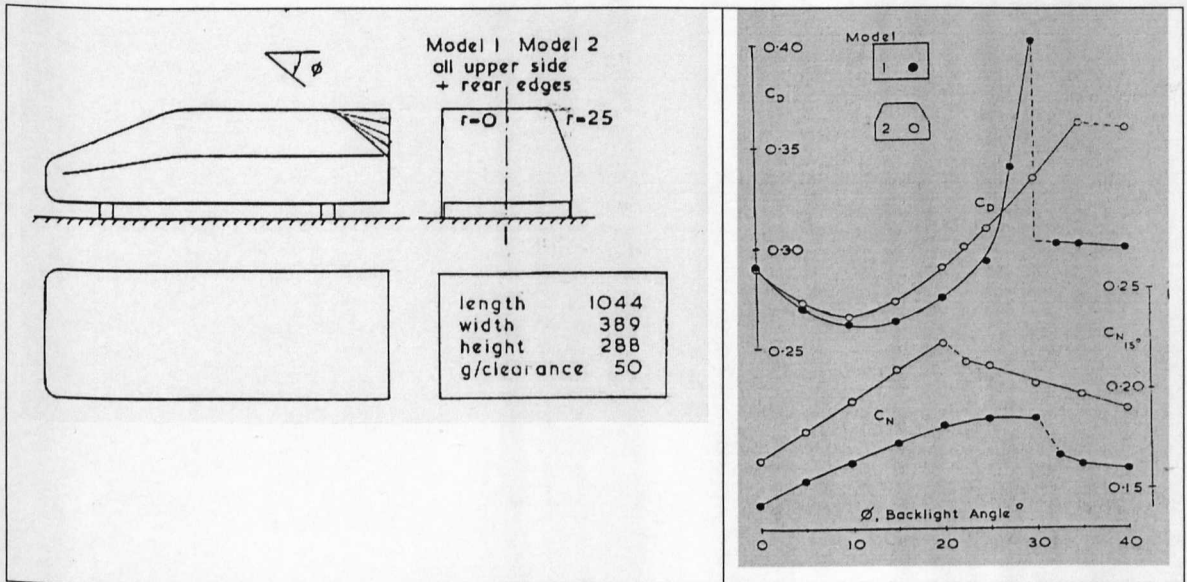
Figure 1.12 Simple wind tunnel models tested by Howell [32] in static tests. Effect of rear slant angle on drag and yaw moment Model 1 (straight C-pillar edges), Model 2 (rounded C-pillar edges).

The introduction of C-pillar rounding suppresses the rapid increase in drag usually associated with the intensity of the C-pillar vortex but is also responsible for a significant increase in the yaw moment.

Various investigations, including Ahmed et al. [2], Ryan and Dominy [60], and Bearman [7], [9] have demonstrated that the longitudinal vortices are an important feature of the vehicle wake. Ahmed et al. [2] concluded that the strength of C-pillar vortices is mainly determined by rear slant angle and that the strong C-pillar vortices were partly responsible for a high vortex drag component. Bearman [7] suggested that the greatest contribution to side force arises from the differences in the longitudinal vorticity field. These vorticies contribute to the drag as well as side force, and increased vortex drag helps explain why vehicle drag can increase with yaw.

Modification to the basic shape of a vehicle such as fixing a C-pillar strake shows a reduction in yaw moment with yaw angle. Figure 1.13 shows the effect of C-pillar strakes on flow separation.
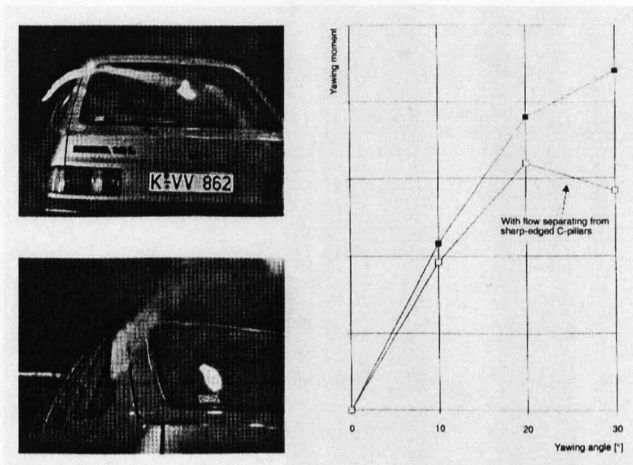
Figure 1.13 Smoke visualisation and reduction of yaw moment achieve by flow separation edge on C-pillars, Hucho [30].

1.5 Objectives of the Research Programme

The main objective of this research work is to introduce an alternative technique to quantify the unsteady aerodynamic forces and moments acting on a bluff body in the wind tunnel using an oscillating model rig. This new approach should allow a greater understanding of the characteristics of transient aerodynamic loads on passenger cars by predicting the side force and yaw moment from recorded time response histories.

An efficient, relatively low cost dynamic test rig has to be designed which can be installed in the wind tunnel quickly and measurements should be low noise and simulate the transient case sufficiently to estimate the primary derivatives effectively. The transient response from the dynamic tests is compared with the results from quasi-steady predictions in order to evaluate the differences.

A further objective of this research work is to develop a simulation model and compare the simulated response with results from the experiment. The simulation model is developed in parallel with the experimental work in order to build an understanding of the unsteady characteristics of the response.

Parametric studies on the effect of rear slant angles and C-pillar strakes are investigated. The variation in rear slant angle has been chosen for investigation because it is known to be a strong determinate of the type and structure of the wake.

On the other hand the effect of strakes is chosen because they are known to stabilise problem vehicles.

Finally, the effect of the aerodynamic derivatives on an hypothetical vehicle is tested using a simple crosswind simulation model to evaluate the crosswind sensitivity parameters such as yaw rate and path deviation.

1.6 Scope of Work

The design of an experiment to estimate the transient aerodynamic derivatives is the key feature of this research work. The design of the dynamic wind tunnel rig requires the construction of a model, model support system, installation of motion sensors, calibrations, evaluation and validation and tests.

Two types of test are described:

> (1) Conventional steady-state static tests.
> (2) Dynamic yaw oscillation tests.

In the conventional static tests, the derivatives are simply given by the gradient of side force and yaw moment versus yaw angle plots. An investigation to determine the effects of Reynolds number on the aerodynamics derivatives is also included.

The dynamic response of a simple automotive bluff body (Davis model) measured using an oscillating model rig is compared with the response obtained using the conventional static yaw test. In both cases the response is characterised by calculating the aerodynamic derivatives. A schematic of the experimental setup is shown in Figure 1.14. It consists of a simple bluff body constrained to oscillate with a single degree of freedom of pure yawing motion.
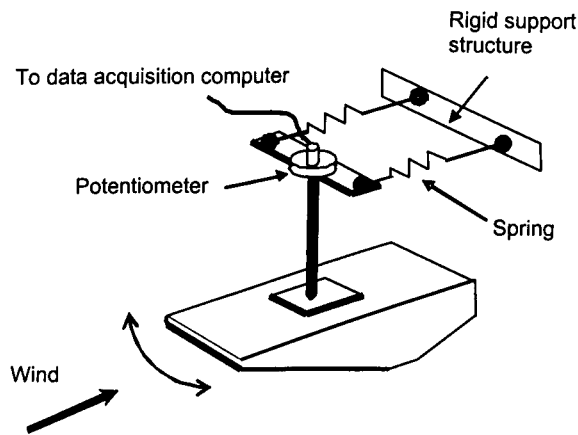
Figure 1.14 Oscillating model rig.

The oscillatory mechanism is mounted to a rigid support structure outside the working section and a circular section steel rod, passes through a clearance hole in the working section roof. The model is mounted to the end of the support rod and is free to rotate in yaw. The combination of the tunnel flow and the model oscillation then represents an unsteady condition. The externally mounted pair of springs can be changed to control the oscillation frequency. The scaling parameter of reduced frequency is used to normalise the frequency range found in the literature [25], [73]. The fundamental response of the oscillating model rig is governed by the aerodynamic stiffness and damping, and are represented as aerodynamic derivatives.

A dynamic system approach is used to describe the behaviour of the oscillating model rig shown in Figure 1.14. The analysis and prediction of dynamic system characteristics and performance can be represented as a block diagram with input and output shown in Figure 1.15.
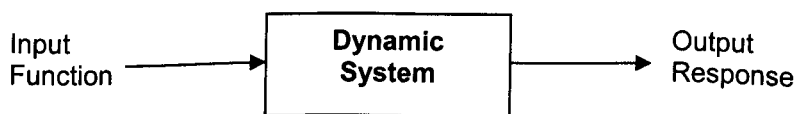
Figure 1.15 General representation of a dynamic system.

The dynamic system in the block diagram in Figure 1.15 can be linear or nonlinear. Linear systems have quantities (i.e. inertia, stiffness and damping) that behave linearly and do not vary with time. A linear differential equation with constant

coefficients is adequate to describe the motion. The use of a linear model for the system under consideration leads to fairly simple and often useful results [12]. This enables one to compute various statistics of the response in terms of a few parameters. The most complex problem of predicting the system response is when the input is random excitation and the dynamic system is nonlinear. Since the excitation is described in terms of statistical functions, even with linear dynamic systems, the output must be solved using statistical analysis (e.g. mean, root-means-square, and power spectrum [56]).

From the yaw angle time response history the aerodynamic stiffness derivative is estimated from the natural frequency, while the aerodynamic damping derivative of the damped oscillation is estimated from the time to half amplitude computed from the wind-off and wind-on data. The frequency is determined from the power spectral density. The model is shown to exhibit damped, self-sustained and self-excited oscillation behaviour. Since the unsteadiness in the oscillation amplitude is clearly seen in self-sustained and self-excited oscillation the project was then focussed on the behaviour of nonlinear oscillatory system. The unsteadiness of the self-sustained oscillation was investigated using statistical analysis, phase-plane plot and energy method.

The initial stage of the project was to establish the method of estimating the transient aerodynamic derivatives using the oscillating model rig. During this phase a single model configuration was used.

Parallel to the experimental work, a simulation model has been developed that incorporates a coupled model for the mechanical rig and the aerodynamic stiffness and damping to simulate the transient behaviour and compare with the measured time response histories. Initially the simulation is based on the static results (i.e. quasi-steady). In the quasi-steady analysis the dynamic variation of the aerodynamic forces and moments is inferred from the measured steady state derivatives. Further development of the simulation is improved by the inclusion of the aerodynamic damping derivative and the self-sustained oscillation is simulated by making the assumption that the effective damping of the system is zero, however, the unsteadiness seen in the oscillation amplitude is failed to reproduce. The unsteadiness

seen in the experimental results was then simulated by introducing a band-limited white noise function to represent the variation in lateral velocity.

Figure 1.16 shows the link between the static tests and dynamic tests, and the simulation model developed in parallel with the experimental work.
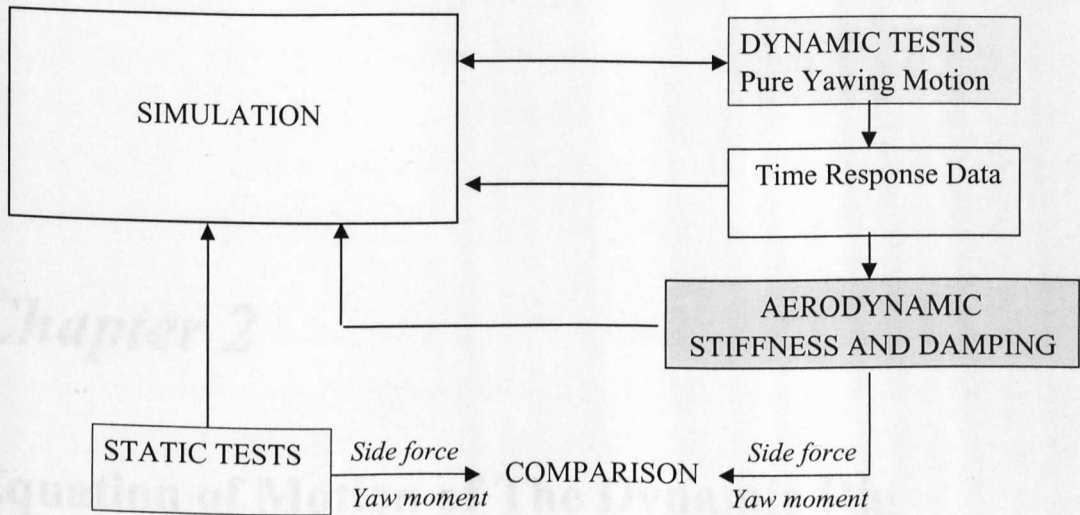
Figure 1.16 The link between static tests, dynamic tests and simulation.

In the next phase the techniques developed in the initial stage are applied in a parametric investigation of the effect of rear slant angles of zero, 10, 20 ,30 and 40 degrees and the effect of adding strakes to the C-pillar of zero, 2.5, 5.0 and 10 percent ratio of strake height to model height.

In the final phase the measured transient aerodynamic side force and yaw moment derivatives are incorporated into a simple simulation of a vehicle transient response to a lateral crosswind gust. Path deviation and yaw rate response parameters are used in the evaluation of vehicle response and crosswind sensitivity for various configurations (rear slant angles and C-pillar strakes).

Chapter 2

Equation of Motion of The Dynamic Rig

2.1 Introduction

The equation of motion of an oscillating model rig in the wind tunnel is essential to build the foundation of the transient motion of the model associated with unsteady aerodynamic loads. For the purposes of the study the aerodynamic loads are considered to act as a stiffness and damping to the model motion. The dynamic behaviour of the model motion is characterised by the natural frequency and damping ratio. Analysis of these results can be subsequently used to identify regions of linear and nonlinear behaviours.

2.2 Equation of Motion

The equation of motion to represent the dynamic response of the model mounted on the rig and oscillating with pure yawing motion is given by:

$$I_{zz}\,\ddot{\beta} + C_r\,\dot{\beta} + K_r\,\beta = \sum N_a(t) \qquad\qquad (2.1)$$

with β, $\dot{\beta}$, $\ddot{\beta}$ as the yaw angle, yaw velocity (yaw rate) and yaw acceleration respectively, I_{zz}, C_r and K_r representing the yaw inertia, mechanical damping and stiffness and $\sum N_a(t)$ being the total aerodynamic yaw moment representing the input function.

Several attempts have been made to find suitable aerodynamic yaw moment $\sum N_a(t)$ input functions. As the aerodynamic characteristics of ground vehicles have many features that are common to both civil-engineering structures and to aircraft, Hucho [30], Cooper [15], Barlow et al. [5], the development of the mathematical model in this thesis lies in these two areas.

In the estimation of aircraft unsteady aerodynamic parameters, Murphy and Klein [51] incorporate unsteady effects into the equation of motion by separating the forcing function into static, dynamic and unsteady terms. In fluid-structure interaction a van der Pol equation model is commonly useful to describe the fluctuating nature of vortex shedding and self-excited oscillation, Facchinetti et al. [20]. Perhaps a more simplistic but nonetheless useful function has been proposed by Jakobsen and Hjorth-Hansen [34], Scanlan [61] and Zhang et al. [77] whereby the aerodynamic moment is separated into two terms: the oscillating dynamic load and the unsteadiness or buffeting. For simplicity the latter approach is preferred. Thus, in this thesis the general structure proposed for the forcing function to represent the aerodynamic yaw moment model has the form:

$$\sum N_a(t) = N_a(t)_{dynamic} + N_a(t)_{unsteadiness} \qquad (2.2)$$

2.2.1 Aerodynamic Stiffness and Damping

The dynamic yaw moment $N_a(t)_{dynamic}$ can be represented by aerodynamic stiffness and damping terms. Bird et al. [10], Beam [6], Russell [57] and Nelson [52], Darling and Standen [17] used the stiffness and damping approach to estimate the unsteady aerodynamic derivatives from dynamic wind tunnel tests using an oscillating model in yaw.

The component of the unsteady aerodynamic loading that is in phase with the displacement of the motion can be regarded as an aerodynamic stiffness, while the component in phase with velocity of the motion can be interpreted as an aerodynamic damping, Tuovila and Robert [70], Van Oudheusden [71]. The aerodynamic stiffness can be viewed as an elastic property which affects the natural frequency of the oscillatory system. While the aerodynamic damping can be viewed as a frictional loss that dissipates energy, tending to stop or slow down a given motion and, which affects the damping ratio of the system. The damped frequency of the dynamic system is the product of the natural frequency and damping ratio. For a system with a very small damping ratio (i.e. close to zero) the damped frequency equals the natural frequency. Blevin [11] in his review of twenty-five years of research discussing procedures for flow-induced vibration, concluded that the use of stiffness and damping to describe galloping and flutter instability of a bluff body is generally an appropriate method and is widely accepted. Furthermore, this approach was employed by Hemon and Noger [28] in estimating the transient energy of ground vehicles of simplified vehicle shape from translational and torsional motions.

2.1.2 Unsteadiness

The unsteadiness term, $N_a(t)_{unsteadiness}$ can be thought of as disturbances in the flow arising due to random loads or turbulent wake effects. In yaw oscillation the lateral unsteadiness can be generated from lateral rotational gust r_f arising from the variation in lateral gust velocity v_f with position and time. For the purpose of simulation, the unsteadiness can be assessed numerically using a band-limited white-noise disturbance. In this work the unsteadiness input is simulated using band-limited white-noise as a variation in lateral velocity generating a fluctuation in crosswind angle.

For nonlinear random oscillations, Kareem and Gurley [35] proposed a mathematical model of aerodynamic damping which can be quantified by quasi-steady and unsteady aerodynamics. More recently, Van Oudheusden [71] designed an experimental set-up for a rotational oscillation of a rigid rectangular cylinder with an aspect ratio of 1.6. One of the conclusions is a disagreement between quasi-steady predicted and experiment, attributed to the deviation in the estimation of the aerodynamic damping,

which was found to be the main parameter governing instabilities. Rüdinger [58] proposed the estimation of aerodynamic stiffness and damping for random and nonlinear responses by probability density and total energy of the random vibration methodologies.

2.3 Mathematical Model of Pure Yawing Motion

The equation of motion of the oscillating model rig is derived from first principles corresponding to a rigid body acting under a torsional motion. A linear model is assumed and has a system characteristic equivalent to that of the simple harmonic motion of an oscillatory system. For the purpose of this investigation the equation of motion is derived by considering the dynamic aerodynamic terms $N_a(t)_{dynamic}$ in the form of stiffness and damping derivatives. And for simplicity, the unsteadiness term is assumed zero at this stage.

Figure 2.1 illustrates a single degree of freedom wind tunnel model where the motion of the vehicle is constrained to pure yawing motion.
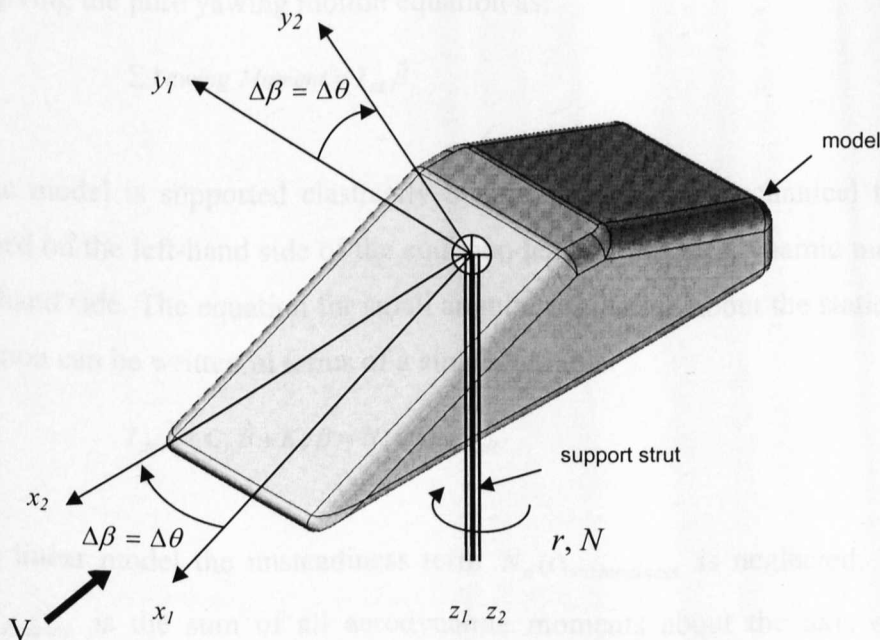
Figure 2.1 Wind tunnel model of pure yawing motion.

For the restricted motion, the variables are the angle of rotation (θ), yaw angle (β) and the time rate of change of these variables. As the model has been aligned parallel to the flow and oscillates on a fixed frame they coincide at $t = 0$, the change in angle of rotation and yaw angle are identical, that is:

$$\Delta\beta = \Delta\theta \qquad\qquad (2.3)$$

and

$$\Delta\dot{\beta} = \Delta r = \Delta\dot{\theta} \qquad\qquad (2.4)$$

The model is free to rotate about its axis of rotation (i.e. mid-wheel base, mid-track) during the test and is considered to be subject to the external moments from the aerodynamic terms generated from the flow over the body, and from the mechanical terms generated from the springs and support systems. For the purpose of derivation, the aerodynamic terms are considered to be positive. For consistency in the derivation of the equation of motion, the positive moment refers to the clockwise direction while the negative moment is referred to as anti-clockwise.

For the motion of a model constrained to perform only a simple yawing motion with the centre of rotation constrained, the yaw angle is identical to the angle of rotation, thus giving the pure yawing motion equation as:

$$\Sigma\ Yawing\ Moment = I_{zz}\ddot{\beta} \qquad\qquad (2.5)$$

As the model is supported elastically by the springs, the mechanical terms can be grouped on the left-hand side of the equation leaving the aerodynamic moment on the right hand side. The equation for small angular oscillation about the static equilibrium condition can be written in terms of a single variable:

$$I_{zz}\ddot{\beta} + C_r\dot{\beta} + K_r\beta = N_a(t)_{dynamic} \qquad\qquad (2.6)$$

For a linear model the unsteadiness term $N_a(t)_{unsteadiness}$ is neglected. The quantity $N_a(t)_{dynamic}$ is the sum of all aerodynamic moments about the axis of oscillation arising from angular deflection, velocity, acceleration etc., about the static equilibrium condition. The aerodynamic moments due to angular acceleration and higher-order terms are generally neglected in the analysis leading to the assumption that:

$$N_a(t)_{dynamic} = N_\beta \beta + N_r r = \underbrace{\frac{1}{2}\rho V^2 A\ell \frac{\partial Cn}{\partial \beta}\beta}_{\substack{aero \\ stiffness}} + \underbrace{\frac{1}{2}\rho V A\ell^2 \frac{\partial Cn}{\partial \dot\beta}\dot\beta}_{\substack{aero \\ damping}} \qquad (2.7)$$

Writing the aerodynamic stiffness and damping in the form of derivatives:

$$N_a(t)_{dynamic} = \frac{1}{2}\rho V^2 A\ell \left[Cn_\beta \beta + \frac{\ell}{V} Cn_r r \right] \qquad (2.8)$$

where,

$$Cn_\beta = \frac{\partial Cn}{\partial \beta} \qquad \text{- yaw moment due to the yaw angle derivative (rad}^{-1})$$

$$Cn_r = \frac{\partial Cn}{\partial r} \qquad \text{- yaw moment due to the yaw rate derivative (rad}^{-1})$$

V is the air velocity (m/s), A is the frontal area of the model (m^2), ℓ is the characteristic length which is normally the model length (m), and ρ is the air density (kg/m^3).

2.3.1 Wind-Off Model

In the wind-off condition the aerodynamic term is assumed zero, so that Equation (2.6) becomes:

$$I_{zz}\ddot\beta + C_r \dot\beta + K_r \beta = 0 \qquad (2.9)$$

Equation (2.9) is the characteristic equation and is equivalent to a standard second order dynamic system:

$$\Delta(s) = s^2 + 2\zeta\omega_n s + \omega_n^2 \qquad (2.10)$$

The natural frequency of the rig is given by:

$$\omega_n = \sqrt{\frac{K_r}{I_{zz}}} \qquad \text{(rad/s)} \qquad (2.11)$$

While the expression for the mechanical stiffness is:

$$K_r = \omega_n^2 I_{zz} \qquad \text{(Nm/rad)} \qquad (2.12)$$

Similarly, the damping ratio term is given by:

$$\zeta = \frac{C_r}{2\omega_n I_{zz}}$$ (2.13)

Then the expression for the mechanical damping is:

$$C_r = 2\zeta\omega_n I_{zz} \qquad \text{(Nms/rad)}$$ (2.14)

The damped frequency of the model rig can be written as a function of the natural frequency and damping ratio as:

$$f_d = \frac{1}{2\pi}\sqrt{\frac{K_r}{I_{zz}}}\sqrt{1-\zeta^2} \quad \text{(Hz)}$$ (2.15)

In order to meet the suitable range of oscillation frequencies in the wind-off condition, the required torsional stiffness can be calculated using Equation (2.12). Before constructing the rig and with no information regarding the mechanical damping available, it was assumed that the rig had a small constant damping ratio taking an expected value of less than 0.05, which led to the conclusion that the natural frequency was similar to damped frequency.

2.3.2 Wind-on Model

In the case of the wind-on condition, the total force and moment are the sum of the mechanical and aerodynamic terms. The sum of the aerodynamic moments acting on the model is due to a combination of the aerodynamic stiffness and damping. Letting K_a and C_a take the form of aerodynamic stiffness and damping, respectively:

Aerodynamic Stiffness $K_a = \frac{1}{2}\rho V^2 A \ell\, Cn_\beta = N_\beta$ (Nm/rad)   (2.16)

Aerodynamic Damping $C_a = \frac{1}{2}\rho V^2 A \ell\, Cn_r \frac{\ell}{V} = N_r$ (Nms/rad)   (2.17)

Substituting the aerodynamic stiffness and damping into Equation (2.6) leads:

$$I_{zz}\ddot{\beta} + C_r\dot{\beta} + K_r\beta = K_a\beta + C_a r$$ (2.18)

Substituting $r = \dot{\beta}$ in Equation (2.18) and rearranging yields,

$$I_{zz}\ddot{\beta} + (C_r - C_a)\dot{\beta} + (K_r - K_a)\beta = 0$$ (2.19)

The sign of the aerodynamic stiffness and damping terms in the Equation (2.19) are negative, implying that they oppose the mechanical stiffness and damping. Therefore the wind-on stiffness is less than the wind-off equivalent. Similarly, if the wind-on stiffness is more than the wind-off stiffness, it verifies that the aerodynamic stiffness provides a restoring moment which opposes the model displacement. For a system to be statically and dynamically stable, the aerodynamic stiffness and damping derivative of Cn_β and Cn_r should be negative, and vice-versa for instability.

Writing Equation (2.19) in the form of a standard second-order dynamic system normalised by its inertia:

$$\ddot{\beta} + \frac{(C_r - C_a)}{I_{zz}} \dot{\beta} + \frac{(K_r - K_a)}{I_{zz}} \beta = 0 \qquad (2.20)$$

Equation (2.20) takes the form of a simple second-order dynamic system equivalent to Equation (2.10), so by inspection, the natural frequency and damping ratio can be written as:

$$\text{Natural Frequency,} \quad \omega_n = \sqrt{\frac{(K_r - K_a)}{I_{zz}}} \quad \text{(rad/s)} \qquad (2.21)$$

$$\text{Damping Ratio,} \quad \zeta = \frac{C_r - C_a}{2I_{zz}\sqrt{\frac{(K_r - K_a)}{I_{zz}}}} \qquad (2.22)$$

2.4 Transfer Function for Free Oscillation with Initial Input

For free oscillation, tests were carried out by giving the model an initial yaw angle displacement and releasing it. The transfer function can be derived from the equation of motion, Equation (2.19), by substituting initial values.

If the initial yaw angle is β_o and released at zero angular velocity, then $\beta(0) = \beta_o$ and $\dot{\beta}(0) = 0$. By expanding Equation (2.19) in the form of a Laplace equation yields,

$$I_{zz}[s^2\beta(s) - s\beta(0) - \dot{\beta}(0)] + (C_r - C_a)[s\beta(s) - \beta(0)] + (K_r - K_a)\beta(s) = 0$$

$$I_{zz}s^2\beta(s) - I_{zz}\beta_o s + (C_r - C_a)s\beta(s) - \beta_o(C_r - C_a) + (K_r - K_a)\beta(s) = 0$$

$$\left[s^2 + \frac{(C_r - C_a)}{I_{zz}}s + \frac{(K_r - K_a)}{I_{zz}}\right]\beta(s) = \beta_o\left[s + \frac{(C_r - C_a)}{I_{zz}}\right]$$

$$\beta(s) = \frac{\beta_o\left[s + \dfrac{(C_r - C_a)}{I_{zz}}\right]}{\left[s^2 + \dfrac{(C_r - C_a)}{I_{zz}}s + \dfrac{(K_r - K_a)}{I_{zz}}\right]} \qquad (2.23)$$

2.5 Summary of Parameters

From the wind-off and wind-on equations of motion derived in the previous section, a summary of the important parameters are shown in Table 2.1.

	Wind-Off	Wind-On
Equation Of Motion	$I_{zz}\ddot{\beta} + C_r\dot{\beta} + K_r\beta = 0$	$I_{zz}\ddot{\beta} + (C_r - C_a)\dot{\beta} + (K_r - K_a)\beta = 0$
Natural Frequency (rad/s)	$\omega_n = \sqrt{\dfrac{K_r}{I_{zz}}}$	$\omega_n = \sqrt{\dfrac{(K_r - K_a)}{I_{zz}}}$
Damping Ratio	$\zeta = \dfrac{C_r}{2I_{zz}\sqrt{\dfrac{K_r}{I_{zz}}}}$	$\zeta = \dfrac{C_r - C_a}{2I_{zz}\sqrt{\dfrac{K_r - K_a}{I_{zz}}}}$
Damped Frequency (rad/s)	$\omega_d = \sqrt{\dfrac{K_r}{I_{zz}}}\sqrt{1 - \dfrac{C_r^2}{4I_{zz}K_r}}$	$\omega_d = \sqrt{\dfrac{K_r - K_a}{I_{zz}}}\sqrt{1 - \dfrac{(C_r - C_a)^2}{4I_{zz}(K_r - K_a)}}$

Table 2.1 Parameters determined from equation of motions.

The expectation from the experiment is to observe differences in oscillation frequency and the rate of amplitude decay between the wind-off and wind-on conditions. The difference in oscillation frequency between wind-off and wind-on indicates the existence of aerodynamics stiffness (yaw moment) Cn_β whereas the difference in the rate of amplitude decay indicates the existence of aerodynamic damping Cn_r.

2.6 The General Solution

In the dynamic tests the model is given an initial displacement in yaw angle (β_o) and released, the time history of yaw angle of the model measured. The general equation to describe the free oscillation of a single degree of freedom system in yaw motion is an expression of damped harmonic motion:

$$\beta(t) = \beta_o e^{-\zeta \omega_n t} \sin(\omega_d t + \phi)$$

(2.24)

where β_o is the initial yaw angle, ζ is the damping ratio, ω_n is the natural frequency and ω_d is the damped frequency in rad/s and ϕ is the phase angle. A typical time response plot of a damped oscillation is shown in Figure 2.2.
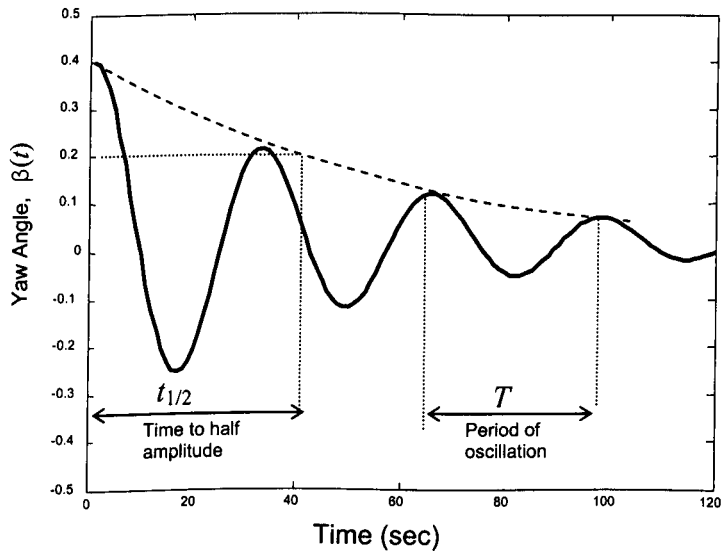
Figure 2.2 Typical response of a damped oscillation.

The frequency of the oscillation ω_d can be calculated from the period of the oscillation:

$$\omega_d = \frac{2\pi}{T} \qquad \text{rad/s.}$$

(2.25)

The ω_d can also be written in terms of natural frequency ω_n and damping ratio ζ:

$$\omega_d = \omega_n \sqrt{1 - \zeta^2}$$

(2.26)

For a damping ratio close to zero, $\zeta \approx 0$, then $\omega_d \approx \omega_n$.

In the analysis of real experimental data, the exponential decay to half the amplitude is used as a standard reference criteria for evaluation and comparison. Time to half amplitude can be derived from the exponential decay of the oscillation amplitude using the expression:

$$\beta_{1/2} = \beta \, e^{-\zeta \omega_n t_{1/2}}$$

(2.27)

For half amplitude, $\dfrac{\beta_{1/2}}{\beta} = \dfrac{1}{2}$, then Equation (2.27) becomes:

$$\frac{1}{2} = e^{-\zeta \omega_n t_{1/2}}$$

(2.28)

Solving for $\zeta \omega_n$: $\ln \dfrac{1}{2} = -0.6931 = \zeta \omega_n t_{1/2}$

$$\zeta \omega_n = \frac{0.6931}{t_{1/2}}$$

(2.29)

and $$\zeta = \frac{0.6931}{(t_{1/2})\omega_n}$$

(2.30)

The graphical representation of natural frequency ω_n damping ratio ζ and damped frequency ω_d on the s-plane is depicted in Figure 2.3.
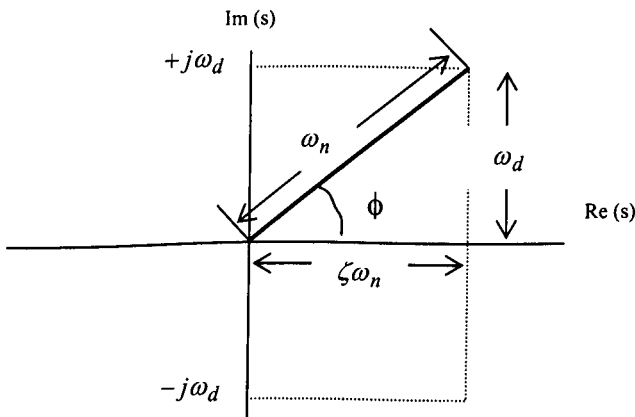
Figure 2.3 Graphical representation of natural frequency, damping ratio and damped frequency.

From the figure the expression for damped frequency is given by:

$$\omega_d{}^2 = \omega_n{}^2 - \zeta^2 \omega_n{}^2$$

(2.31)

Rearranging to get the expression for ω_n

$$\omega_n = \sqrt{\omega_d{}^2 + \zeta^2 \omega_n{}^2}$$

(2.32)

Substituting the expression for ω_d and $\zeta\omega_n$ gives:

$$\omega_n = \sqrt{\frac{4\pi^2}{T^2} + \left(\frac{0.6931}{t_{1/2}}\right)^2}$$

(2.33)

And also from Figure 2.3 the phase angle ϕ is given by:

$$\phi = \tan^{-1}\frac{\omega_d}{\zeta\omega_n} = \cos^{-1}\frac{\zeta\omega_n}{\omega_n}$$

(2.34)

For a damping ratio close to zero, $\zeta \approx 0$, the phase angle, $\phi = 90^o$.

Chapter 3

Development of the Dynamic Test Facility

3.1 Introduction

In this chapter the conceptual design of the wind tunnel test rig is explained in detail and the selection and description of the models that were used in the tests are explained. The important design requirements are described with the results from the preliminary calibration and setup tests of the oscillating rig. Initial measurements of model inertia and wind-off measurements were conducted and are reported. Instrumentation and measurement techniques, measurement accuracy, resolution and repeatability are also described.

3.2 Description of the Tunnel

3.2.1 Basic Characteristics

The wind tunnel tests were undertaken in the 1.9m x 1.3m low speed wind tunnel in the department of Aeronautical and Automotive Engineering at Loughborough University. The wind tunnel is shown in Figure 3.1.
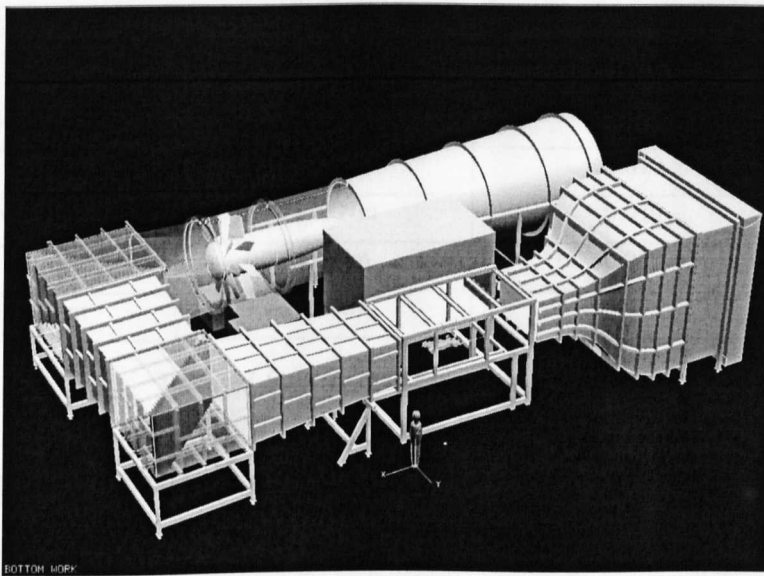
Figure 3.1 Loughborough University low speed open circuit wind tunnel.

In the empty working section the average turbulence intensity at the centre of the working section is 0.15% measured at 40 m/s. The boundary layer thickness at the centre of the working section of the floor is 60 mm at 40 m/s (at working section midpoint, equating to a displacement thickness of approximately 7.5 mm) and is assumed to be the same at the centre of the working section roof. The wind tunnel has a working range of zero to 45 m/s.

3.2.2 Balance

The tunnel is equipped with a precision six-component external balance located under the working section. A turntable attached to the balance is fitted flush to the floor and rotates together with the model. All forces and moments are measured in the body axis.

The loads are measured by load cells and the calibration matrix converts them into three forces (lift, drag and side force) and three moments (pitch, yaw and roll). The software saves the data as both force and moments and in coefficient forms. The balance is operated using a dedicated program that also allows the user to choose a suitable sampling rate and data averaging time. In the results presented in this thesis data was sampled at 100 Hz and averaged over 10 seconds. The accuracy of the six-component balance as specified by the manufacturer is summarised in the Table 3.1.

Component	Balance Load Ranges	Accuracy (% Full Scale)
Drag	± 120 N	0.010
Side Force	± 420 N	0.005
Lift	± 500 N	0.010
Roll Moment	± 150 Nm	0.010
Pitch Moment	± 60 Nm	0.010
Yaw Moment	± 45 Nm	0.015

Table 3.1 Balance load range and accuracy.

3.3 Description of the Dynamic Oscillating Rig

The oscillating mechanism used in the dynamic tests is a single degree of freedom torsional system. The schematic diagram of the experimental setup is shown in Figure 3.2.
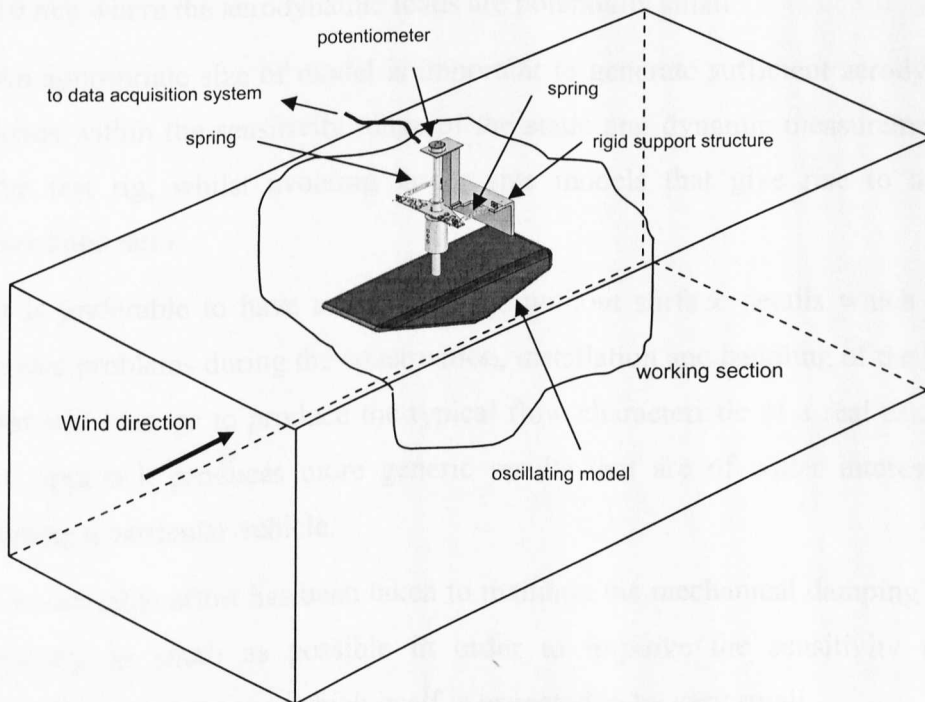
Figure 3.2 General layout of the dynamic oscillating model rig mounted to the tunnel working section roof.

The rig consists of a simple bluff body (Davis model) constrained to oscillate with a single degree of freedom of pure yawing motion. The rig is mounted to the tunnel working section roof. The oscillatory mechanism is mounted to a rigid support structure outside the working section and a circular section steel rod, of 20 mm diameter, passes through a clearance hole in the roof. The model is mounted to the

end of the support rod to provide a ground clearance of 40 mm and is free to rotate in yaw. The combination of the flow and the model oscillation then represents an unsteady condition. A range of springs were used to control the oscillation frequency, and hence reduced frequency, and the model response is measured using a potentiometer mounted at the top of the shaft.

3.3.1 Design Criteria and Specification

Some of the important criteria that were considered during the development of the dynamic test rig and some conflicting issues include:

1. The models must be light weight with low yaw inertia. This increases the sensitivity of the model and oscillating rig to the unsteady aerodynamic loads. This is of particular importance as it was proposed to utilise speeds from 10 m/s where the aerodynamic loads are potentially small.

2. An appropriate size of model is important to generate sufficient aerodynamic loads within the sensitivity range of the static and dynamic measurements of the test rig, whilst avoiding larger size models that give rise to a large blockage ratio.

3. It is preferable to have a simple shape without surface details which might create problems during the construction, installation and handling of the model but still manage to produce the typical flow characteristic of a real car. Such an approach produces more generic results that are of wider interest than testing a particular vehicle.

4. Considerable effort has been taken to maintain the mechanical damping of the test rig as small as possible in order to improve the sensitivity to the aerodynamic damping, which itself is expected to be very small.

5. Suitable geometry, test rig dimensions, and the correct selection of springs dimension and stiffness are important to cover the full range of reduced frequency for the given range of wind speed. The reduced frequency scaling is important to capture correctly the unsteady aerodynamic loading over the desired full-scale frequency bandwidth. The frequency of the free oscillation test can be varied by installing the suitable spring stiffness.

6. In order to make possible the estimation of side force derivative it must be possible to move the axis of rotation along the longitudinal axis. A provision to adjust the ground clearance is also available.

7. To develop a relatively low-cost, low-noise, rapid-access wind-tunnel approach.

3.3.2 Mechanical Design

The dimensions of the rig and the selection of springs were determined from the results of a quasi-steady analysis. A schematic drawing of the dynamic test rig is shown in Figure 3.3. The mechanical strength of the test rig (i.e. model and the support system) was calculated based on the maximum loads acting on the model and support structures. These occur at the maximum wind speed of 40 m/s acting on the largest surface area of the model of 0.063 m^2 (i.e. based on side area of the model). The safety factor at the maximum bending stress and shear stress was 94 and 2043.
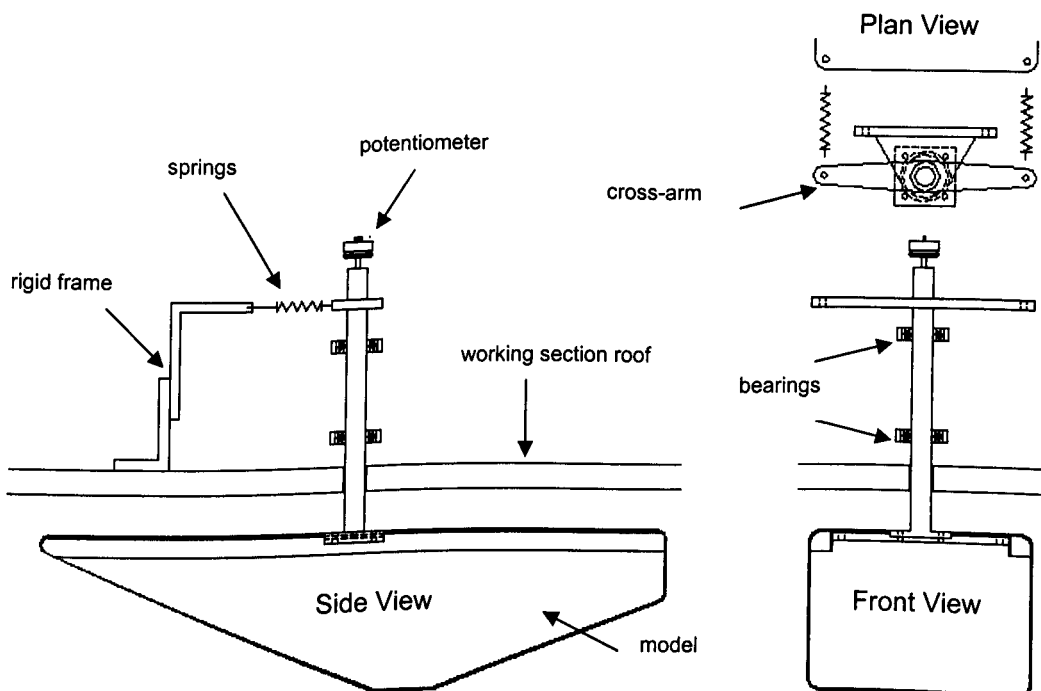
Figure 3.3 Dynamic test rig general arrangement.

As seen in Figure 3.3 two linear springs are attached to the cross arm on the top of the rod and an adjustment mechanism allows the spring forces to be equalized and the

model aligned in the tunnel. This adjustment mechanism can be seen at the end of the spring assemblies in Figure 3.4.
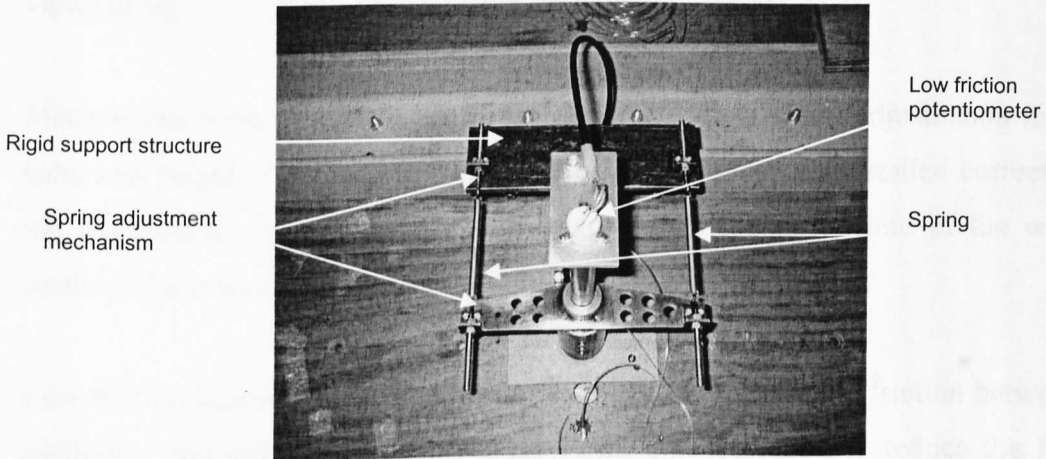
Figure 3.4 Plan view of the test rig.

Rigid support structure

Spring adjustment mechanism

Low friction potentiometer
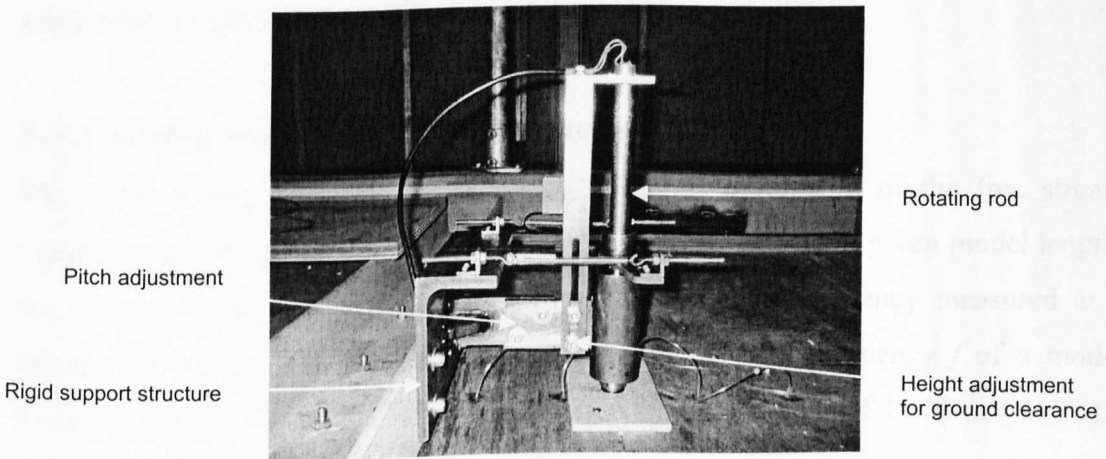
Spring

Figure 3.5 Side view of the test rig.

Pitch adjustment

Rigid support structure

Rotating rod

Height adjustment for ground clearance
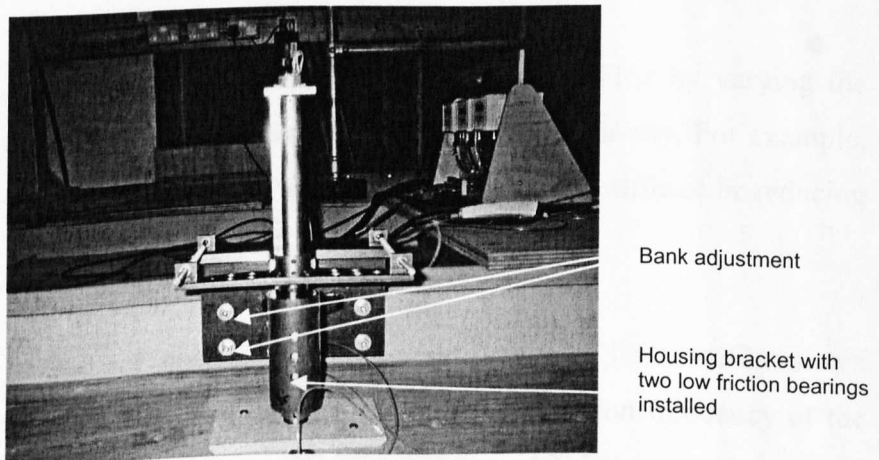
Figure 3.6 Front view of the test rig.

Bank adjustment

Housing bracket with two low friction bearings installed

The oscillation frequency of the system is modified by simply replacing the springs with springs of different stiffness. Figures 3.4, 3.5 and 3.6 show three photographic views of rig.

Mechanisms were also included in the design to allow small adjustments in pitch, bank and height. This ensures that the test rig and model are installed correctly and the longitudinal axis of the model is aligned with the centre-line of the working section. These features are indicated in the figures.

Low friction bearings were installed to minimize the mechanical friction between the oscillating rod and the housing bracket of the rig. However, to reduce the friction between the bearing and seals still further, the lubricant (grease) is removed and the ball bearings, bearing housing and seals are cleaned before the bearing is re-assembled. In addition the potentiometer is a low friction model.

3.3.3 Spring Selection and Rig Dimensions

The reduced frequency of the oscillating model is a function of the free stream velocity, oscillation frequency and the length of the model. For a given model length, the reduced frequency is calculated from the oscillation frequency measured at a given wind speed. For instance, if the measured wind-on frequency f of a model having a length of ℓ =0.625 m tested in a free stream velocity of V=20 m/s is 2 Hz, then, the reduced frequency is:

$$K_m = \frac{\pi f \ell}{V} = \frac{\pi (2)(0.625)}{20} = 0.196$$

There are therefore two ways to vary the reduced frequency. First by varying the oscillation frequency and, second, by varying the free stream velocity. For example, the reduced frequency can be increased by increasing the spring stiffness or reducing the wind speed.

The selection of the spring dimensions with a suitable range of linear stiffness was made in order to meet the maximum yaw angle and the oscillation frequency of the rig. A suitable range of oscillation was considered to be $\pm 10^\circ$ because it is believed

that it minimises the degree of nonlinear effects normally associated with large amplitude motions, without losing the important characteristics of the transient aerodynamics.

Spring selection was made with the aid of Figure 3.7 which shows the schematic of the oscillatory system, looking in plan view.
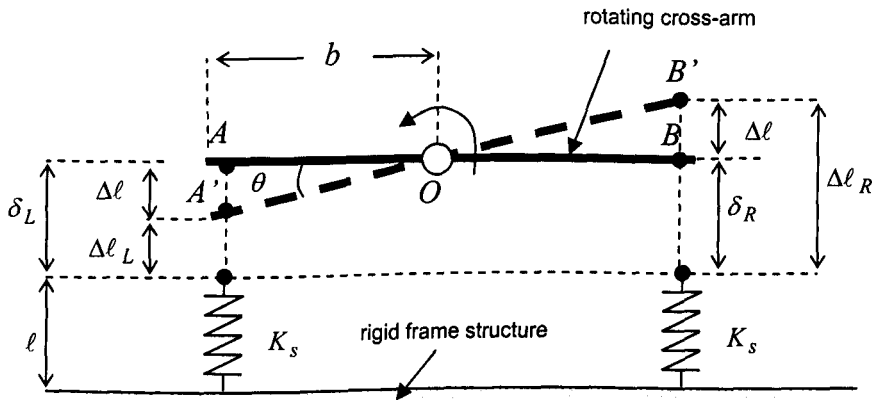
Figure 3.7 Free body diagram of dynamic test rig (from plan view).

AOB is the cross-arm length which is connected by two linear springs of the same stiffness K_s to the rigid frame structure. For the purpose of derivation, it was assumed that the springs and the cross-arm were light and the arm rotated about pivot O. For small angle oscillations about the equilibrium position, then $\sin\theta = \theta$ and $\cos\theta = 1$. With the cross-arm mounted about its midpoint then $AO = OB = b$.

For correct rig operation, the combination of the spring pair should provide a linear torsional stiffness. The springs are of the extension type, so must always be in tension during the oscillation process. Therefore, the spring is pre-loaded during installation. The initial length (i.e. zero extension) of all the springs was $\ell = 70$ mm. During the initial installation (i.e. with the model at zero yaw angle), the left spring is extended to A and the right spring to B, the extension required is annotated as δ_L and δ_R, and $\delta_L = \delta_R$. In the rig this initial extension is 30 mm.

For $\delta_L = \delta_R$, the total length of both installed springs in the pre-loaded condition is $\delta_L + \ell$. Now consider a small anti-clock wise rotation from AOB to $A'OB'$. The spring

on the right is extended and the left is shortened a distance of $\Delta\ell$ from the initial position of the rotating arm (i.e. zero yaw). As the length of rotating arm b is 100 mm and the maximum yaw angle is 10 degrees, the maximum spring extension $\Delta\ell$ during oscillation is given by:

$$\Delta\ell = b\sin(10) \approx b\theta = 17.4 \text{ mm}$$

This provides a clear safety margin when compared to the 30 mm pre-loaded condition. Finally, the required total spring extension is the sum of the pre-load length plus the extension during oscillation (i.e. $30+17.4 = 47.4$ mm).

3.4 Description of the Model

The model employed in the study is a simplified bluff body that represents a road vehicle shape, (Davis model). The model dimensions employed in this study are shown in Figure 3.8. In this application the model is approximately 1/6 scale when compared with an average road car.
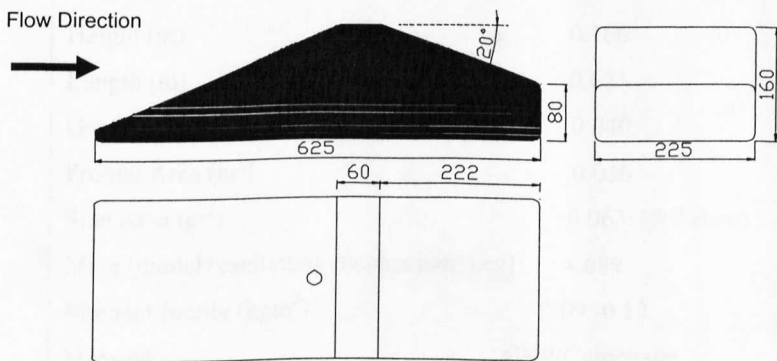
Figure 3.8 General dimensions of baseline shape of Davis model. All edge radii 10 mm.

Important features of the model that make it suitable to be employed in this study include:

1. The model represents the approximate proportions of real cars, i.e. it has the proper ratios of length, width and height comparable to the average passenger cars.

2. Simplified model without complication of detail, such as wheels, side mirrors etc. Such details are vehicle specific and potentially sensitive to variation in Reynolds number.

3. The model is able to produce the same main flow characteristics as a real car. The flow remains largely attached over the fore body. The rear section has a variable geometry that, when altered, is capable of generating all the primary rear end flow fields seen on road vehicles. These include a complete quasi-2D separation in the zero slant angle (estate car) and the 3D vortex structures seen for others, Ahmed et al. [2], Bearman [7].

4. The basic geometry has been used by many other researchers, Davis [18], Bearman and Mullarkey [8], Passmore et al. [54], Ryan and Dominy [59] and Howell [32] allowing the possibility of comparison and correlation of results.

The detailed model specifications are given in Table 3.2.

Parameters	
Width (m)	0.225
Height (m)	0.160
Length (m)	0.625
Ground Clearance (m)	0.040
Frontal Area (m^2)	0.036
Side Area (m^2)	0.063 (20° slant)
Mass (model+oscillating mechanism) (kg)	4.689
Moment Inertia (kgm^2)	0.09 -0.12
Material	GRP/Composite

Table 3.2 Specification of Davis model.

The main model (baseline model with 20° slant) was constructed from fibreglass material and a lightweight foam used to change the shape of the rear slant angle. The use of the lightweight back sections minimise any changes in model inertia or shift in weight which could affect the dynamic characteristics.

In addition to the 20° slant the parametric study also considers rear slant of 0, 10, 30 and 40 degrees. Figure 3.9 shows the Davis model with various rear slant angles.
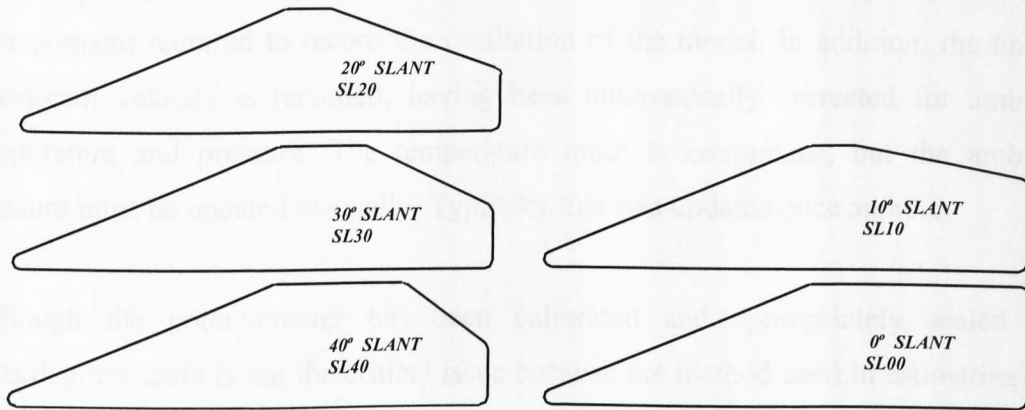
Figure 3.9 Model with different rear slant angles. All edge radii 10 mm.

In subsequent figures the abbreviated slant angle descriptions SL20 etc. are used to denote the test configuration.

3.5 Instrumentation and Data Acquisition

A schematic of the test rig instrumentation and data acquisition equipment is shown in Figure 3.10.
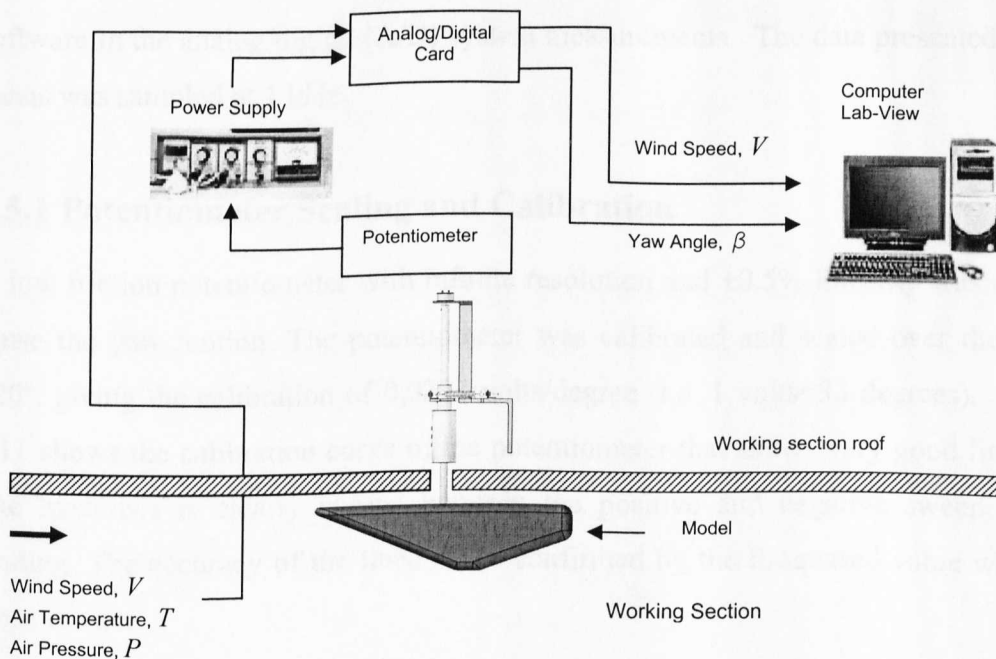
Figure 3.10 Schematic diagram of system set-up.

The simplicity of the technique means that the potentiometer output is the only measurement required to record the oscillation of the model. In addition, the tunnel freestream velocity is recorded, having been automatically corrected for ambient temperature and pressure. The temperature input is continuous, but the ambient pressure must be updated manually. Typically this was updated once an hour.

Although the potentiometer has been calibrated and appropriately scaled the volts/degrees scale is not the critical issue because the method used in estimating the aerodynamic derivatives is based on relative measurements and correlation between wind-on and wind-off responses. The analysis of the output yaw angle is always normalised with the initial yaw amplitude (i.e. not based on absolute values). The most important aspect of the measurement system is the ability of the rig to reproduce similar results of the same tests at any time or, in other words, to have good repeatability.

The analogue signal from the low friction potentiometer was fed to NI-DAQ (National Instruments) data acquisition system through single-ended analogue inputs. The NI-DAQ system has a maximum sampling rate of 500 kHz, with a 12-bit resolution. A commercial data acquisition package was used as the interfacing software in the analog/digital (A/D) system measurements. The data presented in this thesis was sampled at 1 kHz.

3.5.1 Potentiometer Scaling and Calibration

A low friction potentiometer with infinite resolution and ±0.5% linearity was used to sense the yaw motion. The potentiometer was calibrated and scaled over the range ±20°, giving the calibration of 0.0303 volts/degree (i.e. 1 volts=33 degrees). Figure 3.11 shows the calibration curve of the potentiometer that shows very good linearity. The hysterisis is clearly unseen between the positive and negative sweep of the reading. The accuracy of the linear fit is confirmed by the R-squared value which is close to one.
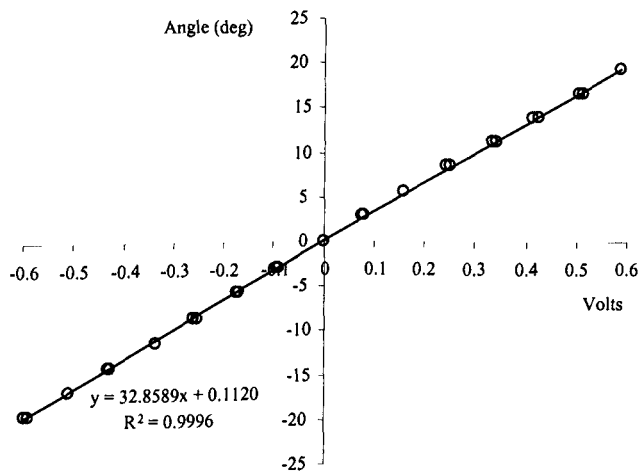
Figure 3.11 Potentiometer scaling and calibration.

The input voltage range of ±5 Volts was supplied to the potentiometer. With the 12-bit resolution of the A/D card, the resolution of measurement was given by:

$$\text{Resolution} = 10 \text{ V} / (2^{12}-1) = 0.002442 \text{ Volts} = 2.442 \text{ mV}$$

The resolution can also be given in terms of percentage of full scale, typically at 0.02442% of the full scale deflection (i.e. changes smaller than 0.0806 degree are not seen by the A/D).

3.5.2 Signal to Noise Ratio

In the initial tests the potentiometer signal was found to be contaminated with noise. The installation of a linear regulated power supply, and the replacement of the original signal cable with a screened cable led to a significant improvement in the recorded data. In the wind-off condition, the noise was reduced from 25 mV peak-to-peak (p-p) to 3 mV p-p. Figure 3.12 shows the comparison between the noisy and the improved signal data in the wind-off conditions.

The voltage fluctuation of 3 mV p-p equates to around 0.0990° p-p. As the model fluctuates with a small angle when the wind is on, the voltage fluctuation is higher than wind-off. However, with the model constrained to remove the oscillation the

signal noise during the wind-on tests is again approximately 3 mV p-p. Considering a full scale measurement of $\pm 10°$ (i.e. $20°$ p-p) the typical noise to signal ratio is around 0.5%.
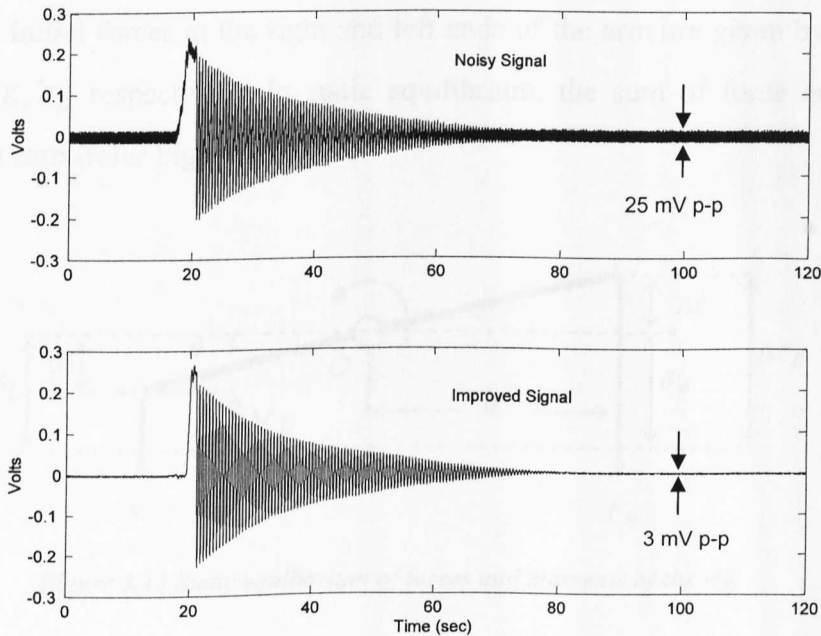
Figure 3.12 Comparison between the noisy and the improved signals.

3.5.3 Precision of the Dynamic Test Rig

The precision of the test rig is confirmed by evaluating the consistency and the repeatability from several test runs for the same test conditions using cylinder disc. The standard deviation of the damped frequency from the mean value for spring K2 to K10 is less than 0.2%. The results from the test using cylinder disc are presented in Appendix A.

The estimation of derivatives was found to be sensitive to the variation in damped frequency and damping ratio of the time response data between the wind-off and wind-on conditions. Detailed evaluations of the accuracies are explained in Chapter 5.

3.6 Rig Calibration

3.6.1 Mechanical Stiffness

Now, let the original length of the spring before extension be ℓ. The springs were preloaded at both ends with an initial extension of δ_L for the left end and δ_R for the right end. Initial forces at the right and left ends of the arm are given by $F_R = K_s \delta_R$ and $F_L = K_s \delta_L$ respectively. In static equilibrium, the sum of force and moments about O is zero (refer Figure 3.13),
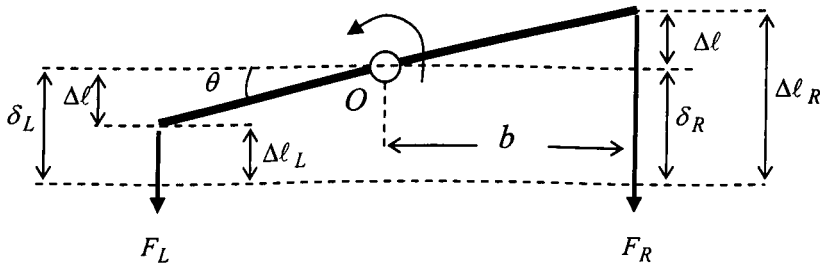
Figure 3.13 Static equilibrium of forces and moments of the rig.

$$\Sigma F = 0 ; \qquad F_L + F_R = 0 \qquad \text{then} \qquad F_L = -F_R \qquad (3.1)$$

$$\Sigma T = 0 ; \qquad -F_L b + F_R b = 0 \qquad \text{then} \qquad F_R b = F_L b \qquad (3.2)$$

If the arm rotates anticlockwise with a small yaw angle, forces at both ends are acting in the same direction because the springs are pre-loaded. Additional forces at the right and left end of the arms are given by $\Delta F_R = K_s(\delta_R + \Delta\ell)$ and $\Delta F_L = K_s(\delta_L - \Delta\ell)$ respectively. We can derive the equation of motion by taking moments about O, and assuming no damping effect on the rig and a small angle of rotation:

$$\Sigma T = I_{zz}\ddot{\theta}$$

$$K_s(\delta_L - \Delta\ell)b - K_s(\delta_R + \Delta\ell)b = I_{zz}\ddot{\theta}$$

$$K_s\delta_L b - K_s \Delta\ell b - K_s \delta_R b - K_s \Delta\ell b = I_{zz}\ddot{\theta}$$

$$-2K_s \Delta\ell b = I_{zz}\ddot{\theta} \qquad (3.3)$$

As $\Delta\ell = b\sin\theta$, Equation (3.3) becomes:

$$-2K_s b\sin\theta\, b = I_{zz}\ddot{\theta} \qquad (3.4)$$

Rearranging:

$$I_{zz}\ddot{\theta} + 2 K_s b^2 \sin\theta = 0 \tag{3.5}$$

Equation (3.5) is nonlinear because the response variable θ appears as the argument of the sine function. For small angle oscillations about the equilibrium position, the equation can be linearised by using the approximation $\sin\theta \approx \theta$:

$$I_{zz}\ddot{\theta} + 2 K_s b^2 \theta = 0 \tag{3.6}$$

Equation (3.6) represents the equation of motion of the mechanical torsional motion which can be written as:

$$I_{zz}\ddot{\theta} + K_r \theta = 0 \tag{3.7}$$

where K_r is the torsional stiffness of the mechanical system:

$$K_r = 2 K_s b^2 \qquad \text{(Nm/rad)} \tag{3.8}$$

Writing this in its general form:

$$\ddot{\theta} + \frac{2 K_s b^2}{I_{zz}}\theta = 0 \tag{3.9}$$

The natural frequency of the rig in the wind-off condition is given by:

$$\omega_n = \sqrt{\frac{2 K_s b^2}{I_{zz}}} \qquad \text{(rad/s)} \tag{3.10}$$

3.6.2 Wind-off Tests

The dynamic responses of the $20°$ rear slant model are determined for a series of different springs, with the characteristics shown in Table 3.3. The calculated values of natural frequency $f_{n_{off}}$ are determined using Equation (3.10) and the value of K_s supplied by the manufacturer (refer Appendix A). The measured values of natural frequency $f_{n_{off}}$ are determined using Equation (2.33) by substituting the period of oscillation and time to half amplitude of the measured time response data.

Spring Code	Linear Stiffness K_s (N/m)	Torsion Stiffness K_r (Nm/rad)	Calculated $f_{n_{off}}$ (Hz)	Measured $f_{n_{off}}$ (Hz)
K1	49	0.98	0.4982	0.4915
K2	119	2.38	0.7764	0.7749
K3	214	4.28	1.0412	1.0667
K4	306	6.12	1.2451	1.3167
K5	806	16.12	2.0207	2.0333
K6	1051	21.02	2.3075	2.3083
K7	1751	35.02	2.9784	2.8167
K8	2242	44.84	3.3702	3.3917
K9	2594	51.88	3.6251	3.5917
K10	3399	67.98	4.1496	4.1407

Table 3.3 Calculated and measured wind-off frequencies based on 20° slant.

3.6.3 Mechanical Damping

If the mechanical damping that exists in the system is considered, Equation (3.7) can be modified by adding the mechanical torsional damping term C_r which is a function of angular velocity $\dot{\theta}$:

$$I_{zz}\ddot{\theta} + C_r\dot{\theta} + K_r\theta = 0 \qquad\qquad (3.11)$$

Comparing Equation (3.11) with a simple second order system, the torsional damping is given by:

$$C_r = 2\zeta\omega_n I_{zz} \qquad \text{(Nms/rad)} \qquad\qquad (3.12)$$

Where ζ is known as the equivalent (effective) mechanical damping ratio of the rig. This can be estimated experimentally from a wind-off oscillation test. The time to half amplitude was determined from the rate of decay of the peak amplitude, which refers to the time taken for the amplitude to decay from 10° to 5°. The calculated values of wind-off damping frequency ζ_{off} are determined using Equation 2.30. Figure 3.14 shows the damping ratio versus damped frequency from the results of two tests. The repeatability is seen to be very good.
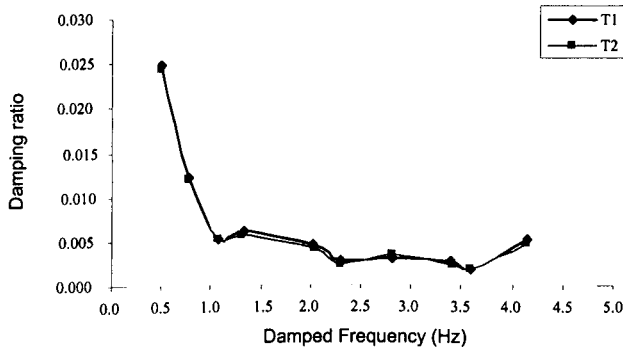
Figure 3.14 Wind-off damping ratio versus damped frequency and repeatability (20° slant).

The damping ratio in the wind-off condition is very small with a highest value that occurs at low frequency, of less than 0.025 (i.e. 2.5% of the critical damping of $\zeta = 1$). At frequencies above 1 Hz the damping ratio is of the order of less that 0.005.

3.6.4 Estimation of Moment of Inertia

The moment of inertia of the system (model and the support system) is determined experimentally from the wind-off free oscillation tests. The moment of inertia is given by the relationship between the natural frequency and the torsional stiffness for a series of different spring stiffness. If the torsional stiffness K_r (Nm/rad) and natural frequency ω_n (rad/s) are known, then:

$$I_{zz} = \frac{K_r}{\omega_n^2} \qquad (3.13)$$

By plotting a graph for a series of K_r versus ω_n^2, the moment of inertia can be determined from the gradient of the graph.
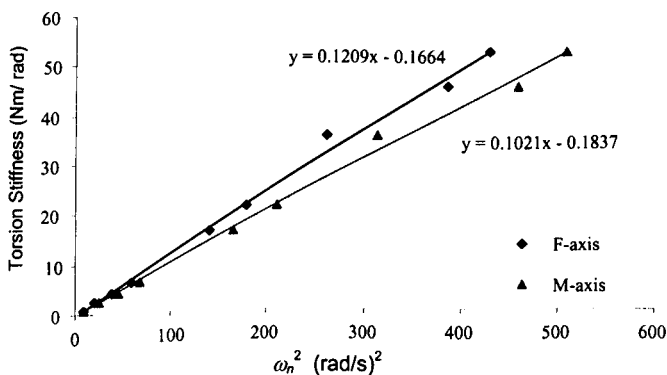
Figure 3.15 Measured wind-off damped frequency versus torsional stiffness to estimate moment of inertia of the oscillation model rig for mid and front axis (20° slant).

Figure 3.15 shows the gradient for both mid and front axes of rotation. The moment of inertias are 0.1021 kgm^2 and 0.1209 kgm^2 respectively.

The moment of inertia can also be estimated by averaging the calculated value of inertia at each point using the same expression of $I_{zz} = 2K_s b^2 / \omega_n^2$ but the first method by gradient was adopted because of the better level of confidence.

3.7 Pilot-Tests of the Dynamics Test Facility

The purpose of the pilot-tests is to integrate the whole system and evaluate the performance of the rig. The capability, limitations and behaviour of the facility are determined. The dynamic tests cover the frequency range 0.5 to 5 Hz and wind speed from 0 to 40 m/s. The range of interest for the oscillation amplitude is ±10°. However, during testing the model was released from an initial yaw angle of about 17° with the analysis of the data performed from 10° to 1° for damped oscillation.

Table 3.4 shows the experimental results of reduced frequency for ten springs tested at 10, 20, 30 and 40 m/s. The 'x' marking shown in the table indicates that the model yawed to the maximum limit of the rig, i.e. the aerodynamic stiffness (yaw moment) exceeds the mechanical stiffness.

Spring Code	Reduced	Frequency		
	V=10 m/s Re=4.28x10^5	V=20 m/s Re=8.55x10^5	V=30 m/s Re=1.28x10^6	V=40 m/s Re=1.71x10^6
K1	0.05	x	x	x
K2	0.13	x	x	x
K3	0.19	0.07	x	x
K4	0.25	0.11	0.05	x
K5	0.39	0.18	0.11	0.07
K6	0.44	0.21	0.13	0.08
K7	0.55	0.27	0.17	0.12
K8	0.66	0.33	0.21	0.15
K9	0.70	0.35	0.22	0.16
K10	0.81	0.40	0.26	0.19

Table 3.4 Measured reduced frequencies based on 20° slant model at four wind speeds.

Results have been obtained for the system over the range of reduced frequencies indicated by the literature [25], [73]. Example time response data is shown for three springs at a speed of 10 m/s in Figure 3.16. The effect of the aerodynamic damping is clearly seen when the wind-on and wind-off traces are compared.
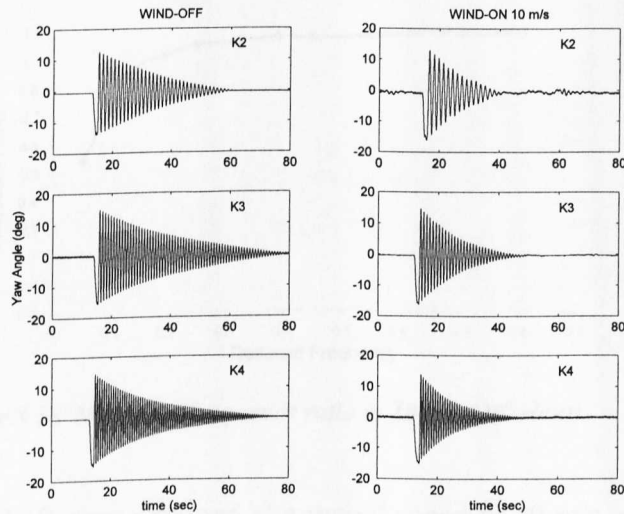
Figure 3.16 Example damped time response data (20⁰ slant).

Figure 3.17 compares the wind-off and wind-on damping ratio at 10 m/s tunnel speed for all ten springs. For wind-off it is seen to be very small indicating that the mechanical damping is small. This ensures that the system is sensitive to any aerodynamic damping that may be present in the wind-on tests. In the wind-on condition the aerodynamic contribution to the damping is seen to be significant at low oscillation frequencies. At higher frequencies the damping is small. However, the presence of some aerodynamic damping can be seen across the frequency range tested.
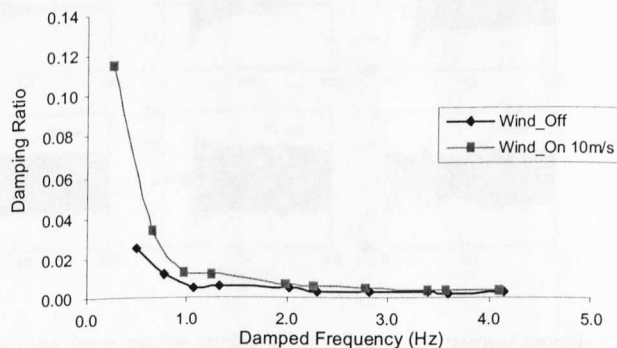
Figure 3.17 Comparison of wind-on and wind-off damping ratios (20⁰ slant).

The frequency ratio $(f_{d_{on}} / f_{d_{off}})$ between wind-on and wind-off is shown for all ten springs at a speed of 10 m/s in Figure 3.18. It is evident from the smooth nature of the curve that the transient aerodynamic response is a function of reduced frequency. For reduced frequencies greater than about 0.4 the frequency ratio approaches unity.
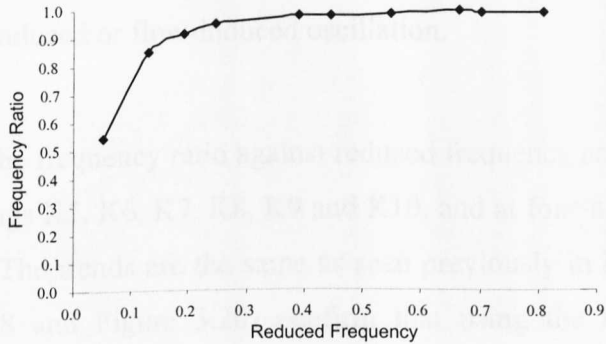
Figure 3.18 Measured frequency ratio at 10 m/s (20° slant).

The results in Figure 3.18 were obtained at a tunnel speed of 10 m/s, at this speed the response is damped across the frequency range. However at higher tunnel speeds the damped response was not always seen. Figure 3.19 shows the response for a single spring K5 over a range of tunnel speeds. It is evident that above a critical speed the oscillation ceases to be damped, and a self-sustained oscillation occurs.
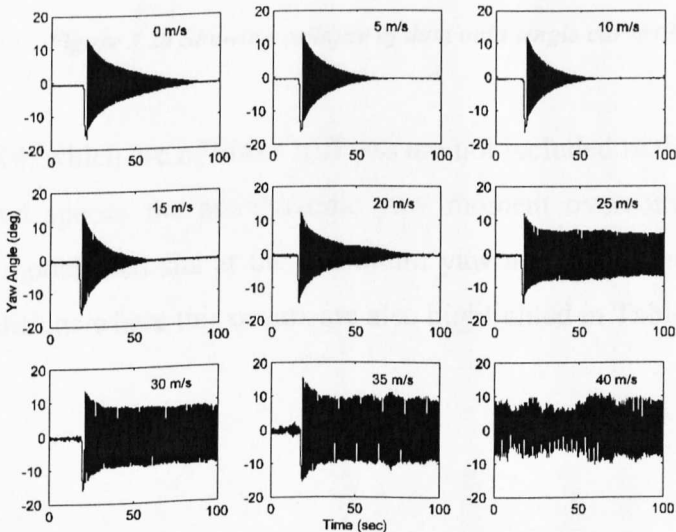
Figure 3.19 Time response for a single spring over a range of tunnel speeds (20° slant).

At higher speeds still, (40 m/s) no initial displacement of the model is required to generate the oscillation, this is referred to as a self-excited oscillation. The transition away from the damped response is independent of reduced frequency, but rather depends on the tunnel speed or Reynolds number. The self-sustained and self-excited oscillation would suggest the existence of effects such as turbulent wake or asymmetric vortex formation exciting the model. This type of behaviour is categorised as self-induced or flow-induced oscillation.

Figure 3.20 shows the frequency ratio against reduced frequency as in Figure 3.18 but in this case for springs K5, K6, K7, K8, K9 and K10, and at four tunnel speeds of 10, 20, 30 and 40 m/s. The trends are the same as seen previously in Figure 3.18. These figures (Figure 3.18 and Figure 3.20) confirm that using the reduced frequency collapses the data onto a single curve very effectively.
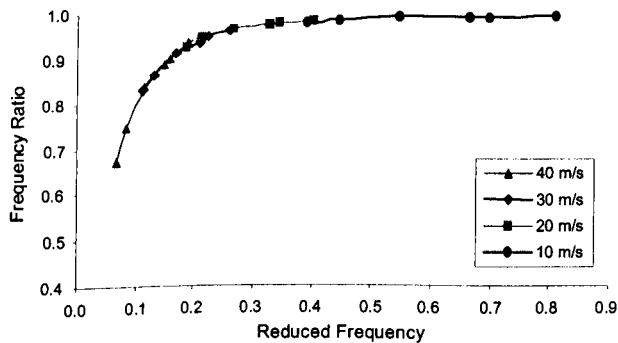
Figure 3.20 Showing collapse of data onto single curve (20° slant).

Spring K1 to K4, which are of lower stiffness are not included in the figure because at the higher wind speeds the aerodynamic yaw moment overcomes the mechanical stiffness. The model then sits at the maximum yaw angle stop and no oscillation is produced, conditions where this occurs are also highlighted in Table 3.4.

3.7.1 Repeatability Tests

The repeatability of the measurement of moment of inertia from two sets of tests T1 and T2 are shown in Figure 3.21.
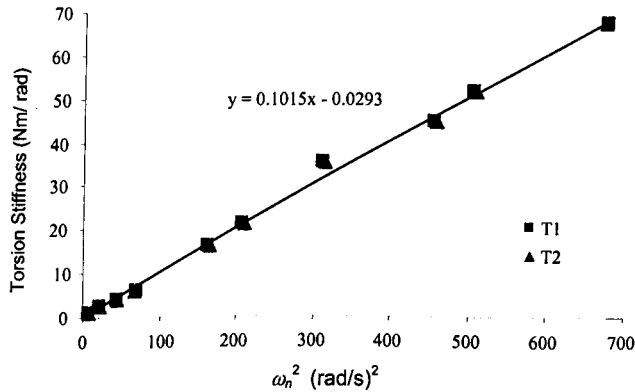
Figure 3.21   Measurement of moment of inertia from two repeat tests (20° slant).

Figure 3.22 shows the frequency ratio (i.e. $f_{d_{on}} / f_{d_{off}}$) of ten springs at 10 m/s from two repeat tests (T1 and T2). The results show good agreement.
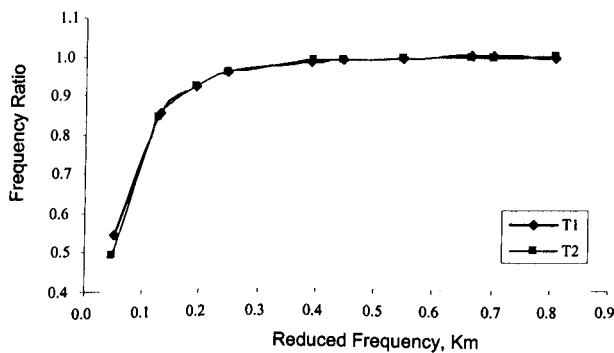
Figure 3.22   Frequency ratio versus reduced frequency for all spring at 10 m/s shows repeatability of two repeat tests (20° slant).

The frequency ratio increases with the increase of reduced frequency, and approaches unity when the reduced frequency is greater than 0.4.

Figure 3.23 shows the same plot but for springs K5, K6, K7, K8, K9 and K10 of four repeat tests. In every test each spring was tested at four different wind speeds of 10, 20, 30 and 40 m/s. Results from the four repeat tests show good repeatability whereby the frequency ratio collapses onto a single curve.
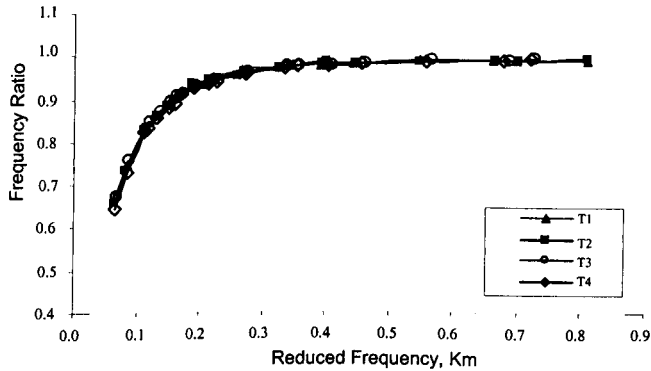
Figure 3.23 Frequency ratio versus reduced frequency for springs K5 to K10 shows repeatability of four repeat tests (T1, T2, T3 and T4) of 20° slant.

Based on the data in Figure 3.23 the standard deviation of the frequency ratio of four repeat tests is less than 0.7% about its mean value.

3.8 Wind Tunnel Blockage

As the experimental procedure in this thesis is based on relative measurements rather than absolute values, the blockage effect is not a critical issue. However, to minimize the effect of secondary flows due to the close proximity to the side walls the model blockage is kept as small as possible, Barlow et al. [5]. It is generally agreed that if the blockage ratio is less than 2.5%, the blockage correction is not necessary.
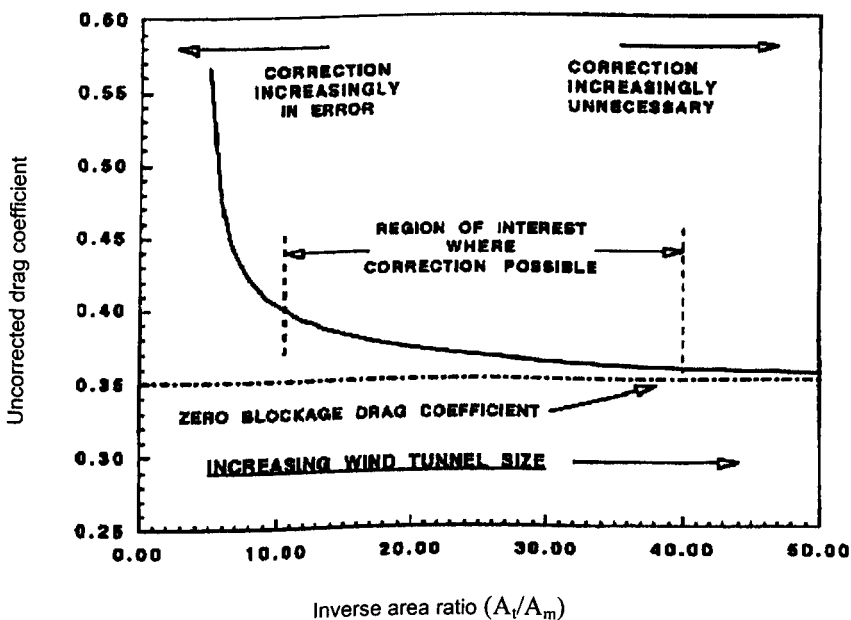
Figure 3.24 Effect of model size on blockage behaviour, Cooper [16].

For example Cooper [16] in Figure 3.24 shows how the uncorrected drag coefficient approaches the zero blockage value, and suggested for $A_t/A_m > 40$ the correction is unnecessary. The condition $A_m/A_t = 40$ is equivalent to a blockage ratio of 2.5%.

In all tests the blockage ratio lies well below this at value of 1.4% (i.e. $A_t/A_m = 69$).

Chapter 4

Static Tests

4.1 Introduction

The static yaw aerodynamic derivatives were obtained from a conventional yaw test with the model mounted on the six-component balance. The model was mounted using a single circular rod at the mid-wheel-base, mid-track that passed through a hole on the floor of the test section to a plate attached to the external balance.

Tests were conducted between 10 to 40 m/s which corresponds to a range of Reynolds numbers based on model length between 0.43×10^6 and 1.71×10^6. The yaw range was between $-16°$ and $16°$ with an increment of $2°$.

The aerodynamic derivatives of side force and yaw moment was determined from the gradient of the coefficient versus yaw angle calculated over a yaw angle range consistent with that generated in the dynamic tests, i.e. $\pm 10°$.

4.2 Results from 20° Rear Slant Angle

Figure 4.1 shows the 20° slant model mounted on the floor turntable for static tests.

| | |
| Side view | Front view |
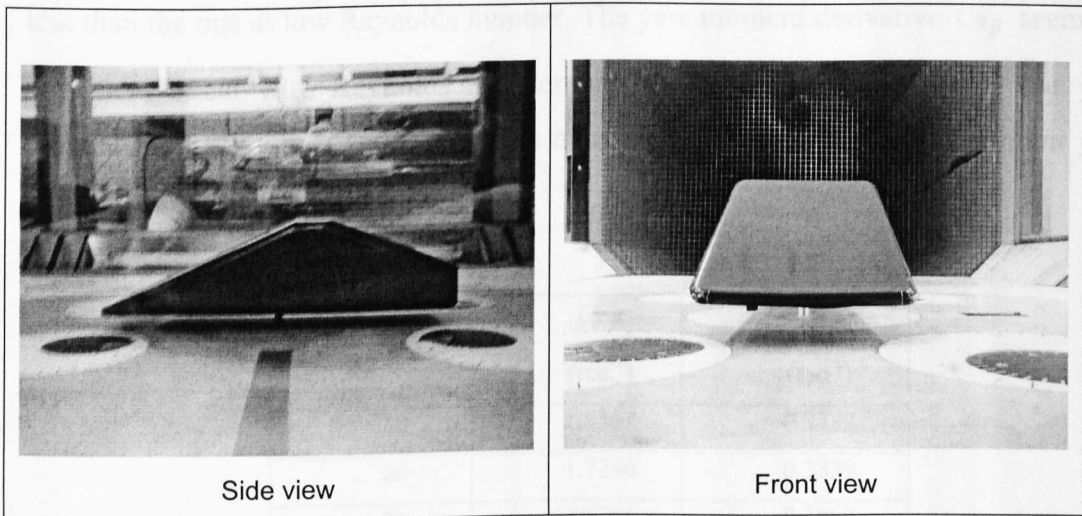
Figure 4.1 Model (20° slant) setup for static tests.

As the 20° slant was the baseline model, extensive tests and more results were produced from the model such as the effect of ground clearance and measurement of all three forces (lift, drag and sideforce) and three moments (pitch, yaw and roll).

4.2.1 Side Force and Yaw Moment Derivatives of 20° Slant

Figure 4.2 shows the side force and yaw moment coefficients versus yaw angle for 20° slant model at four different wind speeds of 10, 20, 30 and 40 m/s.
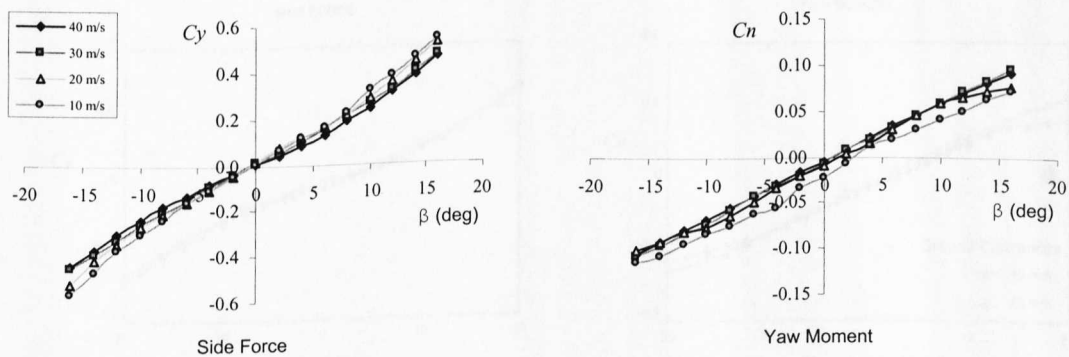
Figure 4.2 Side force and yaw moment coefficients against yaw angle at different wind speeds of 20° slant.

The side force and yaw moment derivatives were determined from the gradient of side force and yaw moment coefficient in the yaw angle range ±10°. The results are shown

in Table 4.1. The side force derivative Cy_β significantly reduces as the Reynolds number increases. The side force derivative at the highest Reynolds number is 19% less than the one at low Reynolds number. The yaw moment derivative Cn_β seems to have less effect with Reynolds number when compared to side force. The yaw moment derivative at highest Reynolds number is 6% less from the maximum yaw moment derivatives.

Wind Speed (m/s)	Cy_β (rad^{-1})	Cn_β (rad^{-1})
10	1.8507	0.3782
20	1.7246	0.3839
30	1.5756	0.3667
40	1.4954	0.3610

Table 4.1 Static measured derivatives of Cy_β and Cn_β for 20° slant.

4.2.2 Effect of Ground Clearance

The model was tested at two ground clearances of 40 mm and 60 mm, equivalent to 25% and 38% of the overall height of the model respectively. Figure 4.3 shows that the side force and yaw moment coefficients had negligible effect with ground clearance for a range yaw angle range of ±10°.
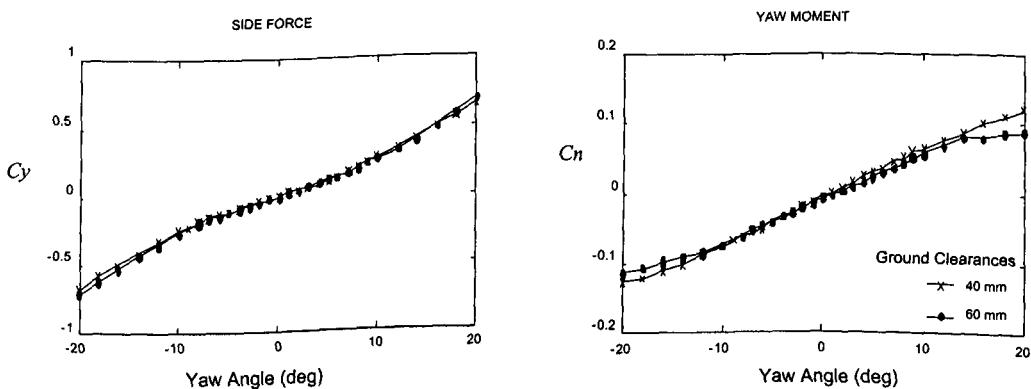
Figure 4.3 Side force and yaw moment versus yaw angle for 40 mm and 60 mm ground clearances at 40 m/s of 20° slant.

Hysterisis is not seen in either side force and yaw moment derivatives for a range of yaw angle of ±10°.

As the ground clearance has no significant effect on Cy_β and Cn_β derivatives within $\pm 10°$ of the yaw angle, the effect of ground clearance is not investigated further.

4.3 The Effect of Rear Slant Angle

Tests were conducted to measure the static coefficient of side force, yaw moment and drag for various rear slant angles at 40 m/s (Re=1.71x10^6). The results are shown in Figure 4.4.
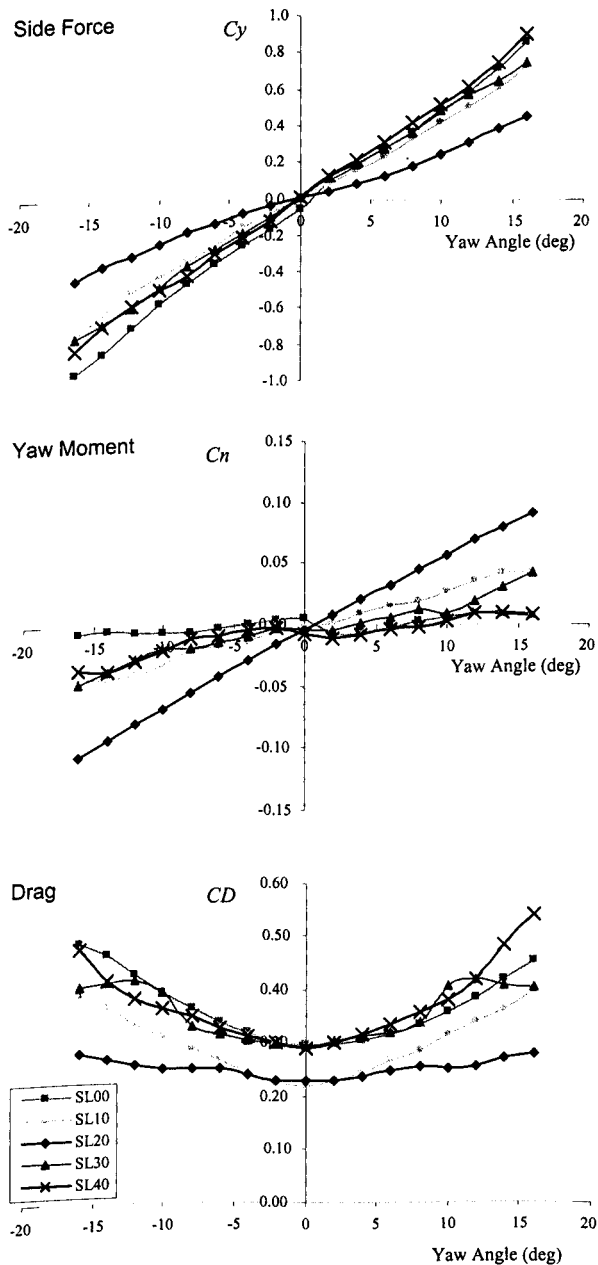
Figure 4.4 Side force, yaw moment and drag coefficient versus yaw angle for different rear slant angles at 40 m/s.

Figure 4.5 shows the summary of static measured coefficients of drag, yaw moment, side force and the centre of pressure for various rear slant angles at 10° yaw and 40 m/s (Reynolds number of 1.71x10⁶). The figure shows all the coefficients for different rear slant angle presented at 10° yaw except for drag coefficient where zero degrees is also added to the plot. A 20° slant has the lowest drag coefficient compared to other models at both zero and 10° yaw. While a 30° slant has the greatest drag at both zero and 10° yaw. From zero to 10° yaw, the drag coefficient of 30° slant increased by 40%, when compared to only 10% increment given by 20° slant.
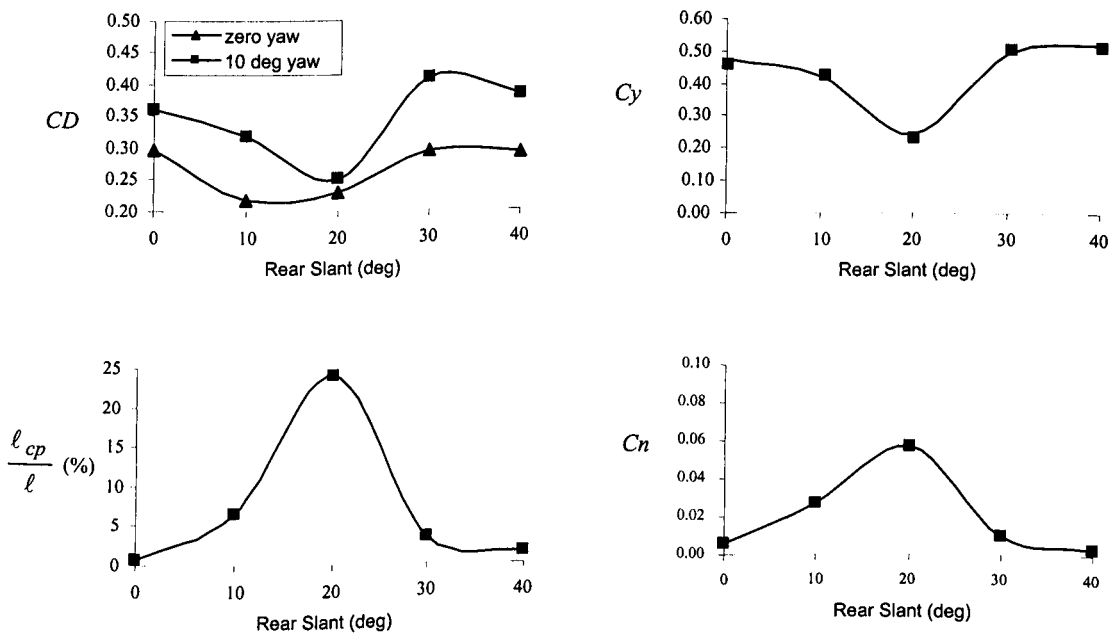
Figure 4.5 Side force, yaw moment coefficient and centre of pressure for various rear slant angles for 10° yaw and drag (zero and 10° yaw) at 40 m/s (Re=1.71x10⁶).

As expected for a model with rounded edges especially on the longitudinal pillars, Howell [32] (refer to Figure 1.12) the zero and 40° slant angle exhibit very small yaw moment but high side force and the 20° shows a large yaw moment. Furthermore, at 10° yaw the 20° slant has a yaw moment six times higher than the 30° slant indicating that the 20° slant has the greatest susceptibility to crosswind. The location of the centre of pressure from the centre of the model of the 20° slant which is much further forward than the other models could be the main cause of why the 20° slant is more susceptible to crosswind.

4.3.1 Side Force and Yaw Moment Derivatives of Various Slant

Figure 4.6 shows the side force and yaw moment derivatives for different rear slant angles. The results are presented in the form of side force and yaw moment derivatives for four tunnel speeds between 10 to 40 m/s, representing a Reynolds number range of 4.25×10^5 to 1.71×10^6. There is evidently some Reynolds number dependency for all models but this is most pronounced in the yaw moment derivative for the $30°$ slant angle.
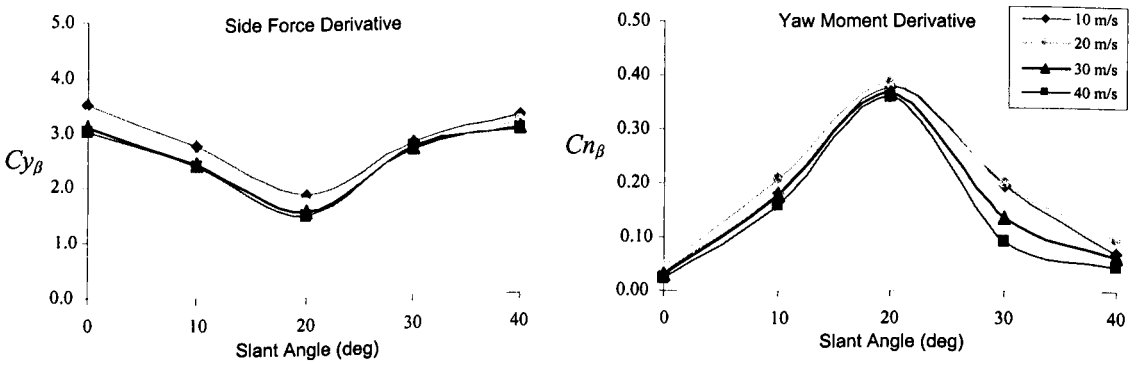
Figure 4.6 Static side force and yaw moment derivatives of different slant angles at 10 to 40 m/s.

To have a clear trend on how these derivatives vary with Reynolds number, the side force and yaw moment derivatives can be plotted again versus Reynolds number as shown in Figure 4.7 and Figure 4.8.
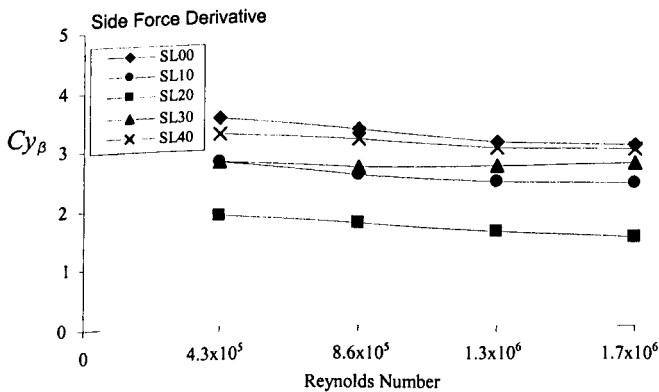
Figure 4.7 Static side force derivatives versus Reynolds number for different rear slant angles.
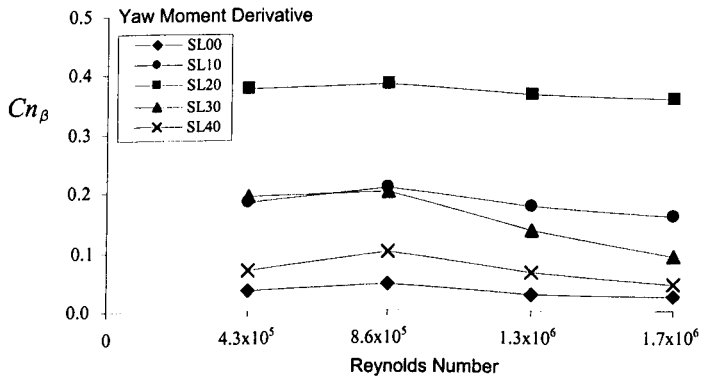
Figure 4.8 Static yaw moment derivatives versus Reynolds number for different rear slant angles.

Side force derivative appears to consistently reduce with increasing Reynolds number for all but the 30° slant. The yaw moment derivative generates a peak value at 8.6×10^5 and then reduced for all configurations.

4.4 Quasi-Steady Response

The quasi-steady time response of the oscillating model is predicted from the static data shown in the previous section. It can be estimated from Equation (2.23) by substituting an appropriate value of I_{zz}, C_r, K_r, C_a and K_a. An impulse input is used to simulate the free oscillation response. The aerodynamic stiffness derivative used in the simulation is from the static measured case Cn_β while the mechanical damping ratio of $\zeta = 0.03$ and moment inertia of $I_{zz} = 0.102$ kgm^2 are measured from wind-off measurements. The quasi-steady response was produced in Matlab, a commercial software package design to allow simple coding of a dynamic model from its mathematical description or transfer function.

Figure 4.9 shows the predicted wind-off and wind-on time response for $Cn_\beta = 0.3782$ rad^{-1} (i.e. at 10 m/s). The frequency shown on each plot was calculated from the wind-off damped frequency of the rig. For the purpose of illustration, the figure shows only six out of the ten frequencies (ten springs) available. However, the six frequencies shown cover the complete frequency range in the actual experimental set-up.

At 10 m/s the model exhibits a damped type of oscillation for all frequencies. For a positive Cn_β the wind-on damped frequency is always less than the wind-off damped frequency. As the aerodynamic damping is assumed zero in this case, the damping effect seen in the simulation is the contribution from the small mechanical damping in the system. As the oscillation frequency increases the wind-on and wind–off oscillation seems to behave in a similar manner which can be seen for 4.14 Hz in Figure 4.9.
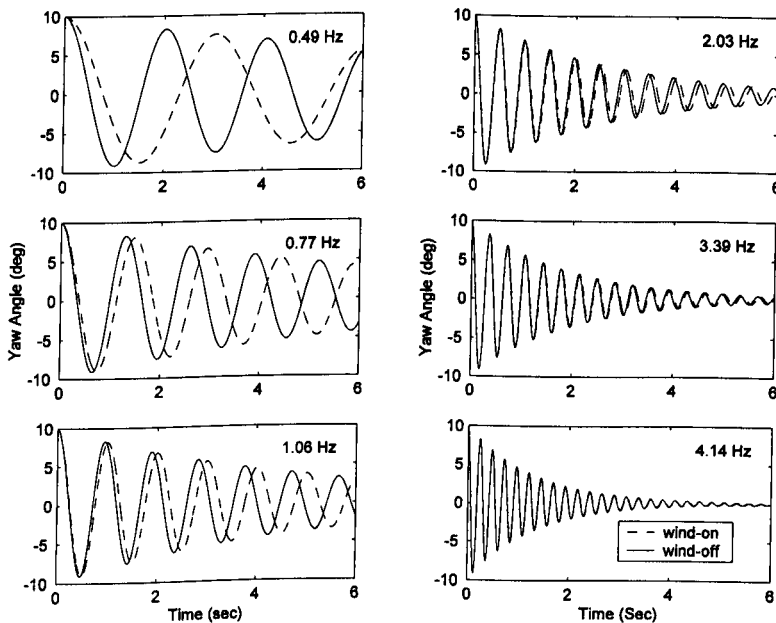
Figure 4.9 Quasi-steady response for 20° slant angle of $Cn_\beta = 0.3782$ ***rad^{-1} at 10 m/s.***

Figure 4.10 shows the responses for Cn_β =0.3610 rad^{-1} (i.e. at 40 m/s) with zero aerodynamic damping as in Figure 4.9 simulated at a higher wind speed of 40 m/s. For frequencies of 0.49, 0.77 and 1.06 Hz a divergent unstable response is predicted. This arises because the aerodynamic stiffness is positive (i.e. unstable), and therefore when it exceeds the mechanical stiffness (i.e. $K_a > K_r$) the effective stiffness of the rig is zero. At this point the spring is no longer able to hold the model from further increase in yaw. However, the damped oscillation is returned at the higher frequencies. For all frequencies of the rig, the wind-on damped frequencies at 40 m/s are lower than at 10 m/s.
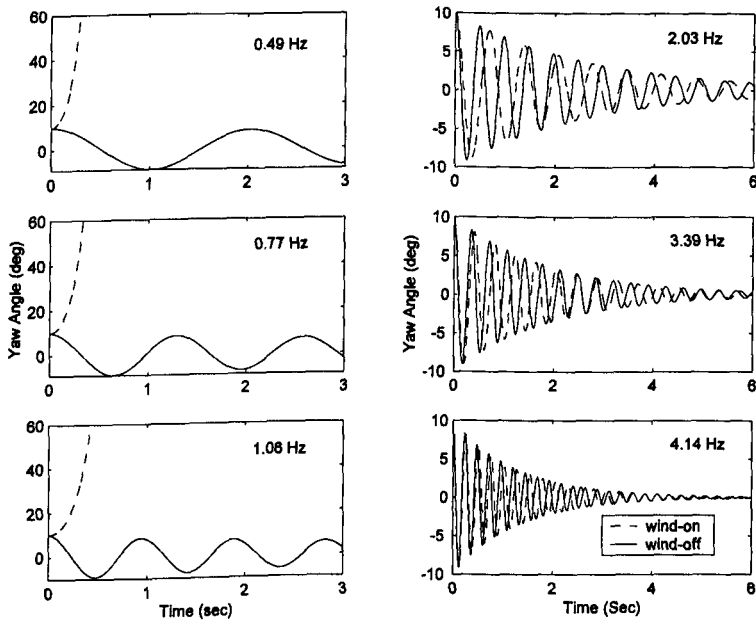
Figure 4.10 Quasi-steady response for 20° slant angle of $Cn_\beta = 0.3610\ rad^{-1}$ at 40 m/s.

The outcome from this analysis verifies that instability or divergent responses occurred at low spring stiffness (i.e. low frequency). The safety of the tunnel and the model rig has to be considered if the tests are to be conducted at this critical condition.

In addition to the time responses the wind-on damped frequency are also predicted. The ratio between wind-on and wind-off damped frequency can be plotted against reduced frequency in Figure 4.11 for wind speeds of 10, 20, 30 and 40 m/s.
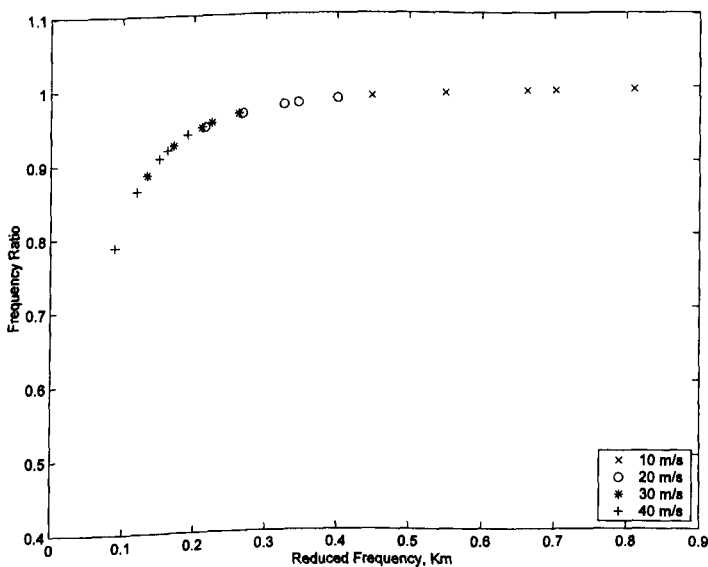
Figure 4.11 Showing collapse of frequency ratio onto single curve for 20° slant.

There are less point plotted at higher speeds because the reduced frequencies for unstable responses cannot be determined. For example, only seven points are plotted at 40 m/s because the other three points are unstable. The figure shows that using the reduced frequency collapses the data onto a single curve which demonstrates a similar trend to Figure 3.20. The discussion between measured (Figure 3.20) and simulated (Figure 4.11) results will be covered in Chapter 6.

Figure 4.12 shows the effect of rear slant angle on the frequency ratio. In the quasi-steady simulation this amounts to changing the value of Cn_β. The frequency ratio for all rear slant angles tends to be close to unity for a reduced frequency of more than 0.6. At low reduced frequency, below 0.4, the frequency ratio for a large positive value of Cn_β (20° slant) is far less than unity when compared to small positive Cn_β (square back). For Cn_β close to zero the frequency ratio is always close to unity for all reduced frequencies.
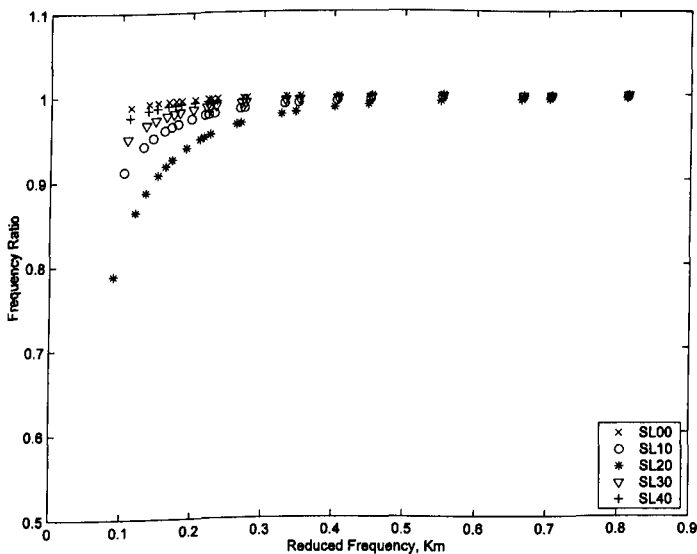
Figure 4.12 Showing the effect of rear slant angle on frequency ratio versus reduced frequency.

From this trend it can be expected that for a negative value of Cn_β the frequency ratio curve moves from larger than unity at low reduced frequency, falls as reduced frequency increases, and tends to unity at high reduced frequency.

Important points which can be drawn from the quasi-steady response analysis are:

1. The oscillation frequency and aerodynamic stiffness is a function of yaw moment derivative Cn_β.

2. For positive yaw moment derivative the wind-on total frequency is less than wind-off. The amplitude is always damped by the mechanical damping.

3. Frequency ratio increases as reduced frequency increases and is close to unity as reduced frequency reaches 0.6.

4. The model exhibits instability with a divergent increase in amplitude when the aerodynamic stiffness (yaw moment) is greater than the mechanical stiffness.

Chapter 5

Calculation of Aerodynamic Derivatives

5.1 Introduction

This chapter is concerned with the estimation of vehicle aerodynamic derivatives using mathematical descriptions of an oscillatory system. It begins with the derivation of the mathematical formulation to identify the aerodynamic derivatives from the time response histories of yaw angle oscillation. Test and verification of each stage was carefully done to ensure the accuracy of the equations used in the calculations and consistency of the estimated values. The case study using the simulated quasi-steady yaw response with known derivatives was used to evaluate the performance of the estimation process.

5.2 Estimation of Yaw Stiffness and Damping Derivatives

For a free oscillation test, the appropriate type of input to excite the model is an impulse. The impulse is created by generating a very short pulse input to the model or simply by generating an initial offset and releasing it to let the model oscillate freely. In order to estimate the aerodynamic stiffness and damping, the test must be conducted in the wind-off and wind-on conditions.

In the wind-off, the period of one cycle of oscillation T_o and time to half the amplitude $(t_{1/2})_o$ can be obtained directly from the displacement time histories and the wind-off natural frequency and damping determined:

$$[\omega_n^2]_{wind-off} = \frac{K_r}{I_{zz}} = \frac{4\pi^2}{T_o^2} + \left(\frac{0.6931}{(t_{1/2})_o}\right)^2 \tag{5.1}$$

$$[2\zeta\omega_n]_{wind-off} = \frac{C_r}{I_{zz}} = \frac{1.3863}{(t_{1/2})_o} \tag{5.2}$$

The subscript o shows wind-off condition.

In the wind-on test, the natural frequency and damping is given by:

$$[\omega_n^2]_{wind-on} = \frac{K_r - K_a}{I_{zz}} = \frac{4\pi^2}{T^2} + \left(\frac{0.6931}{(t_{1/2})}\right)^2 \tag{5.3}$$

$$[2\zeta\omega_n]_{wind-on} = \frac{C_r - C_a}{I_{zz}} = \frac{1.3863}{(t_{1/2})} \tag{5.4}$$

The aerodynamic stiffness (i.e. in-phase with displacement) can be determined from the change in oscillation frequency due to air flowing over the body and can be calculated by subtracting the expression of natural frequency ω_n^2 of the wind-off (Equation (5.1)) from the wind-on condition (Equation (5.3)). Then the aerodynamic stiffness is given by:

$$\hat{N}_\beta = -\left[\frac{K_a}{I_{zz}}\right] = -\left\{4\pi^2\left(\frac{1}{T^2} - \frac{1}{T_o^2}\right) + 0.6931^2\left[\frac{1}{(t_{1/2})^2} - \frac{1}{(t_{1/2})_o^2}\right]\right\} \tag{5.5}$$

Writing the period of oscillation in term of frequency ratio then gives:

$$\hat{N}_\beta = -\left\{4\pi^2 f_o\left(\left[\frac{f}{f_o}\right]^2 - 1\right) + 0.6931^2\left[\frac{1}{(t_{1/2})^2} - \frac{1}{(t_{1/2})_o^2}\right]\right\} \frac{Nm/rad}{kgm^2} \tag{5.6}$$

The aerodynamic damping (i.e. in-phase with velocity) can be determined by operating on the logarithmic decrement of decay of the oscillation calculated by subtracting the expression of the damping term $2\zeta\omega_n$ for the wind-off (Equation (5.2)) from the wind-on (Equation (5.4)) condition. Subsequently, the aerodynamic damping is given by:

$$\hat{N}_r = -\left[\frac{C_a}{I_{zz}}\right] = -1.3863\left[\frac{1}{(t_{1/2})} - \frac{1}{(t_{1/2})_o}\right] \qquad \frac{Nms/rad}{kgm^2} \qquad (5.7)$$

Equation (5.6) and (5.7) can be re-written in the general form in terms of natural frequency, damped frequency and damping ratio as:

$$\hat{N}_\beta = -\omega_{d_{off}}^2\left[\left(\frac{f_{d_{on}}}{f_{d_{off}}}\right)^2 - 1\right] + \zeta_{off}^2\omega_{n_{off}}^2\left[\left(\frac{\zeta_{on}^2\omega_{n_{on}}^2}{\zeta_{off}^2\omega_{n_{off}}^2}\right) - 1\right] \qquad (5.8)$$

$$\hat{N}_r = -2\zeta_{off}\omega_{n_{off}}\left[\frac{\zeta_{on}\omega_{n_{on}}}{\zeta_{off}\omega_{n_{off}}} - 1\right] \qquad (5.9)$$

The $\hat{N}_\beta$ and $\hat{N}_r$ are the dimensional aerodynamic derivatives and have to be normalised with dynamic pressure and moment of inertia to make it equivalent to the non-dimensional static yaw moment derivative Cn_β and damping Cn_r, Beam [6], Bird et al. [10], Nelson [52], Hales [26].

Yaw moment derivative: $Cn_\beta = \dfrac{\hat{N}_\beta I_{zz}}{\frac{1}{2}\rho V^2 A\ell}$ (rad^{-1})   (5.10)

Yaw damping derivative: $Cn_r = \dfrac{\hat{N}_r I_{zz}V}{\frac{1}{2}\rho V^2 A\ell^2}$ (rad^{-1})   (5.11)

5.3 Estimation of Derivatives for Self-Sustained Oscillation

Estimation of the aerodynamic stiffness derivatives using the method described in Section 5.2 is still applicable for self-sustained oscillation. However, the use of the logarithmic decay in estimating the aerodynamic damping is clearly unworkable for self-sustained oscillation. Alternative techniques to describe the aerodynamic damping or to quantify the effect of aerodynamic damping on the oscillation are therefore required. In the self-sustained oscillation an estimate of the aerodynamic damping derivative is made by making the assumption that the effective damping ratio is zero (i.e. the aerodynamic damping cancels the mechanical damping). This assumption is only accurate to determine the cross-over condition or the critical limit of the model when the self-sustained oscillation is initiated. Alternative techniques using the combination of statistical analysis, phase-plane and energy methods are then

required to describe the motion. These techniques are discussed later in the thesis (Chapter 6).

Since the aerodynamic damping is very small during the self-sustained oscillation the damping effect on the frequency is neglected and the entire shift is attributed to the aerodynamic stiffness. The new expression for the aerodynamic stiffness can then be simplified from Equation (5.8) as:

$$\hat{N}_\beta = -\omega_{d_{off}}{}^2 \left[\left(\frac{f_{d_{on}}}{f_{d_{off}}} \right)^2 - 1 \right] \tag{5.12}$$

As the equivalent damping ratio is very small, the damped frequency is equal to the natural frequency of the oscillation, and:

$$\frac{\omega_{n_{on}}}{\omega_{n_{off}}} = \frac{f_{d_{on}}}{f_{d_{off}}} \tag{5.13}$$

Rearranging Equation (5.9) to express the aerodynamic damping in a more general form as a function of frequency ratio leads to:

$$\hat{N}_r = -2\zeta_{off}\, \omega_{n_{off}}{}^2 \left[\frac{\zeta_{on}}{\zeta_{off}} \left(\frac{f_{d_{on}}}{f_{d_{off}}} \right)^2 - 1 \right] \tag{5.14}$$

5.4 Estimation Procedures and Validation

In order to apply the equation discussed in Section 5.2 and 5.3 a procedure has been developed:

1. Identify the range of sampled data from the recorded time response history which are suitable for estimation. For a damped type of oscillation the range is selected from $10°$ down to $1°$ of yaw angle. Oscillations greater than $\pm 10°$ are excluded because of effects associated with the initial release from rest of the model. These have been seen to introduce additional variation in the measured oscillation frequency, so by excluding them the repeatability is improved. Data below $\pm 1°$ is excluded because for such small oscillations the signal to noise ratio is poor.

2. Determine the oscillation frequency f_d (Hz) from the time response data. The oscillation frequency is determined from the power spectral density, calculated from the model oscillation. The period of the oscillation can be calculated from the oscillation frequency as $T = 1/f_d$.

3. For a damped oscillation, identify all positive peak amplitudes from the time response data and record the time when each of the peak amplitudes occurred. Curve-fit these peak amplitudes using a polynomial and approximate the rate of amplitude decay. Then, interpolate the curve-fitted data to estimate the time to half amplitude $(t_{1/2})$. The time to half amplitude was determined from the rate of decay of the peak amplitude, which refers to the time taken for the amplitude to decay from $10°$ to $5°$.

4. Perform step 1, 2 and 3 for wind-off and wind-on time response data, to get the wind-off and wind-on damped frequency and time to half amplitude.

5. Calculate the aerodynamic stiffness $\hat{N}_\beta$ by substituting the measured damped frequency and time to half amplitude for wind-off and wind-on in Equation (5.6). Then, calculate the aerodynamic stiffness (i.e. yaw moment) derivative Cn_β from Equation (5.10).

6. Calculate the aerodynamic damping $\hat{N}_r$ by substituting the measured time to half amplitude for wind-off and wind-on in Equation (5.7). Then, calculate the aerodynamic damping (i.e. yaw damping) derivative Cn_r from Equation (5.11).

5.4.1 Matlab Codes

The post-processing and analysis of the data used in carrying out the procedures was automated using Matlab m-files. Procedures 1 and 2 are carried out in *filpsd.m, xymax.m* while procedure 3 is performed by a function called *expdecay.m.* Details of the code can be found in Appendix D.

5.4.2 Software Validation

By simulating a number of sets of time response data using the methods described in Sections 5.2, the model can be validated and its overall accuracy assessed. In this

manner, one can assess directly the effects of noise and other imperfections, prior to proceeding with the real data. The validation and accuracy of the estimation results were evaluated based on the comparison between the estimated and simulated values of Cn_β and Cn_r used to generate the time response history. A flow chart of the process is shown in Figure 5.1.
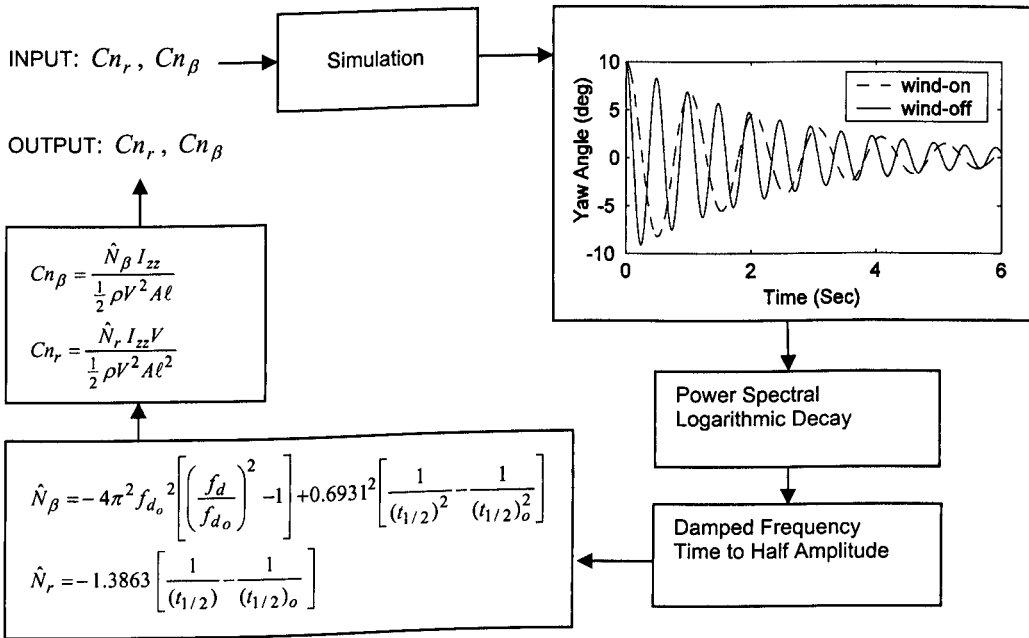
**Figure 5.1 Procedure of estimating the aerodynamic derivatives from simulated time response data.**

Figure 5.2 shows the time response plot used to estimate the damped frequency and rate of amplitude decay between wind-off and wind-on condition using a fourth order polynomial curve-fit for a 1 Hz wind-off oscillation frequency.
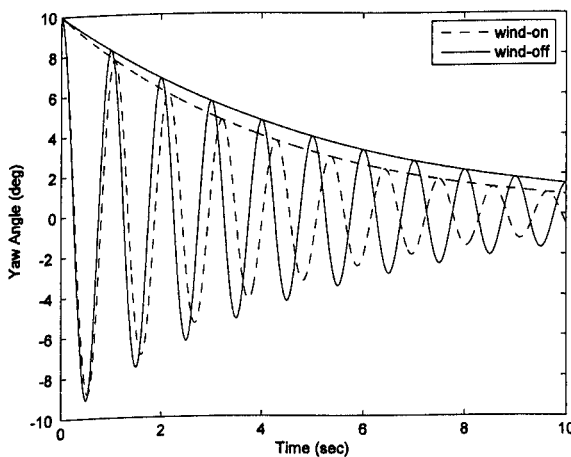
**Figure 5.2 Time response plot used to estimate the damped frequency and time to half amplitude.**

Table 5.1 shows the computed results from the wind-off and wind-on oscillation time response data using simulated values of Cn_β=0.3610, Cn_r=-0.1 and mechanical damping ratio 0.03 with a 1 kHz sampling rate.

	Wind-Off		Wind-On 10 m/s			
Freq. (Hz)	f_{d_o} (Hz)	$t_{1/2_o}$ (sec)	f_d (Hz)	$t_{1/2}$ (sec)	Cn_β	Cn_r
0.5	0.4998	7.3529	0.3507	5.0360	0.3610	-0.1003
1.0	0.9995	3.6765	0.9339	2.9885	0.3606	-0.1004
2.0	1.9992	1.8382	1.9670	1.6487	0.3624	-0.1003
3.0	2.9985	1.2250	2.9771	1.1377	0.3616	-0.1004
4.0	3.9984	0.9187	3.9825	0.8688	0.3577	-0.1004

Table 5.1 Computed aerodynamic derivatives from simulated time response data at 10 m/s.

The estimation of Cn_β becomes less accurate at higher oscillation frequencies. The accuracy can be improved by simply increasing the sampling rate of the simulation. The accuracy is also improved at higher tunnel speeds and this effect will be shown in the next section.

5.5 Parameters Affecting Estimation Accuracy

5.5.1 Effect of Mechanical Damping

The estimation of the aerodynamic derivatives is influenced by the data sampling rate and the mechanical damping ratio of the test rig. The estimation of yaw stiffness Cn_β and yaw damping Cn_r is largely influenced by the mechanical damping ratio.

Table 5.2 shows the results of the estimation by increasing the mechanical damping ζ_{off} to 0.1 at 10 m/s. Overall accuracy of the estimation is less when compared to Table 5.1 especially for Cn_r.

Freq.(Hz)	Wind-Off		Wind-On 10 m/s			
	f_{d_o} (Hz)	$t_{1/2_o}$ (sec)	f_d (Hz)	$t_{1/2}$ (sec)	Cn_β	Cn_r
0.5	0.4975	2.2256	0.3467	0.9890	0.3614	-0.0857
1.0	0.9950	1.1034	0.9285	1.0350	0.3610	-0.0960
2.0	1.9900	0.5513	1.9573	0.5324	0.3605	-0.0996
3.0	2.9851	0.3678	2.9630	0.3597	0.3636	-0.0980
4.0	3.9793	0.2767	3.9635	0.2721	0.3421	-0.0967

Table 5.2 Computed aerodynamic derivatives from simulated time response at 10 m/s with higher mechanical damping of 0.1.

The accuracy of the estimation is good if the mechanical damping is kept as low as possible (i.e. damping ratio of less than 0.03) and sampled at sufficient sampling rate. As in the actual experimental setup the maximum oscillation frequency is less than 4 Hz and the mechanical damping ratio ζ_{off} is less than 0.03, at 1 KHz sampling rate, the estimation accuracy is always within the given values shown in Table 5.1.

5.5.2 Effect of Tunnel Speed

The aerodynamic loads are small at lower tunnel speed and the test is therefore less sensitive to the difference between wind-off and wind-on frequency. Larger loads at high tunnel speed produce a distinct difference between the wind-off and wind-on damped frequency. Figure 5.3 and 5.4 show oscillations at 10 and 40 m/s for 2 Hz wind-off oscillation frequency.
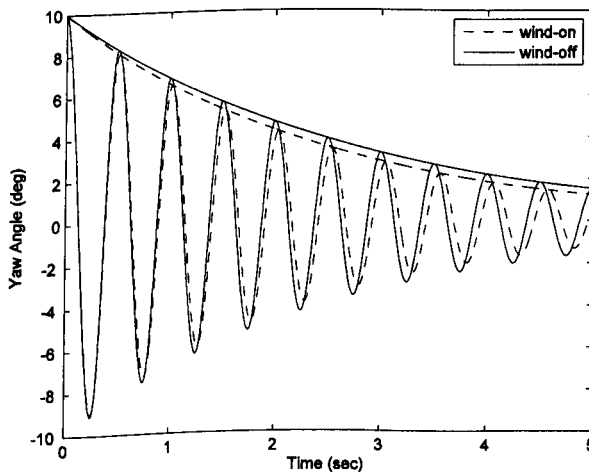
Figure 5.3 Simulated response at 10 m/s.
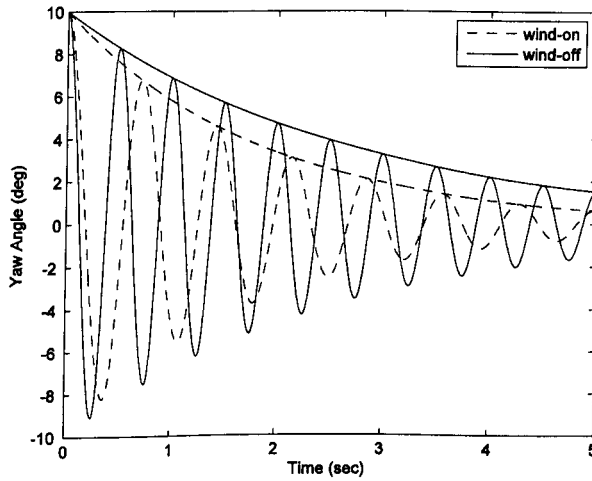
Figure 5.4 Simulated response at 40 m/s.

At 40 m/s the separation between the wind-off and wind-on is clearly seen, this can improve the estimation of the aerodynamic derivatives. Table 5.3 shows the results of the estimation performed at 40 m/s. Data at 0.5 and 1 Hz are not presented because of unstable divergent oscillations. By comparison to Table 5.1 the accuracy for Cn_β at 2, 3 and 4 Hz has improved.

Freq.(Hz)	Wind-Off		Wind-On 40 m/s			
	f_{d_o} (Hz)	$t_{1/2_o}$ (sec)	f_d (Hz)	$t_{1/2}$ (sec)	Cn_β	Cn_r
2.0	1.9992	1.8382	1.4027	1.2590	0.3611	-0.1003
3.0	2.9985	1.2250	2.6385	0.9376	0.3608	-0.1003
4.0	3.9984	0.9187	3.7355	0.7470	0.3612	-0.1003

Table 5.3 Computed aerodynamic derivatives from simulated time response data at 40 m/s.

5.5.3 Effect of Noise

The effect of noise on the estimation accuracy is evaluated by adding a random function in the oscillation data. Figure 5.5 and 5.6 show the effect of noise level on the time response and estimated derivatives. The noise level is quantified as a standard deviation in yaw angle disturbance. At low noise level shows in Figure 5.5 the estimated value of yaw moment derivative is good but the yaw damping derivative is poor.
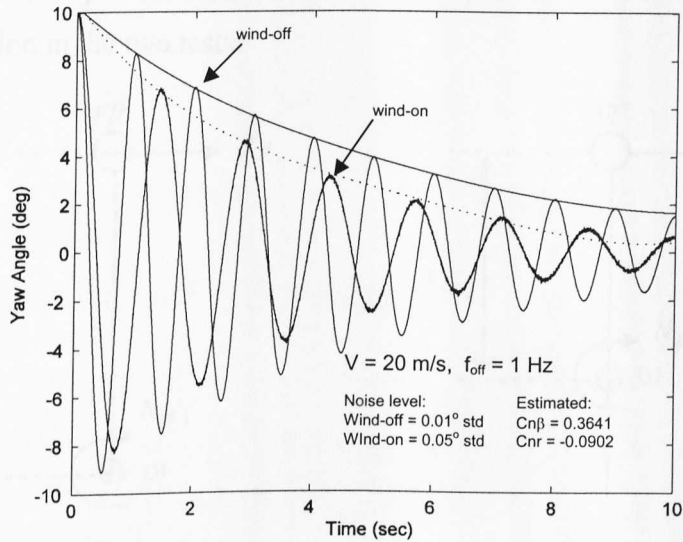
Figure 5.5 Computed aerodynamic derivatives from noisy time response data at 20 m/s.

With a further increase in the noise level shown in Figure 5.6, the error in Cn_β is of the order of 1%; however it is not possible to extract an accurate value of Cn_r.
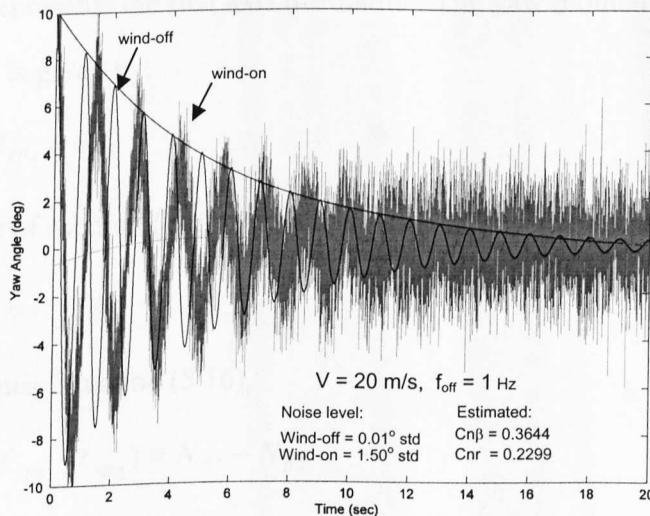
Figure 5.6 Computed aerodynamic derivatives from high level of noise of wind-on data at 20 m/s.

5.6 Estimation of Side Force Derivatives

The tests were conducted at two longitudinal positions of the axis of rotation of the model in order to enable the estimation of the side force derivatives (Cy_β and Cy_r). This is possible if it is assumed that the flow characteristics are the same for the two longitudinal positions and that it generates the same vector of side force stiffness Y_β

acting on the centre of pressure *cp*, i.e. the centre of pressure is assumed to be acting at the same location in the two tests.

(a)   (b)
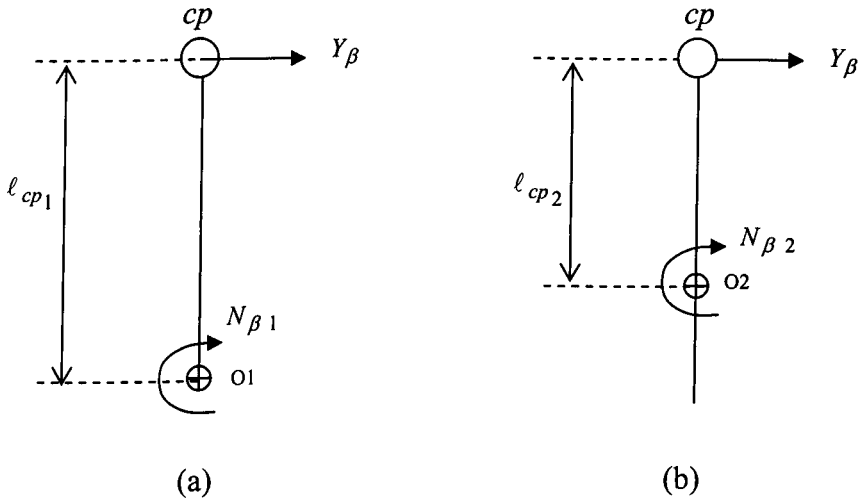
Figure 5.7 Two axis measurement allows estimation of the side force derivative.

Let Figure 5.7(a) represents the first axis of rotation. The yaw moment N_β about the reference point O1 is given by:

$$Y_\beta \, \ell_{cp_1} = N_{\beta 1} \tag{5.15}$$

For the second axis of rotation (Figure 5.7 (b)):

$$Y_\beta \, \ell_{cp_2} = N_{\beta 2} \tag{5.16}$$

Equation (5.15) minus Equation (5.16),

$$Y_\beta \, (\ell_{cp_1} - \ell_{cp_2}) = N_{\beta 1} - N_{\beta 2} \tag{5.17}$$

In coefficient term:

$$Cy_\beta \, \frac{(\ell_{cp_1} - \ell_{cp_2})}{\ell} = Cn_{\beta 1} - Cn_{\beta 2} \tag{5.18}$$

Then the formulation of the side force derivatives expression can be written as:

$$Cy_\beta = \frac{(Cn_{\beta 1} - Cn_{\beta 2})\ell}{\Delta \ell_{cp}} \tag{5.19}$$

By following the same procedure, the damping derivative of the side force is given by:

$$Cy_r = \frac{(Cn_{r1} - Cn_{r2})\ell}{\Delta\ell_{cp}} \qquad (5.20)$$

where $\qquad \Delta\ell_{cp} = \ell_{cp_1} - \ell_{cp_2}$ $\qquad\qquad\qquad$ (5.21)

5.7 Estimation of Centre of Pressure

Let the side force act about the centre of pressure cp at a distance of ℓ_{cp} from the rotation axis of the model O and N is the product of yaw moment about centre of rotation be described as shown in Figure 5.8.
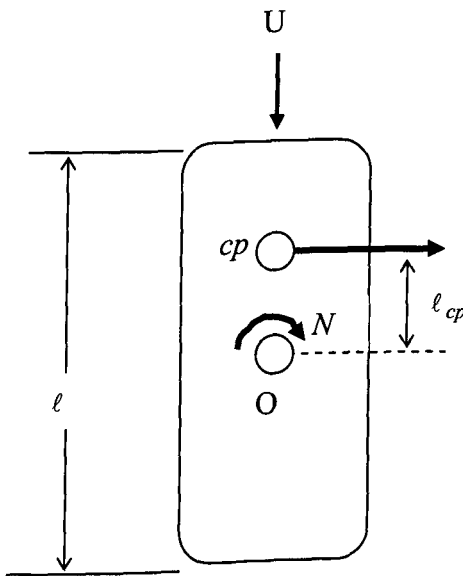
Figure 5.8 Determination of the centre of pressure.

$$N = Y \ell_{cp} \qquad (5.22)$$

for a non-dimensional value, divide Equation (5.22) by $\frac{1}{2}\rho V^2 A\ell$ such that:

$$C_n = C_y \frac{\ell_{cp}}{\ell} \qquad (5.23)$$

By differentiating Equation (5.23) with respect to C_y, the expression for the distance of the centre of pressure to the axis of rotation ratio to wheel base is given by:

$$\frac{dCn}{dCy} = \frac{\ell_{cp}}{\ell} \tag{5.24}$$

Then, this equation is equivalent to

$$\frac{dCn}{dCy} = \frac{dCn}{dC\beta} \cdot \frac{dC\beta}{dCy} \tag{5.25}$$

which can be used to estimate the location of the centre of pressure.

Chapter 6

Results and Discussions – Preliminary Studies

6.1 Introduction

Some initial results from the oscillating rig have been reported in Chapter 3 where they were necessary to explore the operation and repeatability of the facility. In this Chapter a series of test are repeated that concentrate on the behaviour of a single model configuration; the 20° slant angle Mansor and Passmore [44]. The specific objectives of this initial study are:

1) To test the method of extracting transient aerodynamic derivatives from the oscillating model data developed in Chapter 5.

2) To measure the aerodynamic magnification by comparing the transient with steady state measured derivatives. The steady state derivatives have been determined and presented in Chapter 4.

3) To extend the simulation of the dynamic behaviour reported in Chapter 2 and 4.

The 20° slant angle model was tested across 0.5 to 4 Hz frequency range (reduced frequency 0.09-0.8) at 10 to 40 m/s tunnel speed (Reynolds number $0.43x10^6$-$1.71x10^6$)

and the dynamic derivatives calculated for every test. Force and moment derivatives are reported covering the complete range (damped and self-sustained oscillation) while damping derivatives cover damped response only. Alternative methods based on a total energy calculation are used to quantify the transient response and unsteadiness in the self-sustained oscillation. The development of simulation to match the experimental data is also reported.

6.2 Dynamic Tests

6.2.1 Frequency Ratio

The frequency ratio ($f_{d_{on}}/f_{d_{off}}$) between wind-on and wind-off is shown again for all ten springs at a speed of 10 m/s in Figure 6.1. These are compared to the frequency ratio predicted from simulation with the aerodynamic stiffness derivative Cn_β taken from the steady state data at 10 m/s and zero aerodynamic damping. The difference at low reduced frequency arises because of the difference between the static and dynamic aerodynamic derivative. For reduced frequencies greater than about 0.4 the frequency ratio approaches unity and the simulated and experimental frequency ratios are in agreement.
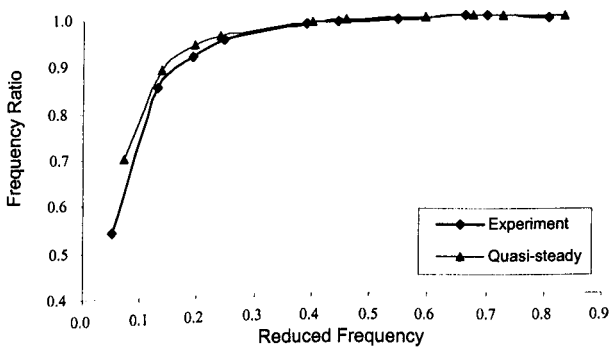
Figure 6.1 Frequency ratio at 10 m/s for all spring. Comparison between experiment and quasi-steady (20° slant).

Similarly, the frequency ratios at four tunnel speeds (10, 20 30 and 40 m/s) using springs (K5, K6, K7, K8, K9 and K10) are shown in Figure 6.2.
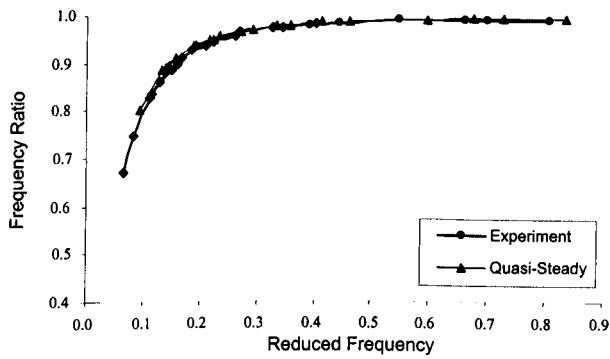
Figure 6.2 Frequency ratio at four speeds (10, 20 , 30 and 40 m/s) of six springs (K5, K6, K7, K8,
K9 and K10). Comparison between experiment and quasi-steady (20° slant).

6.2.2 Dynamic Yaw Moment Derivative

Figure 6.3 shows the dynamic measured yaw moment derivatives calculated using the
method describing in Section 5.2 at four tunnel speeds (10, 20 30 and 40 m/s) using
springs (K5, K6, K7, K8, and K9) from four repeat tests.
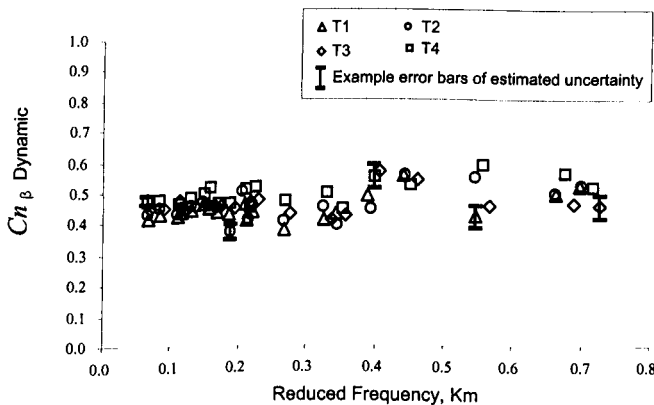
Figure 6.3 Yaw moment derivative against reduced frequency from four repeat tests (20° slant).

In the figure the yaw moment derivatives are plotted against reduced frequency between
0.07 and 0.72. This reduced frequency range is equivalent to wavelengths of the order of
45 to 4 times the body length. The dynamic yaw moment derivative has no significant
trend with reduced frequency. However, it is noticeable that the values seem to increase
slightly above reduced frequencies of about 0.2 and show a slight drop at high reduced
frequencies. The yaw moment derivative is consistent at reduced frequencies lower than
about 0.2. For all reduced frequencies the yaw moment derivatives are well above the
static values reported in Section 4.2.1 (Table 4.1). The estimated uncertainty shown by
the error bars has been calculated using those inputs to the derivative calculation that

contribute to test-to-test variation. Systematic errors (e.g. moment of inertia) are not included as they do not affect this test-to-test variation.

6.2.3 Yaw Damping Derivative

The calculated yaw damping derivative Cn_r determined from those tests exhibiting damped response are shown in Figure 6.4 from three repeat tests at 10 m/s and Figure 6.5 at 15 and 20 m/s.
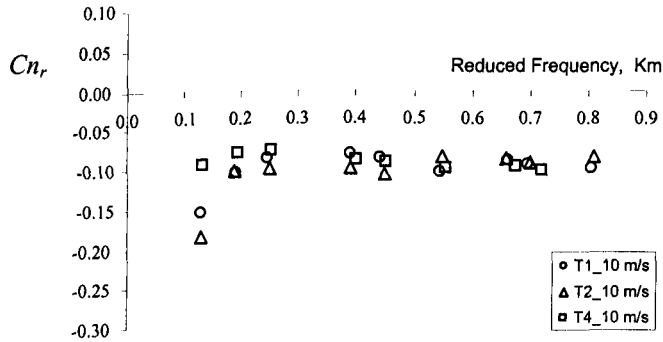
***Figure 6.4 Yaw damping derivative against reduced frequency at 10 m/s
of three repeat tests (20° slant).***
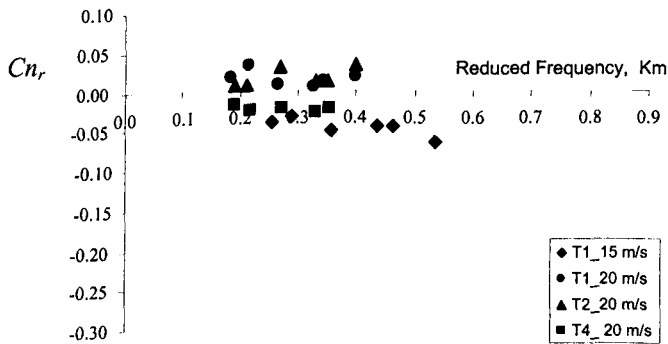
***Figure 6.5 Yaw damping derivative against reduced frequency at 15 and 20 m/s
of three repeat tests (20° slant).***

The yaw damping derivative in Figure 6.4 and 6.5 is generally small apart from at the lowest speed and reduced frequency. In Figure 6.5 at a speed between 15 and 20 m/s the sign of the yaw damping derivative is seen to become positive. It is suggested that the reduction in yaw damping derivative with increasing speed arises as the strength of the vortex shedding increases. The positive yaw damping value arises because the vortex shedding essentially drives the oscillation. However, whilst this effect is relatively small

the overall response remains damped because of the influence of the mechanical damping, it is this effect that makes it possible to extract the value of aerodynamic yaw damping from the time series. At a speed of 10 m/s the yaw damping derivative from three repeat tests (T1, T2 and T4) is consistent for all reduced frequencies above 0.25. This is consistent with the effect of oscillation frequency on damping ratio in Figure 3.17 (in Section 3.7). However, at a speed of 20 m/s the sign of the yaw damping for the first test series (T1 and T2) is inconsistent with the third (T4). This is because this speed range is close to the cross-over speed when the self-sustained oscillation is about to occur. Within this cross-over speed the estimation of yaw damping becomes erratic due to the unsteadiness in the response of the model. As the aerodynamic yaw damping derivative is very small at the cross-over speed it shows that the wind speed at which self-sustained oscillation occurs is influenced by the wind-off damping (i.e. mechanical) and is therefore a result of the rig design and not in itself a particularly significant aerodynamic effect.

6.2.4 Effect of Reynolds Number and Non-Zero Yaw Oscillation

The yaw moment derivative is plotted again in Figure 6.6 but in this case against Reynolds number (based on model length). For all oscillation frequencies (springs) the yaw moment derivative reduces as Reynolds number increases and becomes almost constant above about 1×10^6.
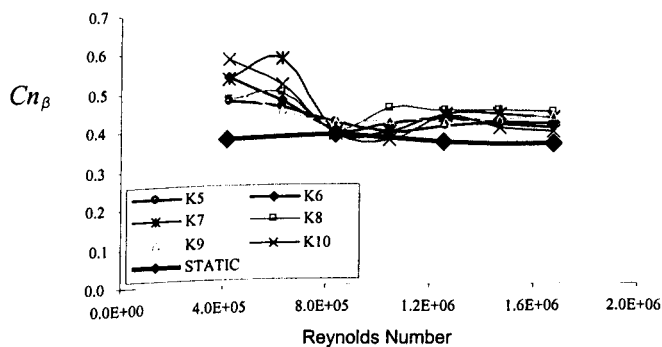
Figure 6.6 Yaw moment derivative against Reynolds number (20° slant).

It is seen that the dynamic measured Cn_β exceeds the static value for all Reynolds numbers. The dynamic Cn_β seems to be close to the static value at a Reynolds number of 1×10^6 and at higher Reynolds number the transient yaw moment derivative consistently exceeds the steady state value by as much as 25%.

As the behaviour appears, from these results, to be reasonable consistent above a Reynolds number of 10^6 it may be concluded that a single test at higher Reynolds numbers is sufficient to characterise the transient behaviour. The higher Reynolds numbers are also much closer to those experienced in practice for a road vehicle, and a Reynolds number of 10^6 often suggested as a minimum for basic model scale testing.

In Figure 6.7, the yaw damping derivatives seen in Figure 6.5 are plotted against Reynolds number. The cross over point at 8.5×10^5 is 'arbitrary' because it depends on the level of mechanical damping, however it is assumed the trends would be remain unchanged should the level of mechanical damping be altered.
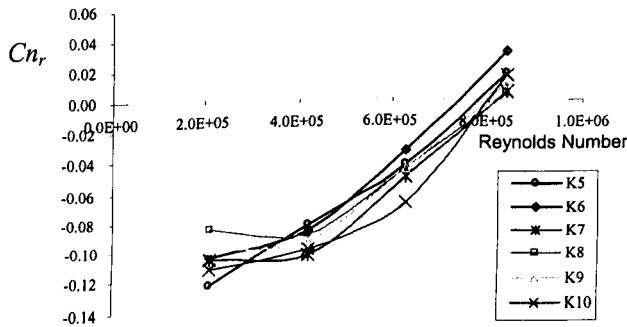
Figure 6.7 Yaw damping derivative against Reynolds and wind speed (20° slant).

Oscillation of the model about a non-zero yaw angle does not affect these derivatives provided that the off-set yaw angle is maintained below 8°.

6.2.5 Dynamic Side force Derivative

The transient side force derivative Cy_β was determined using the measurement from two longitudinal positions of the axis of rotation. The second axis is positioned 50 mm forward of the original centre axis. The equation to calculate the side force from two measurements of Cn_β is given by:

$$Cy_\beta = \left[(Cn_\beta)_{mid} - (Cn_\beta)_{front} \right] \frac{\ell}{\Delta\ell} \qquad (6.1)$$

The subscripts '*front*' and '*mid*' represent the front and centre axes while $\Delta\ell$ is the longitudinal distance between the two axes. The derivation of Equation (6.1) can be found in Section 5.6.

It was found that the overall values of Cn_β measured using the front axis were less than those measured using the mid axis by between 40 and 50%. The smaller yaw moment derivative arises as a consequence of bringing the axis of rotation closer to the centre of pressure. From the static tests the centre of pressure is located at about 150 mm (24% model length) ahead of the mid axis. By moving the axis of rotation to 50 mm ahead of the mid axis, this reduces the distance between the centre of pressure and axis of rotation to approximately 100 mm. Figure 6.8 shows the comparison of the frequency ratio between the two axes plotted against reduced frequency. For the same reduced frequency, the frequency ratio from the front-axis is higher than that from the mid-axis and reaches unity faster than the mid-axis. For reduced frequencies greater than about 0.4 the frequency ratio approaches unity and the frequency ratios are very similar for the two axes. The dynamic measured side force derivative is shown in Figure 6.9.
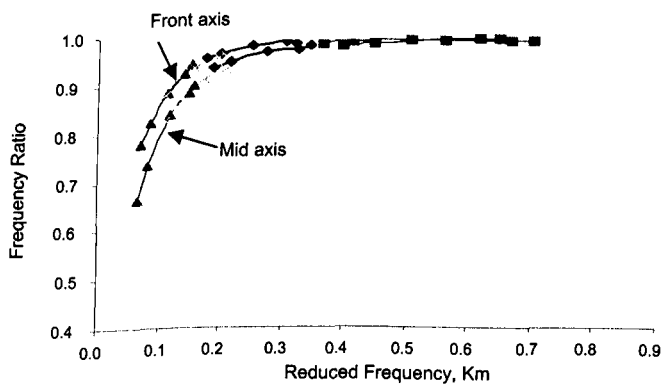
Figure 6.8 Comparison of frequency ratio between the mid-axis (M-axis) and front-axis (F-axis) of rotation (20° slant).
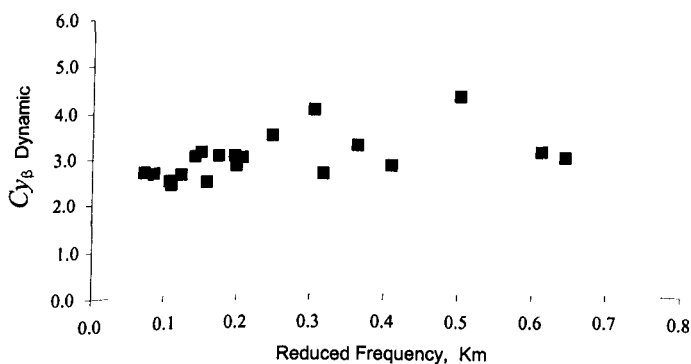
Figure 6.9 Dynamic measured side force Cy_β versus reduced frequency (20° slant).

As seen in the yaw moment derivative, the side force derivative seems to increase slightly with increasing reduced frequency and shows large variation at higher reduced frequencies of more than 0.2.

6.2.6 Side Force Damping Derivative

Using the same approach the side force damping Cy_r can be estimated from the two measurements of yaw damping derivatives $(Cn_r)_{mid}$ and $(Cn_r)_{front}$. The results are shown in Figure 6.10.
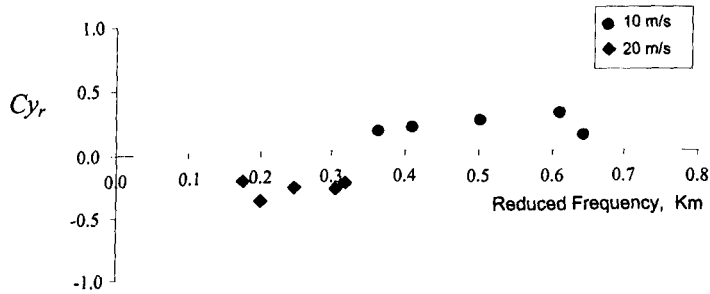
Figure 6.10 Side force damping derivative (20° slant).

At low reduced frequency Cy_r shows very small values which are generally less than zero. As reduced frequency increases Cy_r changes its sign from negative to positive at a reduced frequency of 0.4. Above this the side force damping shows a positive value.

6.3 Magnification of Yaw Moment and Side Force Derivatives

The aerodynamic magnification factor can be determined by simply taking the ratio of derivatives of the transient to the steady state measurements. For example the yaw moment magnification factor is given by:

$$\text{Yaw moment magnification factor} = \frac{Cn_{\beta_{dynamic}}}{Cn_{\beta_{static}}} \qquad (6.2)$$

The results are summarised in Figure 6.11. Using the ratio of dynamic to static derivative allows an assessment of the impact of transient aerodynamics. Values greater than one therefore show that a simple static test will underestimate the aerodynamic loads. When calculating magnification the static derivatives must be for the same Reynolds number as the dynamic test. This is important because for some model configurations the aerodynamic derivatives are sensitive to Reynolds number.

The results are compared with those obtained by Passmore et al. [54]. For all reduced frequencies the magnification is greater than unity, in some instances by as much as 50%. The data of Passmore et al. [54] shows good agreement for reduced frequencies below about 0.4. Above this the data of Passmore shows somewhat lower values. It should be noted that these results are produced from two quite different transient simulations and that although the tests are on the same model, they have been obtained in different wind tunnels with different flow quality, blockage ratios and over different yaw angle ranges. It is also noted that in some cases the gust amplitude used in the test by Passmore et al. [54] is less than $\pm 2°$, which may affect the overall signal-to-noise ratio.
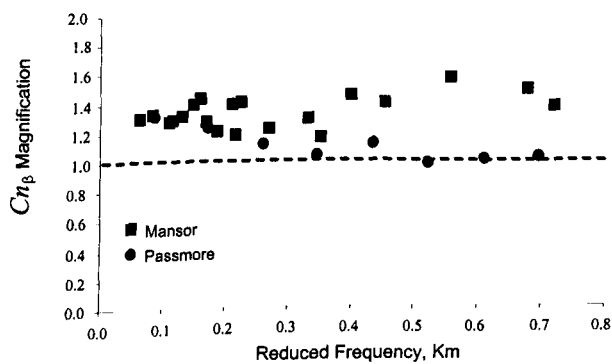
**Figure 6.11 Yaw moment derivative magnification (20° slant).**

The results are not in agreement with Bearman and Mullarkey [8] as in their work the yaw moment admittance was less than unity for 20° slant angles. In the analysis performed in that work the quasi-steady response was calculated using a single value of the static derivative. As in Figure 4.2 and Table 4.1 it is clear that the static yaw moment derivative does not vary considerably with Reynolds number but it is not the case for side force. If the derivative varies considerably with Reynolds number in the static tests, recalculating the results presented here assuming a single value of static derivative has a significant effect.

Figure 6.12 summarises all the side force aerodynamic derivative results. As for previous results the data is represented in the form of a magnification factor, $Cy_{\beta_{dynamic}} / Cy_{\beta_{static}}$.
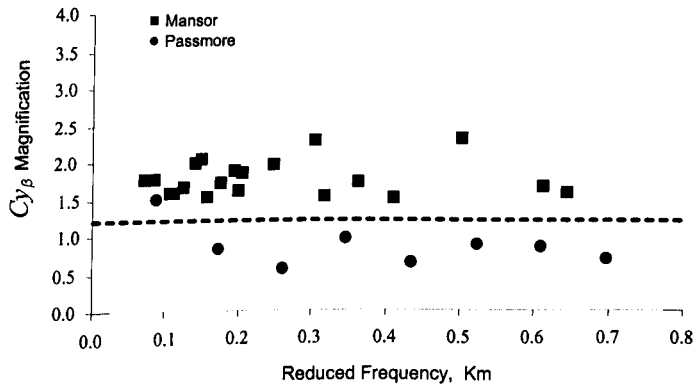
Figure 6.12 Side force derivative magnification (20° slant).

The magnification of side force derivative is greater than unity for all reduced frequencies. For reduced frequencies below 0.2 the magnification is between 1.5 and 2.0. Higher reduced frequencies show large variations ranging from unity to over 2.0. This is contrary to the experience of Passmore et al. [54] whose transient side force is generally significantly less than the static value except for the lowest frequency tested. However, the results obtained for this investigation are more consistent with the past experience of Ryan and Dominy [59] whose transient side force is greater than the predicted steady state value by 18%. Again, it should be noted that these results are produced from two different methods of transient simulations.

6.4 Development of Simulation–Application of Dynamic Derivatives

6.4.1 Damped Oscillation

Figure 6.13 shows the time and frequency response of the model for spring K5 at 10 m/s. The simulation builds on the basic quasi-steady version reported in Section 4.4 but the static derivatives are replaced with the measured dynamic yaw moment derivative. The simulation time response shows a less damped response compared to measured data.

With the addition of aerodynamic damping, Figure 6.14 demonstrates that the simulation of the same model and spring matches the frequency of oscillation and rate of the amplitude decay well.

An important conclusion obtained from the simulation (refer to Figure 6.13 and 6.14) is that the rate of amplitude decay that occurred in the measured data cannot be matched using a simulation without aerodynamic damping. The power spectral density of the

linear simulation in both figures does not match the measured data. This could suggest an indication that some nonlinearity has influenced the measured data, Silva et al. [64].
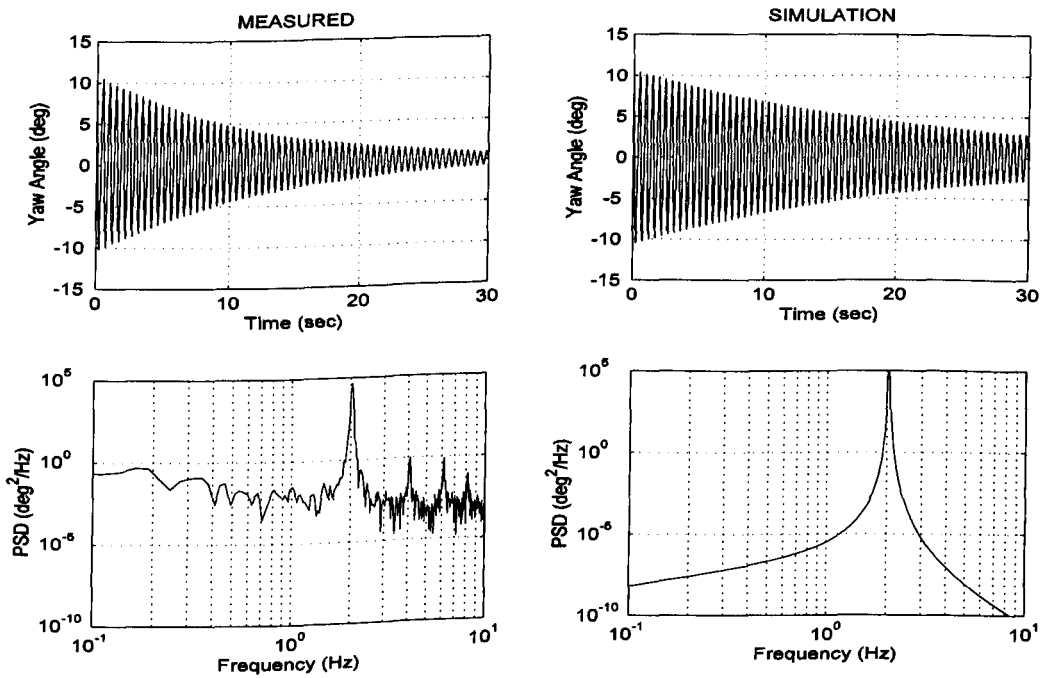
Figure 6.13 Comparison between measured and simulation results for spring K5 at 10 m/s using measured dynamic yaw moment derivative without aerodynamic damping.
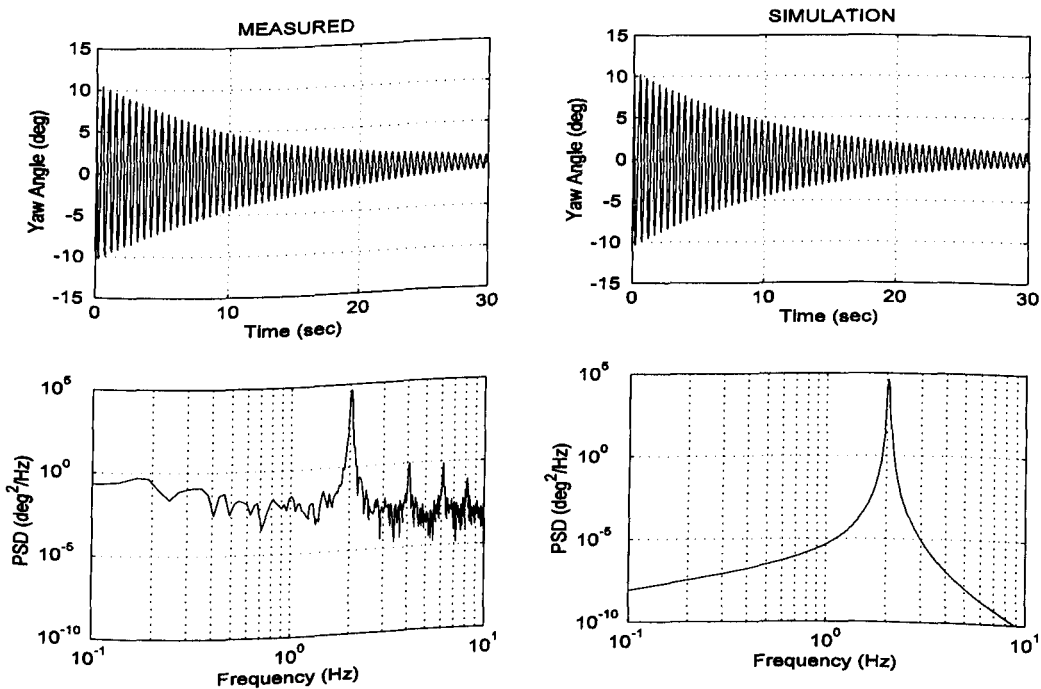
Figure 6.14 Comparison between measured and simulation results for spring K5 at 10 m/s using measured dynamic yaw moment derivative with aerodynamic damping.

6.4.2 Self-Sustained Oscillation

Figure 6.15 shows the time and frequency responses of the same model and spring but at a speed of 40 m/s. The simulation no longer includes an aerodynamic damping term because one cannot be determined from the self-sustained measured data.
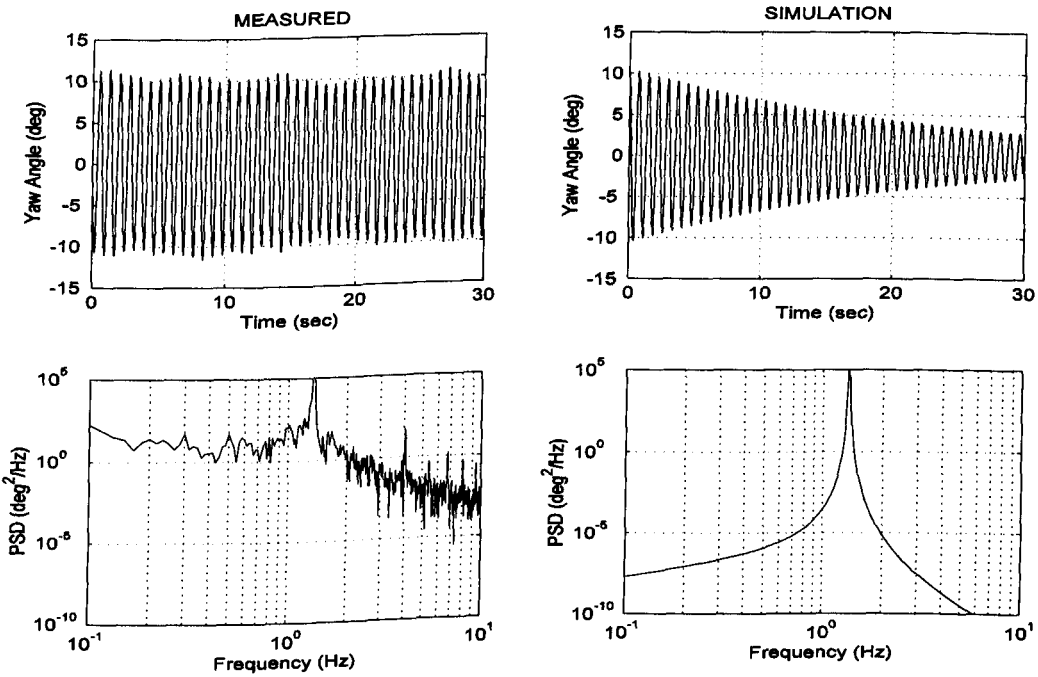
Figure 6.15 Comparison between measured and simulation results for spring K5 at 40 m/s using measured dynamic yaw moment derivative without aerodynamic damping.

The simulation in this form does not produce the self-sustained oscillation seen in the measurements. However with the addition of an artificial aerodynamic damping derivative it can be shown that self-sustained oscillation actually occurs when the aerodynamic damping cancels out the mechanical damping (i.e. the effective damping ratio in the system is assumed zero). This is consistent with the results seen in Figure 6.4, 6.5, 6.6 and 6.7 and confirms the conclusion that the speed at which self-sustained oscillation occurs is a function of the rig design and is not a significant aerodynamic effect.

Figure 6.16 compares the simulated response of the equivalent zero damping ratio system with the measured results during a self-sustaining oscillation. The self-sustained oscillation is evident but does not predict the unsteadiness seen in the self-sustaining responses. It is also evident that at higher wind speeds the unsteadiness is increasing in the experimental data. Referring back to Figure 6.6 it was proposed that above a

Reynolds number of 10^6 the behaviour is essentially consistent as the derivative is approximately constant. However the result from Figure 6.15 suggest that this is not the case and that further analysis is required.
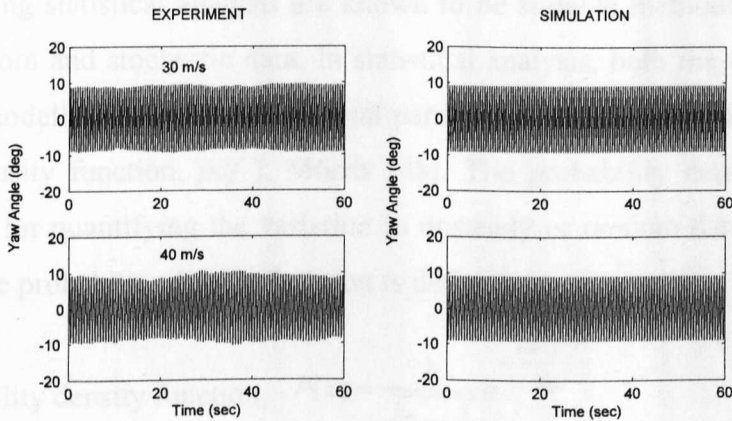
Figure 6.16 Comparison between measured and simulated time responses during self-sustained oscillation (spring K5).

The effect of harmonics can be seen in the power spectral density plot in both Figure 6.14 and 6.15. However, they occur at relatively low energies compared to the fundamental frequency. This phenomenon is not investigated further here but is a clear subject of interest for future research.

6.5 Unsteadiness in Self-Sustained Oscillation

Both the self-sustained and self-excited oscillation suggested that the existence of external effects such as wake buffeting or asymmetric vortex formation is exciting the model to produce a flow-induced oscillation. However, in addition to the regular oscillation of the model it was evident that some general unsteadiness existed and that this increased with increasing wind speed. This result is important because the yaw moment derivative was shown to be reasonably constant above Reynolds numbers of approximately 10^6, suggesting consistent aerodynamic performance but the increasing unsteadiness suggests that the derivatives provide an incomplete picture.

The simulation reported in Section 6.4 captured the fundamental frequency well and also showed that the self-sustained oscillation occurs when the aerodynamic damping cancels out the mechanical damping. However, the simulation did not predict the unsteadiness in amplitude seen in the self-sustaining response.

6.5.1 Statistical Analysis, Power Spectral and Phase-Plane Plot

Initial observation of the time response plot can give early indications of the relative unsteadiness; however, it cannot be quantified simply by observation. Probabilistic approaches using statistical analysis are known to be suitable methods for dealing with unsteady, random and stochastic data. In statistical analysis, both the excitation and the response are modelled in terms of statistical parameters (e.g. root-mean-square, *rms* and probability density function, *pdf*), Morris [48]. The probability density function is a useful method for quantifying the variation in unsteady or random data. For a Gaussian distribution, the probability density function is defined as:

$$\text{Probability density function,} \quad P(x) = \frac{1}{\sqrt{2\pi\sigma^2}} e^{-\frac{(x-m)^2}{2\sigma^2}} \tag{6.3}$$

where m is the mean value and σ is the standard deviation. The standard deviation σ is given by:

$$\text{Standard deviation,} \quad \sigma = \sqrt{\frac{1}{n}\sum_{i=1}^{n}(x_i - m)^2} \tag{6.4}$$

Figure 6.17 shows an example of a *pdf* plot. For consistency, the calculation of the *pdf* for each self-sustained oscillation contains the same number of sampled data points. The figure shows the *pdf* plot for 20° slant model using springs K05 to K09 at 40 m/s.
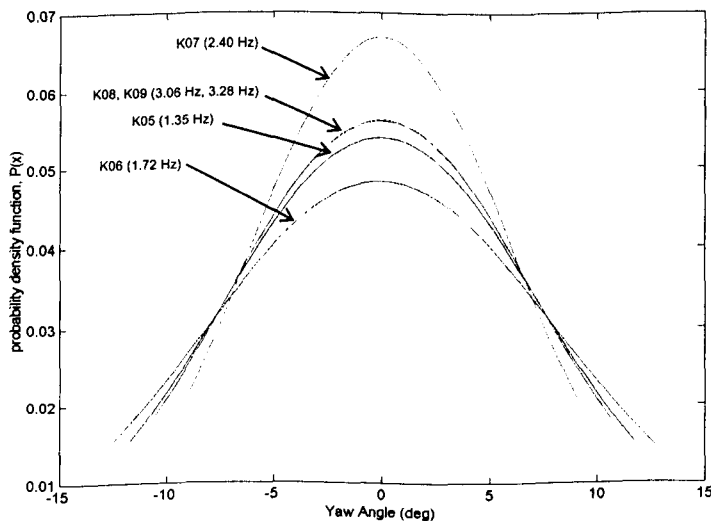
Figure 6.17 Effect of spring stiffness on pdf at 40 m/s.

The distribution of the *pdf* shows no clear correlation or relationship with oscillation frequency. This indicates a nonlinear relationship between the distributions of the *pdf* (i.e. yaw angle) and oscillation frequency.

The simulated results seen in Figure 6.15 are repeated here in Figure 6.18 with the addition of *pdf* and *phase-plane* plots. The *phase-plane* plot is a two dimensional graph with displacement and velocity, respectively, on the x and y axes [12]. Therefore the graph can express the simple behaviour of an oscillatory system.
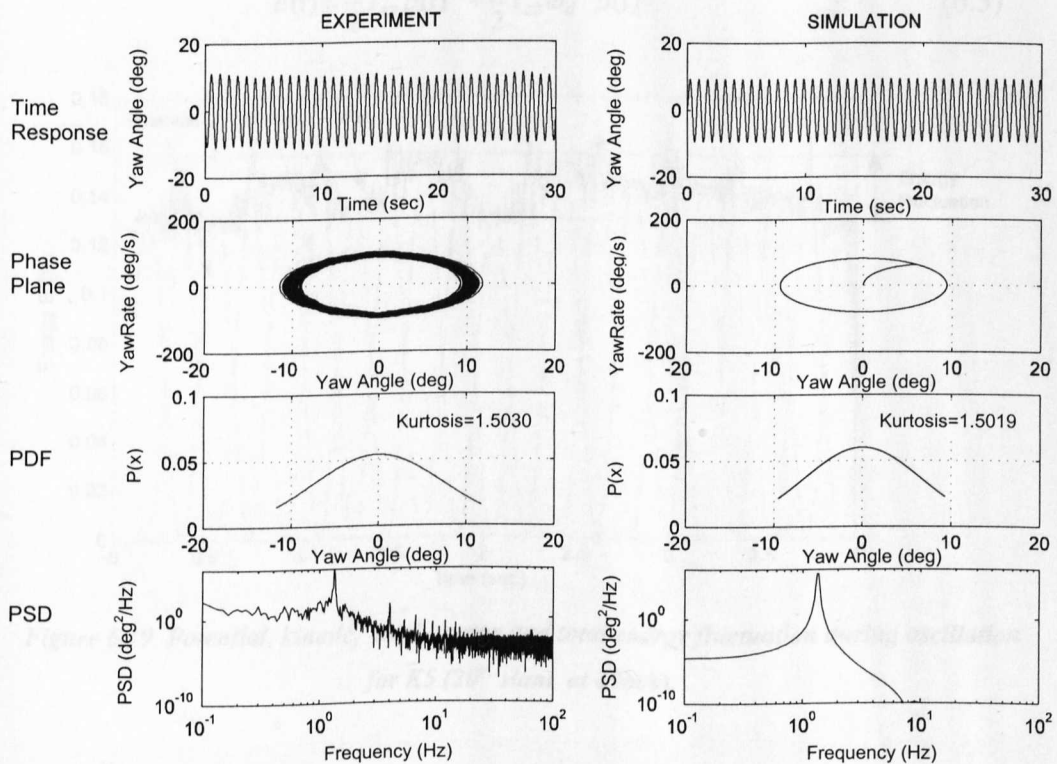
Figure 6.18 Self-Sustained oscillation with pdf and phase-plane plots for K5 (20° slant at 40 m/s).

From the *pdf* plots in Figure 6.18 the simulation does not matched the experimental data, whereby the experimental curve is flatter than the simulated result. The *phase-plane* plot demonstrated that the essential amplitude-velocity information in the simulation is correct but the unsteadiness that exists in the experimental data is evident by the spread in both amplitude and velocity.

The *pdf* and *phase-plane* plot in Figure 6.18 illustrate the unsteadiness but difficult to quantify the effect from the experimental data. The *pdf* and *phase-plane* plots are useful indication of the unsteadiness and allow a simple comparison of experiment and

simulation but are not a good means of quantifying the levels of unsteadiness between different experiments. This prompts the use of an energy method.

6.5.2 Total Energy Calculation

The unsteadiness of the data can be quantified using the total energy of the oscillation. This is achieved by considering the intensity of the unsteady component through the sum of the kinetic and potential energies of the oscillation, *E(t)*.

$$E(t) = \frac{1}{2} I_{zz} \dot{\beta}(t)^2 + \frac{1}{2} I_{zz} \omega_d^2 \beta(t)^2 \qquad (6.5)$$
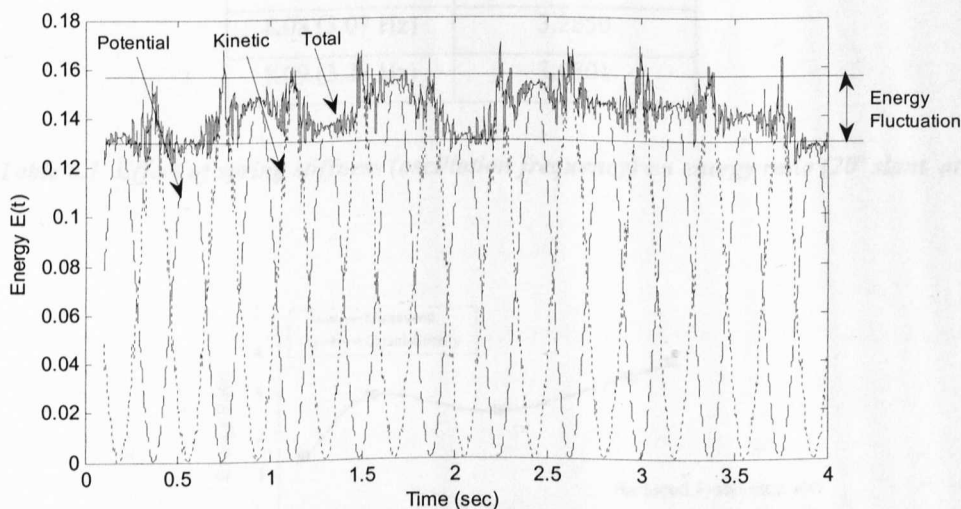
Figure 6.19 Potential, kinetic, total energy and total energy fluctuation during oscillation for K5 (20° slant at 40m/s).

The variation of potential energy is a function of yaw angle and the variation of kinetic energy is a function of yaw velocity determined by differentiating the yaw angle with respect to time. Figure 6.19 shows a sample plot of the variation of potential, kinetic and total energy during the oscillation of the 20° slant model at 40 m/s using spring K5 (1.35 Hz). It is also evidence of fluctuation in total energy during the oscillation.

To remove the effect of varying spring stiffness which alters the underlying amplitude-velocity of the oscillation the results must be normalised using the wind-off energy to form the energy ratio. The wind-off measurement produces a damped oscillation so the energy is determined between ±10° and ±1°.

$$\text{Energy ratio,} \quad = \frac{\sum E(t)_{on} - \sum E(t)_{off}}{\sum E(t)_{off}} \qquad\qquad (6.6)$$

Figure 6.20 and Table 6.1 show the calculated energy ratio for the $20°$ slant angle for spring K5 to K9.

Springs	$\dfrac{E(t)_{on} - E(t)_{off}}{E(t)_{off}}$
K05 (1.35 Hz)	1.3762
K06 (1.72 Hz)	2.8262
K07 (2.40 Hz)	2.4099
K08 (3.07 Hz)	3.2850
K09 (3.28 Hz)	3.6801

Table 6.1   *Effect of spring stiffness (oscillation frequency) on energy ratio ($20°$ slant at 40 m/s).*
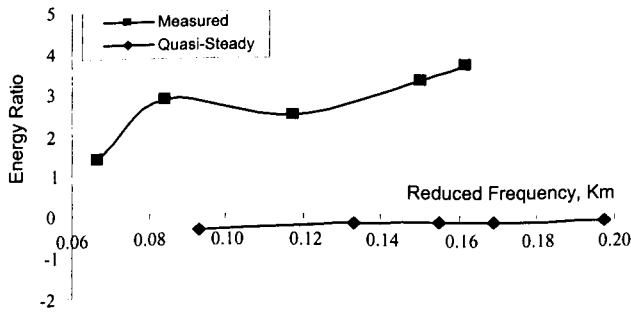
Figure 6.20   *Energy ratios against reduced frequency for $20°$ slant at 40 m/s. Comparison between measured and quasi-steady.*

The variation in energy ratio with reduced frequency in Figure 6.20 shows a nonlinear trend, though overall energy ratio increases with increasing reduced frequency. The energy ratio determined from the quasi-steady predicted responses are also plotted in the same figure. In quasi-steady analysis the energy ratio is always negative because the total energy of the wind-on is always less than wind-off. The damped amplitude in the wind-on oscillation means the wind-on potential energy is always less than the wind-off, while the reduction in wind-on frequency makes the wind-on kinetic energy always less than wind-off. It should be noted that the quasi-steady energy ratio leads to zero as reduced frequency increases which indicates the absent of unsteadiness.

6.5.3 Power Spectral Density Ratio

An alternative technique to the energy ratio method is to use the power spectral density ratio. In this case the variance of the fluctuation in aerodynamic load over the entire frequency range can be deduced from the integral of the power spectral density of the yaw angle as depicted in Figure 6.21, Zan and Richard [76], Newland [53]. A high integral value of the power spectral density signifies a large degree of unsteadiness in a given aerodynamic load, whereas a zero integral indicates a steady aerodynamic load.
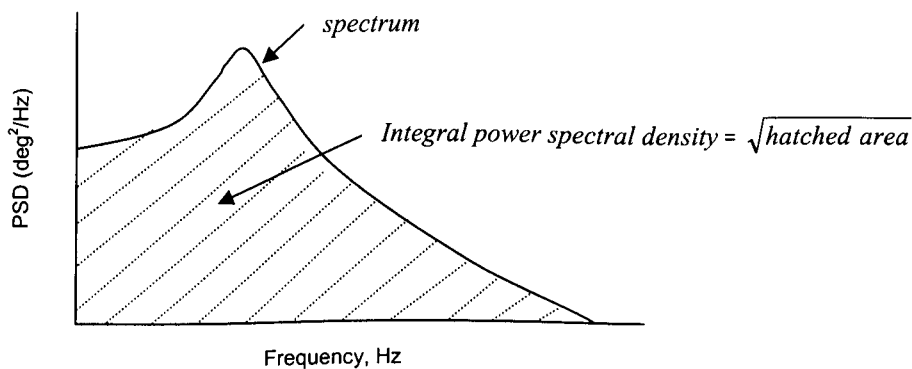
Figure 6.21 Computing of the integral power spectral density over the entire frequency.

As in the energy ratio, the results must be appropriately normalised:

$$\text{Power ratio} = \frac{Power_{on} - Power_{off}}{Power_{off}} \qquad (6.7)$$

Table 6.2 shows the power ratio against reduced frequency of 20° slant for spring K5 to K9.

Spring	$\dfrac{Power_{on} - Power_{off}}{Power_{off}}$
K05	9.3750
K06	14.3829
K07	11.7519
K08	11.7061
K09	13.6320

Table 6.2 Effect of spring stiffness (oscillation frequency) on power ratio (20° slant at 40 m/s).

Figure 6.22 shows the comparison results between energy ratio and power ratio.
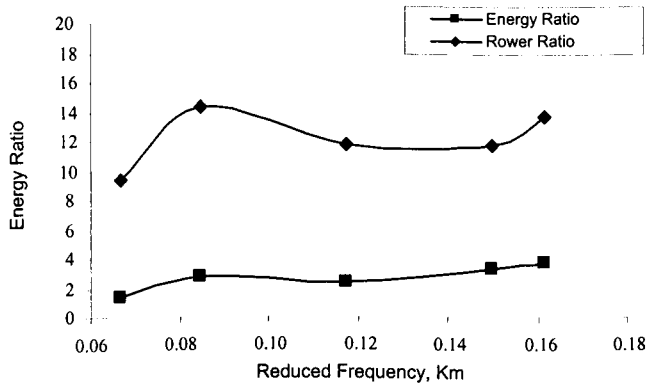
Figure 6.22 Power ratio against reduced frequency (20° slant at 40 m/s). Comparison with energy ratio.

The power ratio shows a similar trend to the energy ratio and therefore does not appear to provide new information. In addition the energy ratio calculation is more sensitive giving an increase over the reduced frequency range of 2.6 times compared to an increase in power ratio of approximately 50%. Therefore the energy ratio is used in all further analysis.

6.6 Development of Simulation –Addition of Unsteady Components

Using the results from Section 6.5 and 6.5.1 the simulation can be further improved by including an unsteady component. In Chapter 2 a general model to describe the motion was proposed in Equation (2.1) and (2.2) and it is repeated here for clarity:

$$\underbrace{I_{zz}\ddot{\beta}+C_r\dot{\beta}+K_r\beta}_{rig\ mechanical} = \underbrace{N_{dynamic}}_{\substack{linearised\\aerodynamic\\derivatives}} + \underbrace{N_{unsteadiness}}_{\substack{turbulent\ wake\\or\\buffeting}} \tag{6.8}$$

The dynamic terms have been considered via the aerodynamic derivatives and by substituting $N_{dynamic} = C_a\dot{\beta}+K_a\beta$ into Equation (6.8), gives:

$$I_{zz}\ddot{\beta}+(C_r-C_a)\dot{\beta}+(K_r-K_a)\beta = N_{unsteadiness} \tag{6.9}$$

The unsteadiness is introduced into the simulation as an input of band-limited white noise to represent fluctuation in lateral velocity V_f which results in the fluctuation in yaw angle β_f, yaw rate r_f, and yaw moment N_f. The simulation diagram is shown in Figure 6.23.
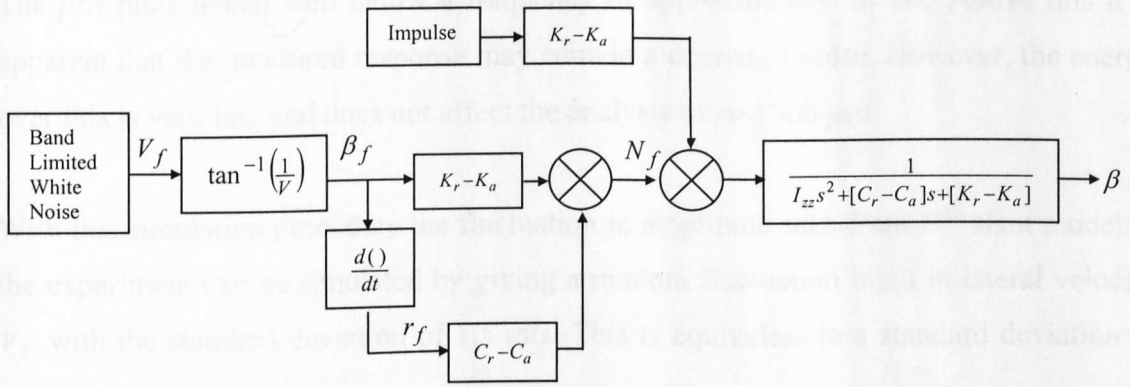
Figure 6.23 Simulation block diagram of self-sustained model with band-limited white noise to represent unsteadiness.

A suitable energy level of the band-limited white noise is applied to match the measured value of time response and power spectral density and optimised qualitatively using the *phase-plane* plot and *statistical* analysis. Figure 6.24 shows the agreement between measurement and simulation with band-limited white noise for the yaw responses in time and frequency domain.
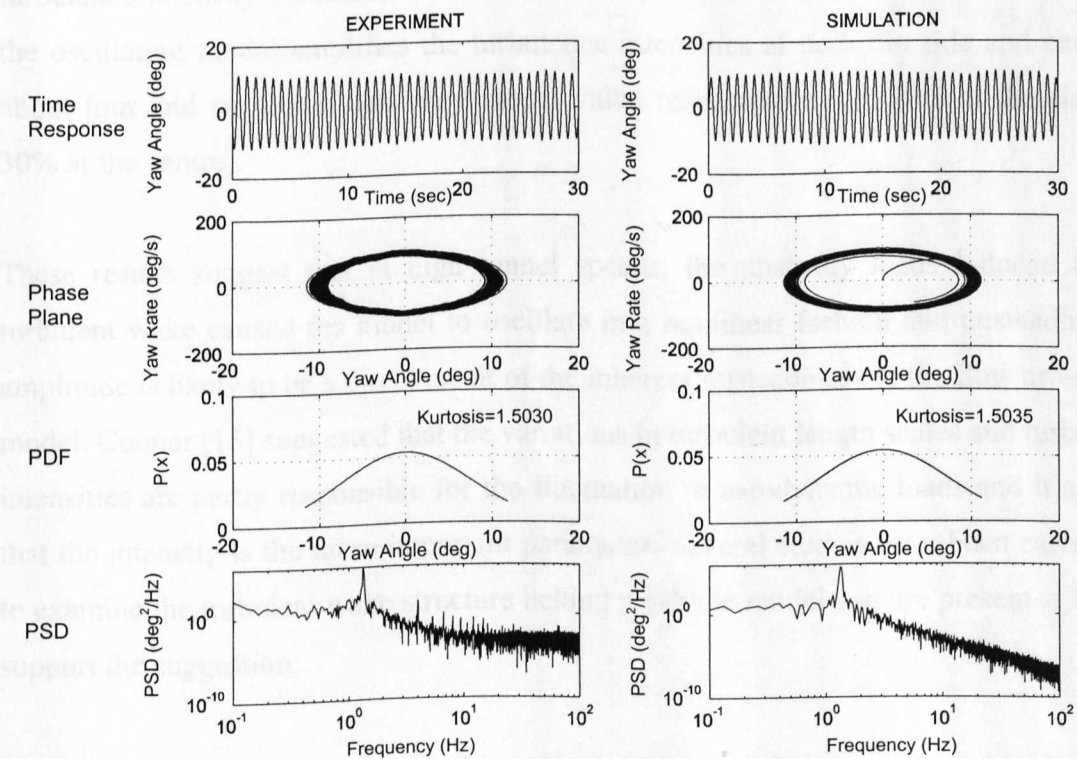
Figure 6.24 Measured and simulated with band-limited white noise of yaw responses in time domain and frequency domain for K5 (20° slant at 40 m/s)

The *psd* plots match well below a frequency of approximately 10 Hz. Above this it is apparent that the measured response may contain a degree of noise. However, the energy over this is very low and does not affect the analysis of *rms* and *psd*.

With this simulation procedure the fluctuation in amplitude seen from 20° slant model in the experiment can be simulated by giving a random fluctuation input in lateral velocity V_f with the standard deviation of 1.5 m/s. This is equivalent to a standard deviation of fluctuation in yaw angle β_f and disturbance torque T_f of 2.1° and 0.26 Nm respectively. By calculating the ratio between the standard deviation of fluctuation to the mean value of the total energy, the fluctuation in total energy seen for spring K5 at 40m/s is about 19%.

The fluctuation in the free stream velocities were checked from measurements taken via hot-wire mounted at 396 mm downstream from the back of the model (i.e. $x/\ell = 0.634$), and traversing along the mid-model height from the centre to side of the model. The turbulence intensity measured from the stationary model is around 5%. The wake from the oscillating model amplifies the turbulence intensities at both the side and centre to about four and six times stationary model value respectively (i.e. 20% at the side and 30% at the centre).

These results suggest that at high tunnel speeds, the unsteady loads induced by the turbulent wake caused the model to oscillate in a nonlinear fashion and unsteadiness in amplitude is likely to be a direct result of the inherent unsteadiness in the flow around the model. Cooper [15] suggested that the variations in turbulent length scales and turbulence intensities are partly responsible for the fluctuation in aerodynamic loads and it appears that the intensity is the more important parameter. Several studies have been carried out to examine the turbulent wake structure behind a vehicle model and are presented here to support the suggestion.

Ahmed [1] investigated the cross-flow velocity V_{yz}/V (resultant of lateral and vertical velocity components divided by freestream velocity) in the wake central plane of a fastback model and quoted values of approximately 28% at $x/\ell = 0.48$ (refer to Figure 6.25). The corresponding value for the estate model approximately 18%.
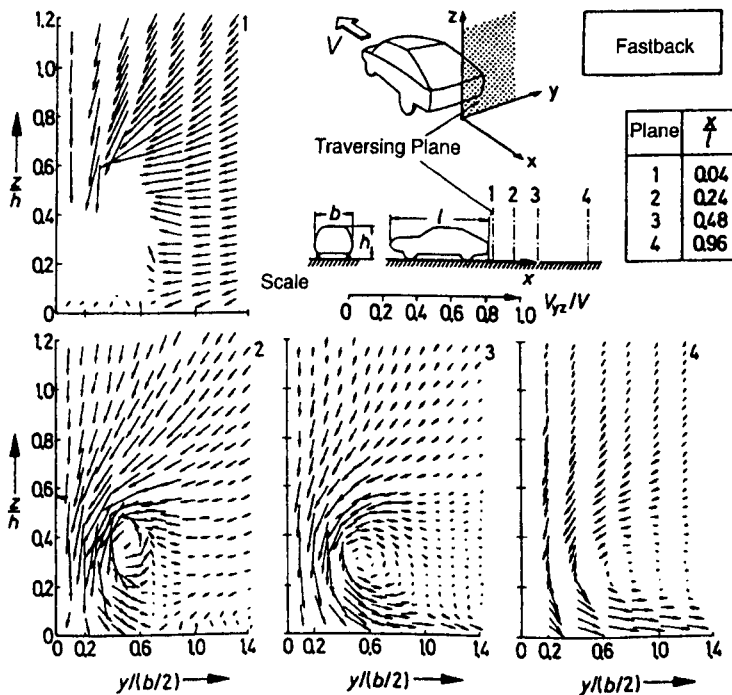
Figure 6.25 Cross-flow velocity field in wake of fastback model, Ahmed [1].

The characteristics of the turbulent wake behind a 20° slant angle in steady flow is reported by Bearman and Mullarkey [8] who measured the lateral and vertical velocity components using a single hot-wire probe at $x/\ell = 0.34$ downstream of the model base and at the mid-model height. The turbulence intensities recorded at the centre and side of the model were 2% and 13% respectively. Sims-Williams and Dominy [66] measured pressure fluctuations in the wake behind the Ahmed model and showed variation of between 10% and 20% of the freestream dynamic pressure, and suggested that this is partly due to the strong vorticity in the wake which can locally amplify unsteadiness.

Similar effects were found by Davis [18] in a study of the changes in wake structure associated with different rear slant angles. Wake surveys were conducted at $x/\ell = 0.40$ downstream of the model leading edge and showed that the magnitude of lateral velocities is influenced by the rear slant angle this produces different level of turbulent intensities behind the model.

With this evidence from the literature the used of band-limited white noise to simulate the unsteadiness can be associated with turbulence intensities behind the model. This phenomenon is clearly a subject of interest for future research.

6.7 Conclusion

1. The side force and yaw moment magnification determined from the transient experiment is greater than unity across the reduced frequency ranges measured.

2. The yaw damping derivative was found to be a function of Reynolds number; at low velocities it is negative but progressively increases to positive values. With further increases in speed; a self-sustained oscillation is observed. The self-sustained oscillation suggests the existence of external effects such as wake buffeting, asymmetric vortex formation or vortex shedding or combinations of both. Unsteadiness in amplitude during the self-sustained oscillation occurs when the system has very low damping.

3. The simulation shows that the self-sustained oscillation occurs when the aerodynamic damping cancels the mechanical damping. A simulation based on the linearised transient aerodynamic stiffness and damping results matched the experimental self-sustained oscillation frequency but failed to simulate the fluctuation in amplitude.

4. Calculation of the energy ratio is shown to provide a good quantitative assessment of the unsteadiness exhibited by the model. And the results appear to agree well with published results on wake turbulence.

5. Unsteadiness was introduced into the simulation though the addition of band-limited white noise. The intensity of the added noise is shown to correspond with the expected turbulence intensities in the wake.

Chapter 7

Results and Discussion – Parametric Studies

7.1 Introduction

In this chapter the techniques developed in Chapter 6 are applied in a parametric study of the effect of rear slant angle and C-pillar strake height. A reduced version of the results can be found in Passmore and Mansor [55]. The parametric study provides an opportunity to assess both the practical application of the technique as well as providing a specific crosswind stability study.

7.2 Parametric Investigation of Rear Slant Angle

7.2.1 Description of Model Geometry

The Davis model with various rear slant angles is shown in Figure 7.1. It comprises of a common fore-body with rear slant angles ranging between zero to 40°. In the subsequent analysis these angles are identified by the title SLxx, where xx refers to the rear slant angle. The detailed description of the model has been given in Section 3.4.
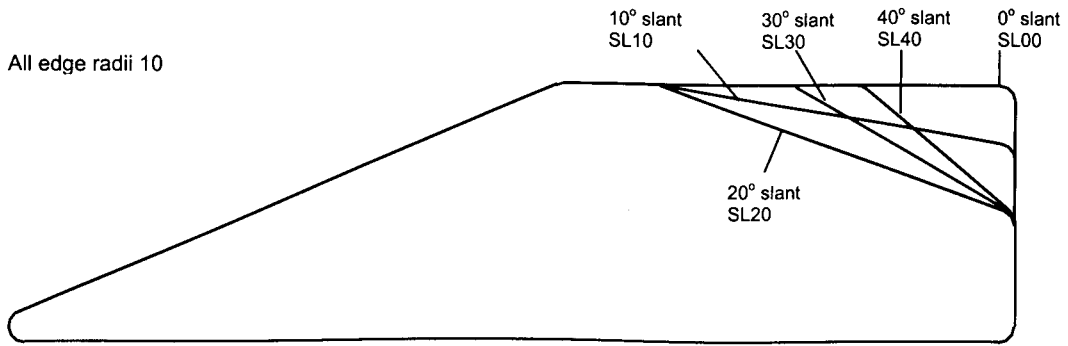
Figure 7.1 Davis model with zero degree (SL00), 10° (SL10), 20° (SL20), 30° (SL30) , 40° (SL40) rear slant angles.

7.2.2 Example of Data

Example time responses, measured at 10, 20, 30 and 40 m/s using single spring (K05) are shown in Figure 7.2, 7.3, 7.4 and 7.5 respectively. At 10 m/s the effect of aerodynamic damping is seen clearly in the data for zero degree, 10°, 20° and 40° slant angles. The 30° slant also has a damped response but the damping is clearly very weak.
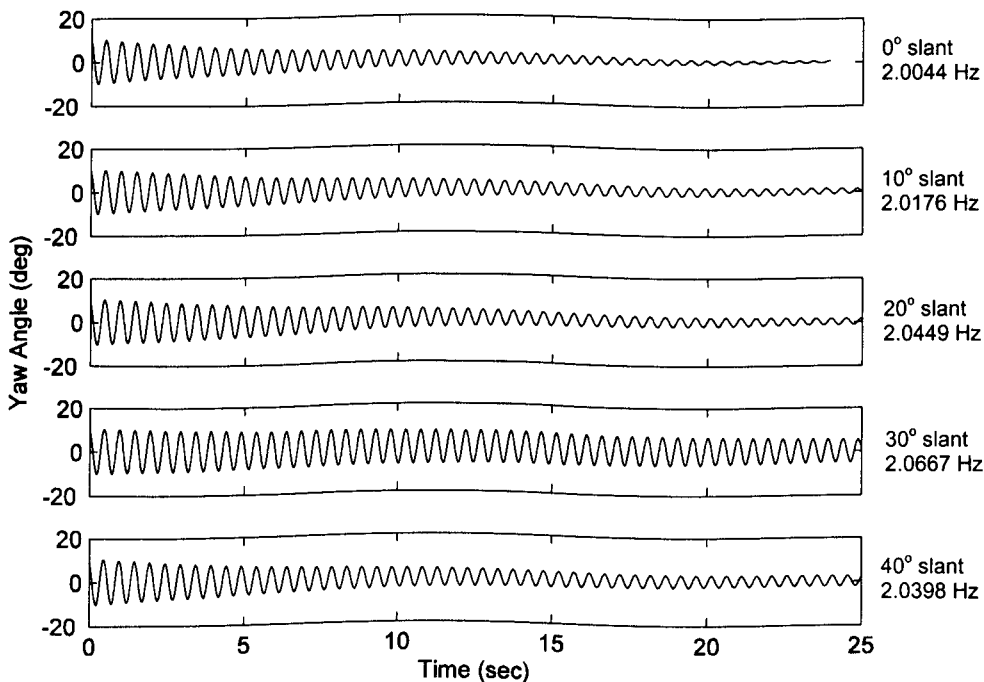
Figure7.2 Time response of different rear slant angles using single spring (K05) at 10 m/s.

As the speed increases to 20 m/s (refer to Figure 7.3) the effect of damping is still clear for 10° slant, and weak damping is seen for the 20° slant. The effect of self-sustained oscillation is clearly seen for zero degree, 30° and 40° slant angles.
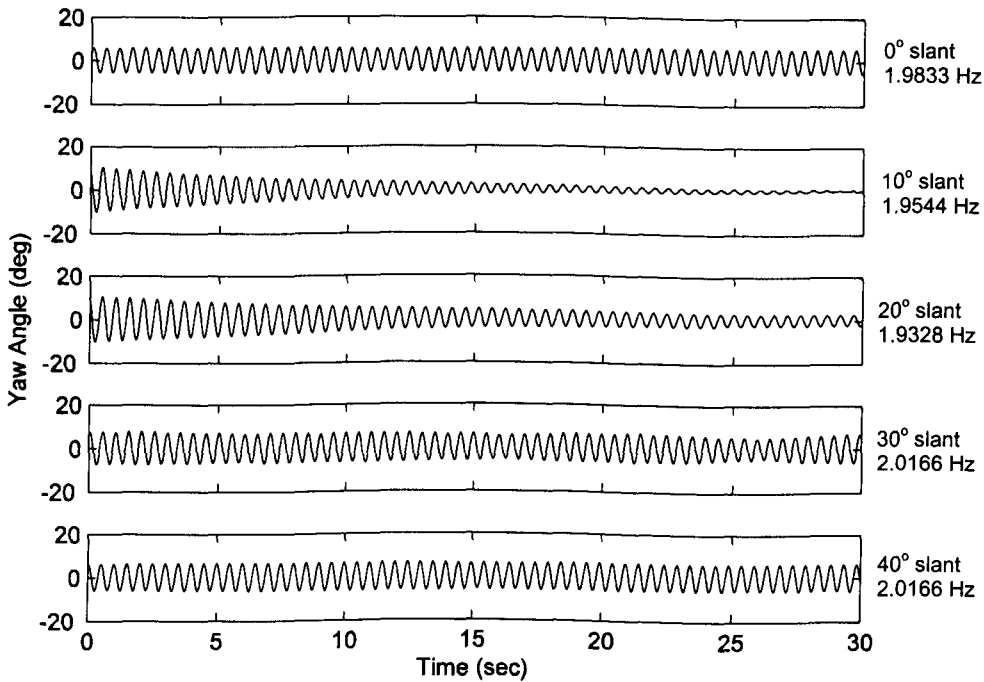
Figure 7.3 Time response of different rear slant angles using single spring (K05) at 20 m/s.
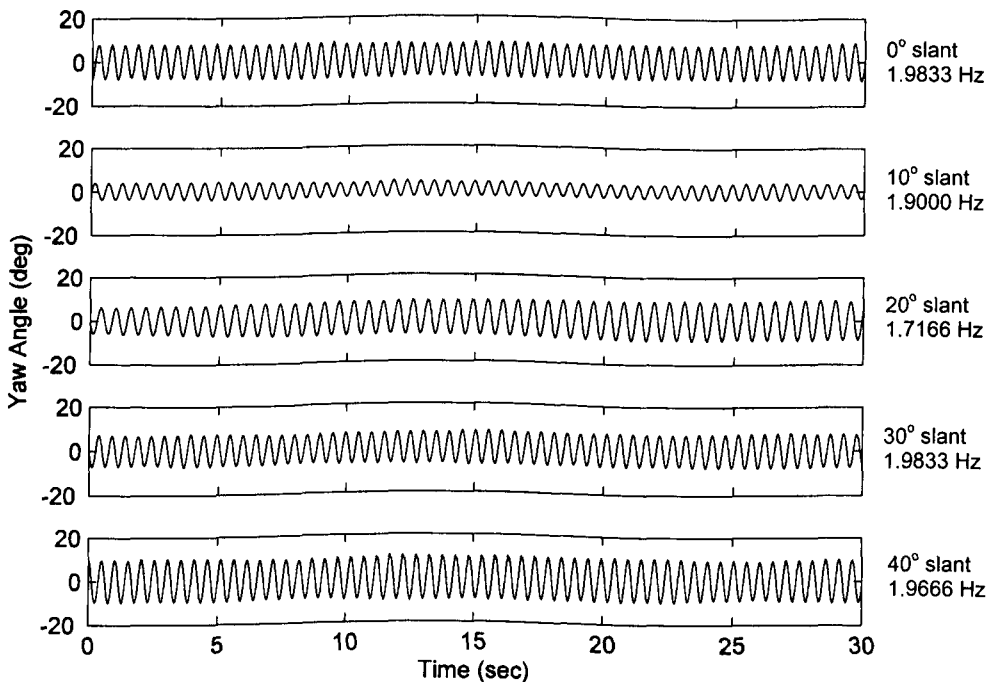
Figure 7.4 Time response of different rear slant angles using single spring (K05) at 30 m/s.

All models exhibit self-sustained oscillations at 30 m/s (refer Figure 7.4). The 20° and 40° slant have relatively large amplitudes of oscillation while 10° slant has the smallest amplitude.
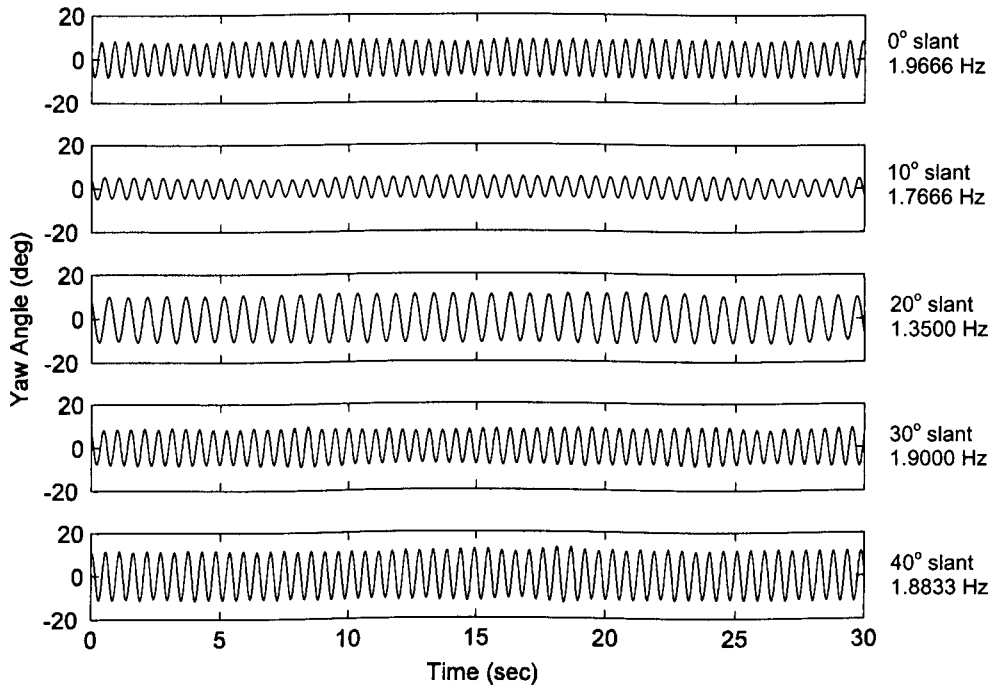
Figure 7.5 Time response of different rear slant angles using single spring (K05) at 40 m/s.

The models continue to exhibit self-sustained oscillations at 40 m/s (refer Figure 7.5) which has a very similar trend to 30 m/s but with slightly larger amplitudes.

For all models the damping effect is found to weaken as wind speed increases. This effect was seen for the 20° slant in Chapter 6 where the effect of Reynolds number on damping was explored. This dependency of Reynolds number is apparent have for all geometries.

Figure 7.6 shows the frequency ratio as a function of reduced frequency for different rear slant angles. The differences in frequency ratio between the slant angles are clearly separated at low reduced frequency. The frequency ratios for all models are tending to unity at high reduced frequency.
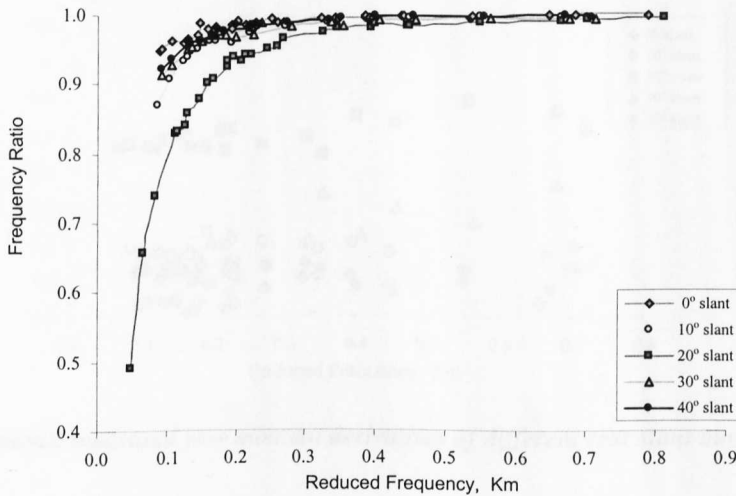
Figure 7.6 Frequency ratio against reduced frequency of different rear slant angles.

The effect of rear slant angle on frequency ratio provides an initial indication of the sensitivity of the model to crosswind or gust effects. The model which shows the greatest effect with reduced frequency is likely to be the most sensitive. This result agrees well with literature Ahmed [1], Hucho [30], Howell [32] which report that the square-back shape of the estate car is less susceptibility to transient crosswind compared to a hatch-back.

7.2.3 Dynamic Yaw moment and Side Force Derivatives

The yaw moment and side force derivatives from the dynamic tests are shown in Figure 7.7 and 7.8.

In Figure 7.7, for all slant angles the yaw moment derivatives show some variation across the reduced frequency range though it is always less for reduced frequencies below 0.2. The 30° slant shows significant variation and this is also the case for the static yaw moment derivative with Reynolds number in Figure 4.6 in Section 4.3.1. The 30° slant is known to exhibit a critical process of switching between high drag and low drag flow associated with the appearance and disappearance of a strong wake, Ahmed et al. [2]. For reduced frequencies less than 0.2 the 20° slant has the highest yaw moment derivative with values between 0.45 and 0.5. The zero degree slant exhibits the least value generally less then 0.05.
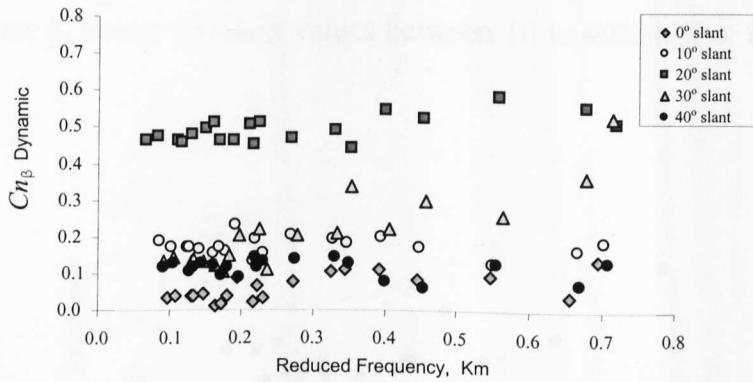
Figure 7.7 Dynamic measured yaw moment derivatives of different rear slant angles.

The side force derivative in Figure 7.8 shows wider variation than the yaw moment derivative though again there is less variation for reduced frequencies less than 0.2. For higher reduced frequencies the 20° and 30° slants exhibit large variation.
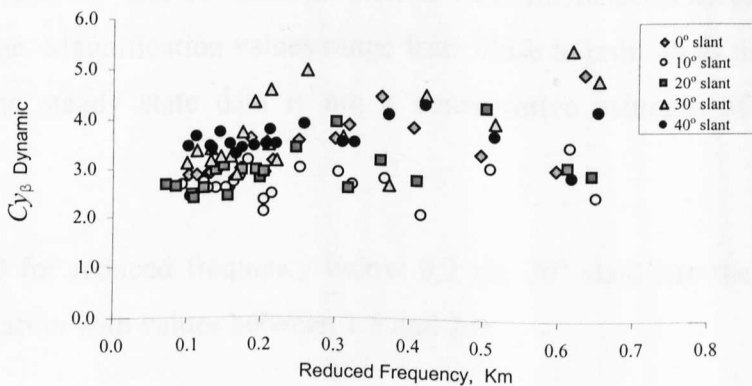
Figure 7.8 Dynamic measured side force derivatives of different rear slant angles.

7.2.4 Magnification of Yaw Moment and Side Force Derivatives

The results from the dynamic tests and their magnifications are shown in Figure 7.9 and 7.10. In each case the dynamic derivatives have been divided by the appropriate static derivative from Figure 4.7 and Figure 4.8 in Chapter 4 to generate a magnification factor.

In Figure 7.9 the yaw moment magnification is close to unity for the 10° slant angle throughout the reduced frequency range, suggesting that the steady state

measurements are a good estimate of the transient loads. The 20° slant, reported in detail in Chapter 6, shows transient values between 10 to 40% higher than the static values.
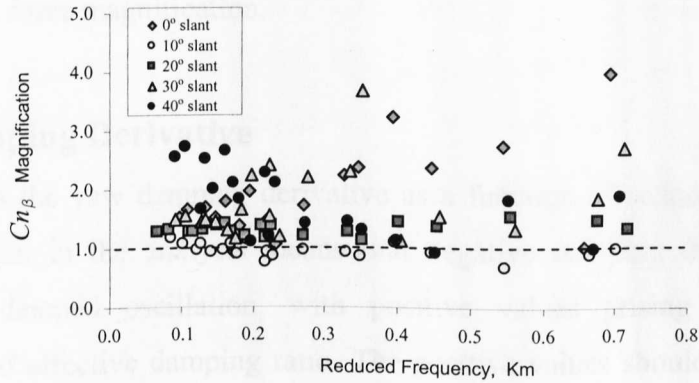
**Figure 7.9 Yaw moment magnification against reduced frequency for different rear slant angles.**

However the zero, 30° and 40° slant all exhibit wide fluctuations across the reduced frequency range. Magnification values range from close to unity to as much as 4.0. In these cases the steady state data is not a conservative estimate of the dynamic situation.

In Figure 7.10 for reduced frequency below 0.2 the 20° slant has the greatest side force magnification with values between 1.5 and 2.0.
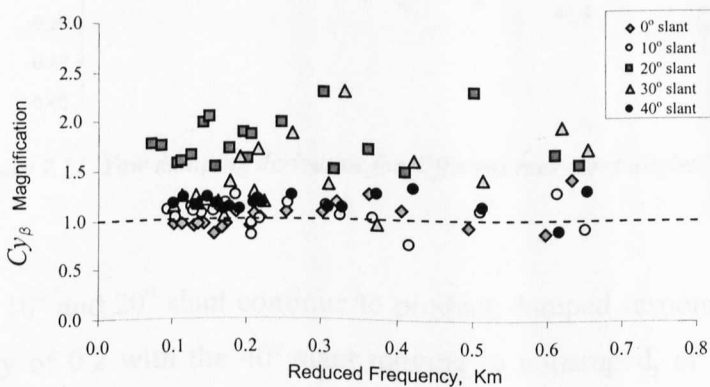
**Figure 7.10 Side force magnification against reduced frequency for different rear slant angles.**

The zero degree slant has values generally close to unity and the remainder all show values slightly greater than one. At higher reduced frequencies the 10° and 40° slant

continue to show responses close to unity but both the 20° and 30° slants show large variation, with magnification values ranging from unity to over 2.0.

It should be noted that configurations with low yaw moment magnification may not also have low side force magnification.

7.2.5 Yaw Damping Derivative

Figure 7.11 shows the yaw damping derivative as a function of reduced frequency. The approach taken in the analysis means that negative damping derivatives are associated with damped oscillation, with positive values arising through the assumption of zero effective damping ratio. The positive values should therefore be treated with caution as they are not an accurate representation of the aerodynamic effect, but they do serve to indicate transition into self-sustained oscillation. A much better description of the aerodynamic effect is provided by the energy ratio discussed in Section 6.5.2. This method will be applied to this data in a later section. The figure shows that all models exhibit a damped response at the highest reduced frequency.
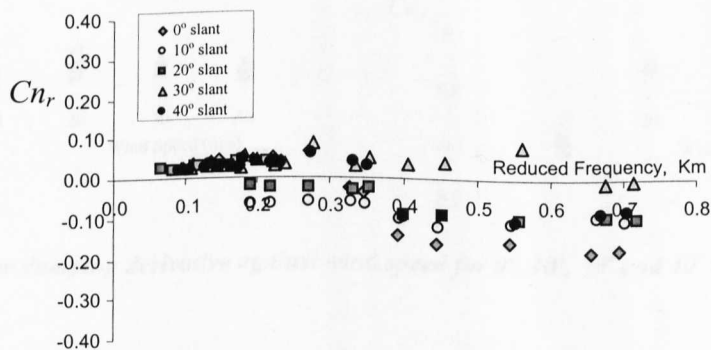
Figure 7.11 Yaw damping derivative for different rear slant angles.

The zero degree, 10° and 20° slant continue to produce damped responses down to a reduced frequency of 0.2 with the 40° slant moving to undamped, or self-sustained oscillation at a reduced frequency of 0.35. However the 30° slant produces a self-sustained oscillation at reduced frequencies of approximately 0.65.

It is well known that the 30° slant angle represents a critical angle for transition between a strong three-dimensional flow structures to a less structured turbulent

wake. The positive damping values seen for the 30° slant are thought to reflect the strong likelihood of regular coupled vortex shedding. It would appear that the critical nature associated with the 30° slant angle ensures that this shedding occurs across most of the frequency ranges explored. This would suggest that the nature of the test helps maintain the strong 3D structure with regular shedding. This tends to agree with Passmore et al. [54] when he found that in the transient case the pressure measurements indicate that the C-pillar vortex is intensified. Below a reduced frequency of about 0.2 all the models show positive damping derivatives, hence self-sustained oscillation. The last configuration to move into this mode is the 10° slant. The conclusion that has been made from Figure 7.11 which relates the level of damping with self-sustained oscillation is strongly supported by Figure 7.12.
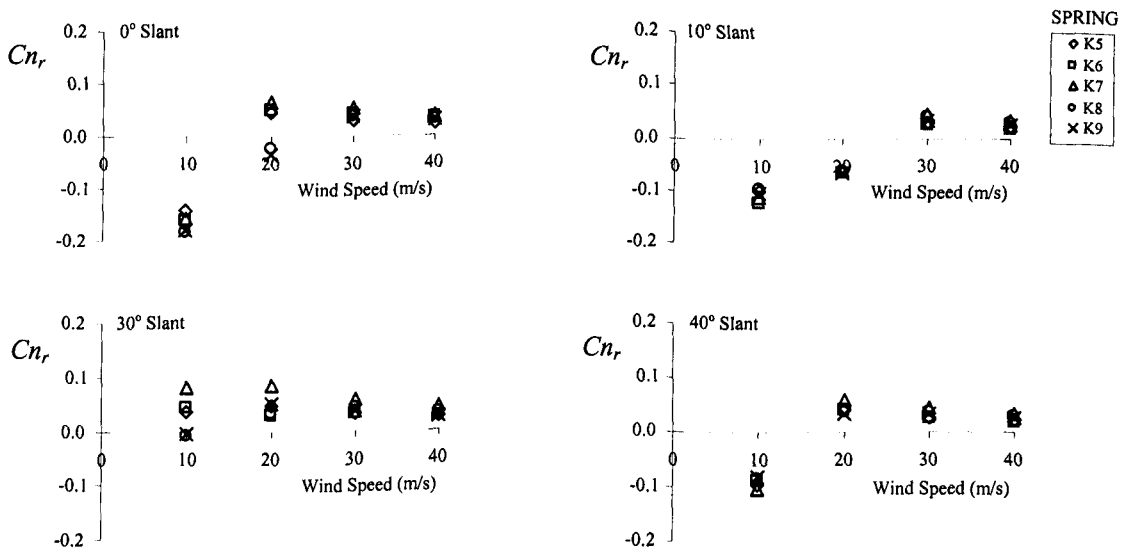
Figure 7.12 Yaw damping derivative against wind speed for 0°, 10°, 30° and 40° rear slant angles.

This figure shows the cross over for each configuration and indicates that the cross over speed for 30° slant is less than 10 m/s when compared to zero degree, 10° and 40°, for which the cross-over speeds are around 20 m/s.

7.2.6 Energy Ratio

Figure 7.13 shows the total energy of a self-sustained oscillation for different slant angles using a single spring at 40 m/s for two minutes. Although the plots are not in the form of energy ratio, 40° slant shows significantly larger energy compared to the others. It is clear that in the figure the 40° slant has the greatest mean energy and

highest levels of unsteadiness, while the $10°$ exhibits the least. High levels of unsteadiness are also demonstrated by the $20°$ but appear to take a different form to the $40°$ slant.
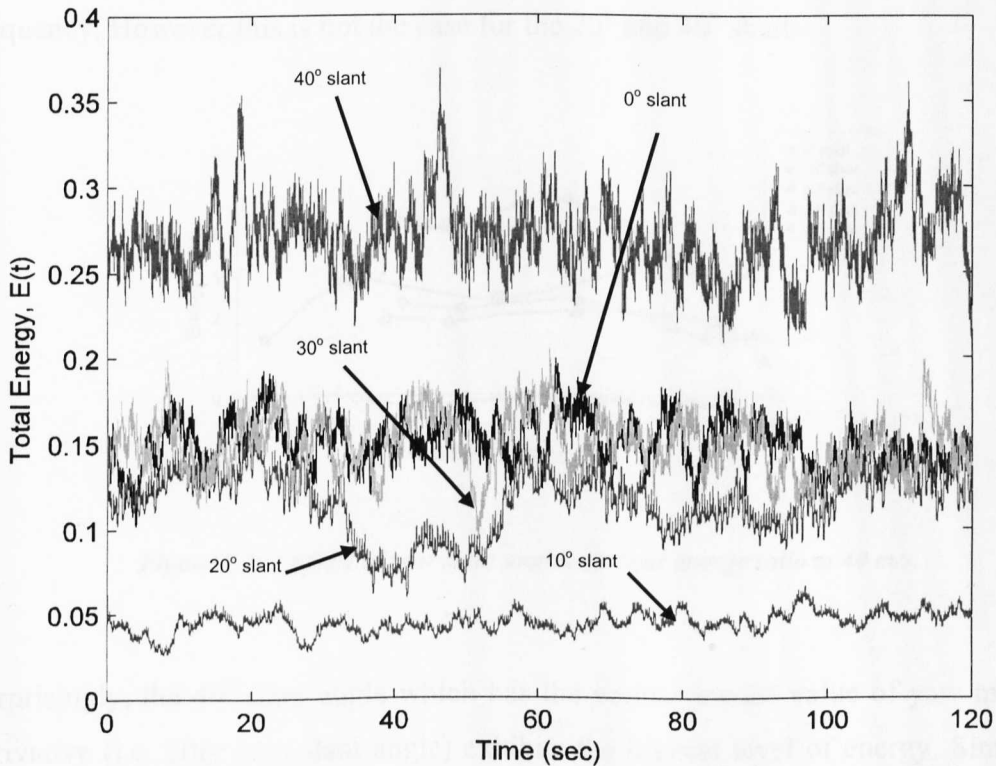
Figure 7.13 Effect of rear slant angles on total energy, E(t) (K05 at 40 m/s).

Results in Table 7.1 and Figure 7.14 show the calculated energy ratios for all models at 40 m/s.

Spring	$0°$ slant	$10°$ slant	$20°$ slant	$30°$ slant	$40°$ slant
			$\dfrac{E(t)_{on} - E(t)_{off}}{E(t)_{off}}$		
K05	2.3110	-0.0896	1.3762	1.9466	4.5536
K06	2.1407	-0.2552	2.8262	1.8679	4.1577
K07	2.3449	-0.0584	2.4099	2.1119	4.8338
K08	1.4116	-0.2584	3.2850	1.8281	2.9414
K09	1.5196	-0.1935	3.6801	0.8837	3.2838

Table 7.1 Energy ratio of different rear slant angles at 40 m/s.

It is clear that the 40° slant has the greatest energy ratio and highest levels of unsteadiness, while 10° exhibits the least. The 20° slant shows an increase in energy level as the oscillation frequency increases. Zero degree and 30° slant seem to have similar energy levels. For some slant angles the energy ratio is independent of reduced frequency. However this is not the case for the 20° and 40° slants.
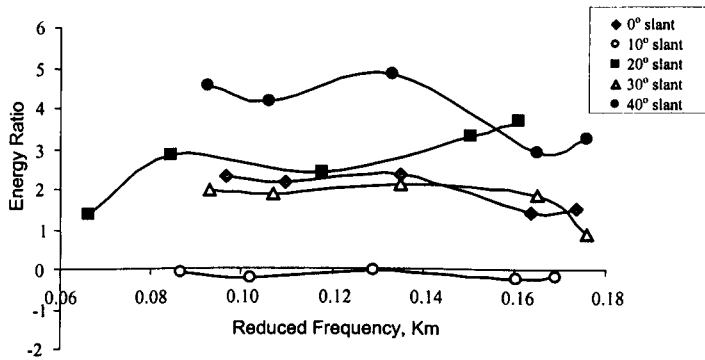
Figure 7.14   Effect of rear slant angles on total energy ratio at 40 m/s.

Surprisingly, the 40° slant angle which has the second lowest value of yaw moment derivative (i.e. after zero slant angle) exhibits the highest level of energy. Similarly, the 20° slant which has the highest yawing moment derivative shows about the same energy level with zero and 30° slant. On the other hand, the 10° slant angle which has the lowest yaw moment magnification shows an energy level less than zero. From these results, it could suggest that the level of the energy ratio is correlated with the aerodynamic magnification factor. The level of energy ratio for different slant angles in Figure 7.14 is consistent with the ranking of yaw moment magnification shows in Figure 7.9 for reduced frequencies less than 0.2, in the case when the model exhibits self-sustained oscillation at 40 m/s.

Figure 7.15 shows the relationship between the magnification of yaw moment derivative with energy ratio for reduced frequencies less than 0.2. The linear fit of the plot shows a gradient of 0.28 and passes through a magnification of one at zero energy ratio.
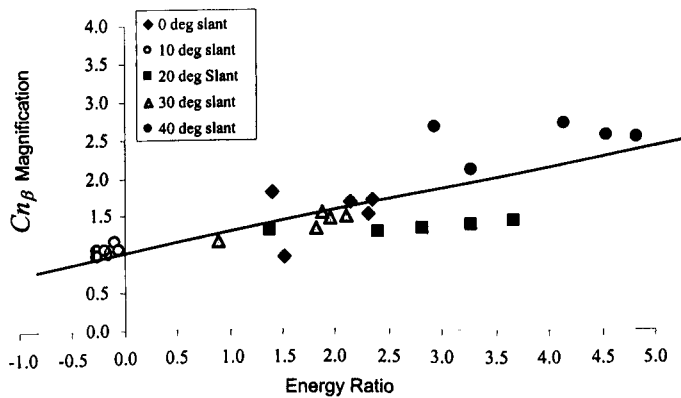
Figure 7.15   Relationship between yaw moment derivative magnification against energy ratio for reduced frequencies less than 0.2 (40 m/s).

The result in Figure 7.15 in particular interesting one because it shows a relationship between the linearised performance of the models and the non-linear 'unsteady' energy.

7.3 Effect of C-pillar Strakes

In addition to the parametric slant angle study the 20° Davis model was used to investigate the stabilizing effect of C-pillar strakes. This provides an opportunity to consider the overall suitability of the oscillating model technique in the assessment of simple vehicle modifications.

Here, five configurations are considered, the base model which has a 20° slant as presented in Chapter 6 (SL20), the base model with the 10 mm C-pillar curvature radius replaced with a sharp edge (ST00), and three strake heights of 2.5% (ST04), 5.0% (ST08) and 10% (ST16). Strake height has been non-dimensionalised using the overall body height. The strakes are attached along the longitudinal edges of the C-pillar, fitted flush with the side of the model. As an example the model fitted with the 5% strake is shown in Figure 7.16.
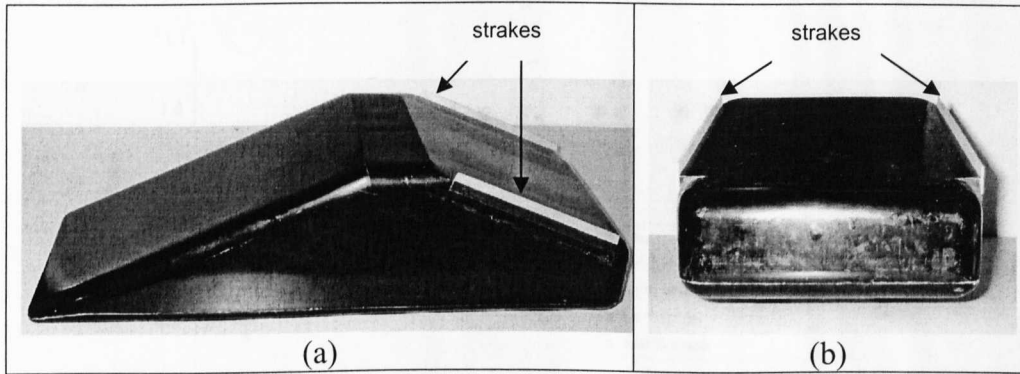
Figure 7.16 Model installed with 8 mm strake (5% to model height). (a) side view, (b) rear view.

7.3.1 Example of Data

Figure 7.17 and 7.18 show the time response and frequency ratio for the five configurations using spring K5 at 30 m/s.
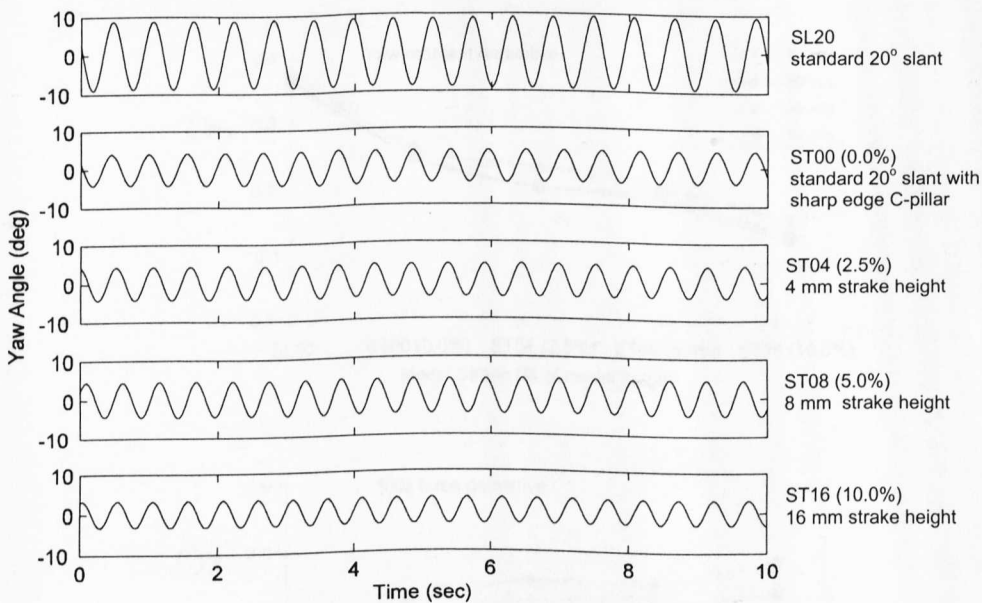
Figure 7.17 Time response for different height of C-pillar strakes using single spring (K5 at 30m/s).

Removing the C-pillar curvature approximately halves the amplitude of the self-sustained oscillation. Adding and then increasing the strake height appears to have little effect initially on the amplitude but the effect of increasing height is seen in the frequency ratio. When increasing strake height from 5 to 10% a further significant reduction in oscillation amplitude occurs. The frequency ratio reduces progressively with increasing strake size.
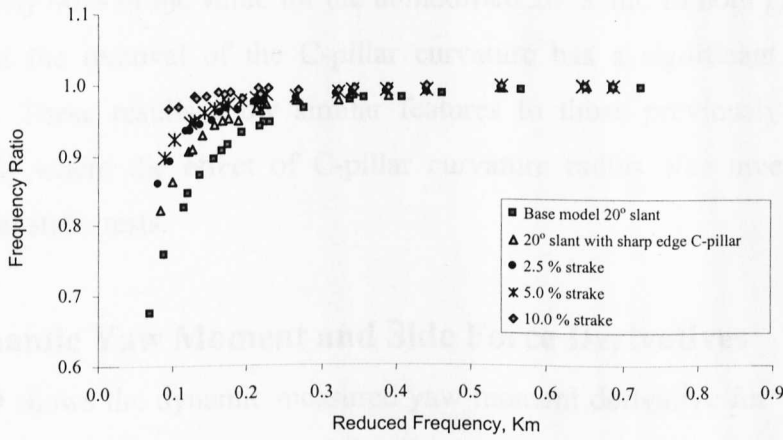
Figure 7.18 Frequency ratio against reduced frequency for different height of C-pillar strakes.

7.3.2 Static Yaw Moment and Side Force Derivatives

Figure 7.19 shows the static derivative for varying the height of the C-pillar strake.
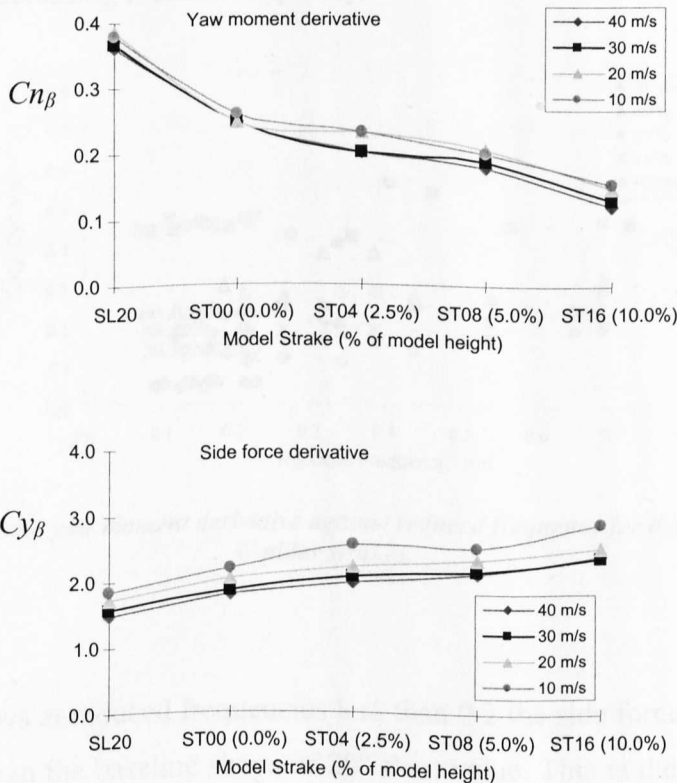
Figure 7.19 The effect of C-pillar strakes on static yaw moment and side force derivatives.

The side force derivative increases progressively with increasing strake size, up by approximately 50% with the largest installed. The yaw moment derivative reduces over the same range. With the largest strake installed, the yaw moment is

approximately 40% of the value for the unmodified 20° slant. In both graphs it is also evident that the removal of the C-pillar curvature has a significant effect on the derivatives. These results show similar features to those previously identified by Howell [32] where the effect of C-pillar curvature radius was investigated using conventional static tests.

7.3.3 Dynamic Yaw Moment and Side Force Derivatives

Figure 7.20 shows the dynamic measured yaw moment derivative for varying height of the C-pillar strake. Removal of C-pillar curvature results in a halving of the derivative over most of the reduced frequency range, although it is noted that at some frequencies the reduction is much less. The yaw moment derivative reduces progressively with increasing strake size down by approximately 80% with the highest strake height. With 2.5, 5 and 10% strakes the yaw moment derivative increases with increasing reduced frequency.
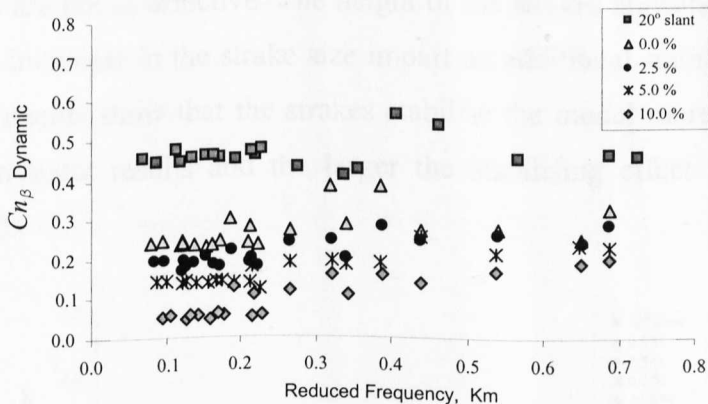
Figure 7.20 Dynamic yaw moment derivative against reduced frequency for different height of C-pillar strakes.

Figure 7.21 shows at reduced frequencies less than 0.2 the side force derivative for all strakes is less than the baseline shape of 20° slant value. This is the opposite trend to the results from the static tests in Figure 7.19. However the trend of increasing side force with increasing strake size found in static measured is maintained at reduced frequency less than 0.2. For higher reduced frequencies the side force derivative for all strakes shows large variation.
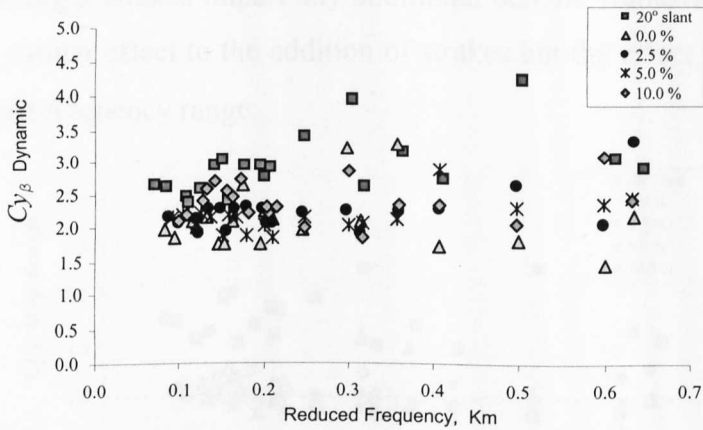
Figure 7.21 Dynamic side force derivative against reduced frequency for different height of C-pillar strakes.

7.3.4 Magnification of Yaw Moment and Side Force Derivatives

The yaw moment magnifications from the same tests are shown in Figure 7.22. Below a reduced frequency of 0.4 the magnification is generally below unity, however above 0.4 the strakes are not as effective. The height of the strakes appears to be important, as progressive increases in the strake size impart an additional stabilizing effect. The magnification results show that the strakes stabilise the model more in practice than predicted from static results and the larger the stabilising effect the more this is underestimated.
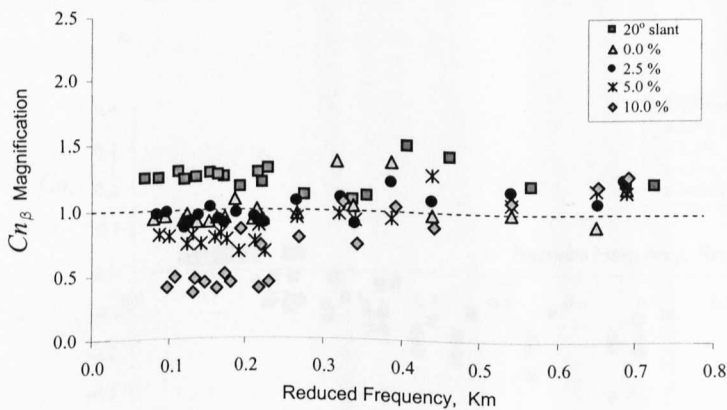
Figure 7.22 Yaw moment magnification against reduced frequency for different height of C-pillar strakes.

The side force magnifications calculated from the dynamic tests are shown in Figure 7.23. The effects of the strakes are clear as the magnification is either close to or below unity in all cases. However, there does not appear to be any clear trend to

indicate that the larger strakes impart any additional benefit. Removal of the C-pillar curvature has a similar effect to the addition of strakes but the effect is not consistent across the reduced frequency range.
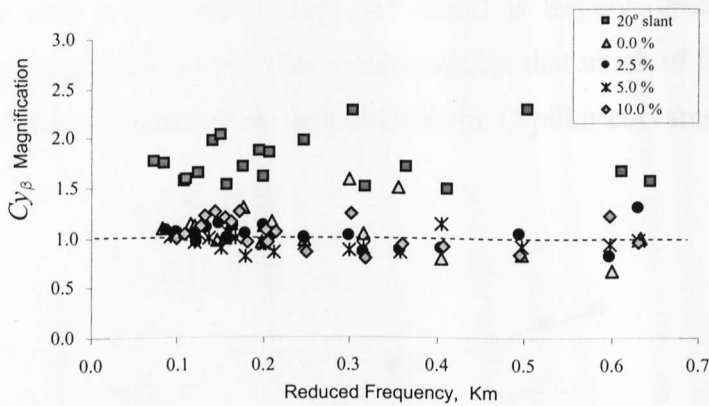
Figure 7.23 Side force magnification against reduced frequency for different height of C-pillar strakes.

7.3.5 Yaw Damping Derivative

The effect of the strakes on the yaw damping derivative (Figure 7.24) is generally to make the motion more damped. However the cross over point remains at a reduced frequency of approximately 0.2 irrespective of strake size. In practice this means that the model motion becomes self-sustained at the same tunnel speed, but the amplitude of sustained oscillation is greatly reduced.
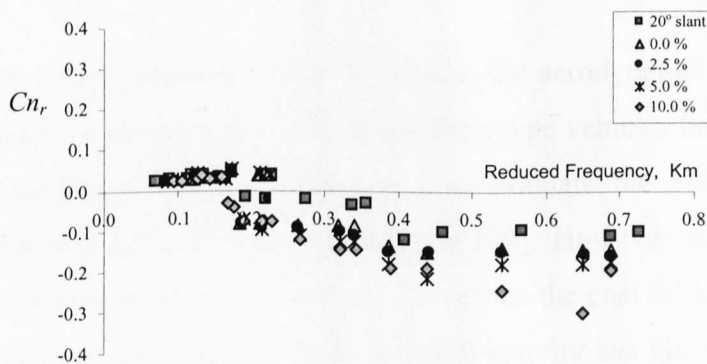
Figure 7.24 Yaw damping against reduced frequency for different height of C-pillar strakes.

7.3.6 Energy Ratio

The energy ratio is shown in Figure 7.25 and illustrates the strong influence of the strakes on unsteadiness. However, the height of the strakes is again not significant as the unsteadiness seen in the base model (20° slant) is largely removed simply by introducing sharp edges to C-pillar. This would suggest that much of the unsteadiness that exists can be linked to uncertain separation on the C-pillar curvature.
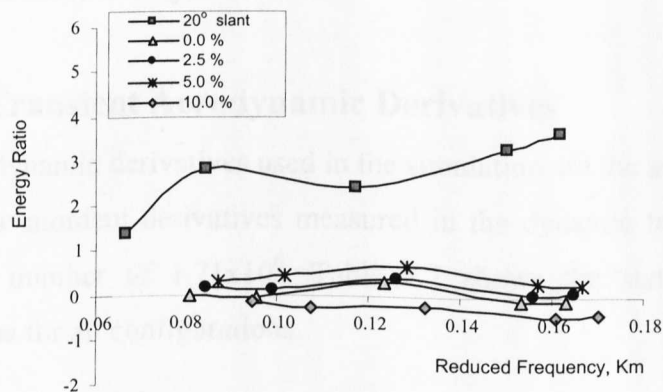
Figure 7.25   Effect of C-pillar strake heights on total energy ratio at 40 m/s.

7.4 Simulation of Vehicle Crosswind Sensitivity

The purpose of this section is to conduct a dynamic simulation based on a simple lateral equation of a vehicle model. It is important to know the effect of the aerodynamic forces and moments on driving stability because it is responsible for the excitation and influences the response of the vehicle.

In a real case, for a non-steady motion of a vehicle, the aerodynamic loads influence its overall stiffness and damping characteristics. Prototype vehicles have been used to check vehicle stability by actual driving tests to evaluate the effect of transient aerodynamics, Murgai [50], Hiramatsu and Soma [29]. However at this stage it is often too late to make changes to the vehicle. To reduce the cost of developing a new vehicle and allow early intervention, much research activity has involved developing handling and stability simulations to study the effect of aerodynamics during the design phase, Yip and Crolla [75], Kee et al. [36], Mac Adam [43]. The aerodynamic models used in such simulations are determined from steady-state wind tunnel tests performed on the vehicle, or on a scale model.

In this work, a mathematical model of vehicle lateral motion is developed using a simple model. The intention here is to compare the effect of rear slant angles and C-pillar strakes responses to crosswind and to rank the crosswind sensitivity ratings, however, it is not a primary part of the project. For the purpose of comparison, the tyre cornering stiffness and weight distribution are kept constant for all aerodynamic configurations. The aerodynamic loads are defined as the function of the aerodynamic derivatives from the static and dynamic tests.

7.4.1 Average Transient Aerodynamic Derivatives

The transient aerodynamic derivatives used in the simulation are the average values of side force and yaw moment derivatives measured in the dynamic tests taken at the highest Reynolds number of 1.71×10^6. Table 7.2 shows the static and average dynamic derivatives for all configurations.

Configurations	Static Derivatives		Dynamic Derivatives	
	$Cy_{\beta_{static}}$ (rad^{-1})	$Cn_{\beta_{static}}$ (rad^{-1})	$Cy_{\beta_{dynamic}}$ (rad^{-1})	$Cn_{\beta_{dynamic}}$ (rad^{-1})
Rear Slant Angles				
0° slant (SL00)	3.0309	0.0229	2.8056	0.0284
10° slant (SL10)	2.4064	0.1604	2.5833	0.1712
20° slant (SL20)	1.4954	0.3610	2.7205	0.4815
30° slant (SL30)	2.7273	0.0917	3.1252	0.1278
40° slant (SL40)	2.9794	0.0458	3.4253	0.1149
C-Pillar Strake Heights				
0.0 % (ST00)	1.7787	0.2464	1.8554	0.2387
2.5 % (ST04)	1.9804	0.2005	2.0658	0.1912
5.0 % (ST08)	2.1201	0.1776	2.1225	0.1419
10.0 % (ST16)	2.3799	0.1203	2.3705	0.0546

Table 7.2 Static and average dynamic measured side force, yaw moment at Reynolds number 1.71×10^6 for different rear slant angles and C-pillar strake heights.

7.4.2 Simulation Results

The simulation permits the estimation of important parameters such as yaw angle, yaw rate, path deviation and lateral acceleration. The derivation of transfer functions to determine the yaw angle and yaw rate response to a wind gust are given in Appendix C. The transient parameter of path deviation and yaw rate are compared with different model configurations similar to previous Section.

The vehicle baseline data is based on typical value for passenger cars Zhenggi et al. [78]. For the purpose of comparison all models are assumed to have the same chassis parameters as listed in Table 7.3. For all models the aerodynamic side force and yaw moment derivatives are referenced to mid wheel-base, as measured in the wind tunnel.

Vehicle weight,	$W = 1200$ kg
Wheel base	$\ell wb = 2.5$ m
Distance between front axle and cg	$\ell f = 1.25$ m
Distance between rear axle and cg	$\ell r = 1.25$ m
Yaw inertia	$I_{zz} = 1600$ kg m^2
Front wheel cornering stiffness	$Krf = -32000$ N/rad
Rear wheel cornering stiffness	$Krr = -41500$ N/rad
Chassis Derivatives:	
Side force stiffness	$Y_{\beta c} = Krf + Krr = -73{,}500$ N/rad
Side force damping	$Y_{rc} = (lfKrf - lrKrr)/u = -430$ Ns/rad
Yaw stiffness	$N_{\beta c} = (lfKrf - lrKrr) = 12051$ Nm/rad
Yaw damping	$N_{rc} = (lf^2 Krf + lr^2 Krr)/u = -4224$ Nms/rad

Table 7.3 Vehicle data for simulation [78].

The vehicle is simulated at 28 m/s forward speed and exposed to a crosswind at the speed of 16 m/s normal to vehicle speed for 1.5 seconds, Goetz [25], Kee et al. [36], Hiramatsu and Soma [29]. The plot of crosswind exposure is shown in Figure 7.26. The simulation results are shown in Figure 7.27 for different rear slant angles and in Figure 7.28 for different height of C-pillar strakes.
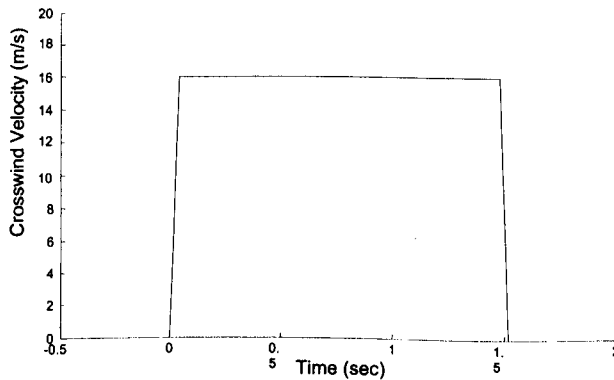
Figure 7.26 Crosswind input exposure.

Figure 7.27 shows the effect of rear slant angles on vehicle response. The 20° slant shows a rapid increase in yaw rate compared to the other models, while zero degree slant shows the least. For all models the maximum value of yaw rate progressively increases with the increase in yaw moment derivative. The maximum value of yaw rate for 20° slant is more than double the maximum values shown by zero 30° and 40° slant angles. It is clearly demonstrated that the increment of yaw rate and the time to reach its maximum value is strongly influenced by the yaw moment derivatives.

For lateral acceleration the 40° slant shows a rapid increase and has the highest value compared to the others, while the 10° slant shows the least. The response and peak value of lateral acceleration coincides with the path deviation. The figure shows that the path deviation, lateral acceleration are strongly influenced by the side force derivatives.

Figure 7.28 shows the effect of C-pillar strakes on vehicle response. All response parameters show a reduction with increasing height of C-pillar strake. The most significant effect is seen in the yaw rate response, which is reduced by half with a 20° slant when the C-pillar curvature is removed and progressively reduces further with increasing strake height. Path deviation shows 25% reduction with a sharp C-pillar, 2.5% and 5% strake heights. Similar effect is seen on yaw angle and lateral acceleration. However when the 10% strake height is installed the path deviation increases and is close to the baseline due to the large increase in side force derivative.
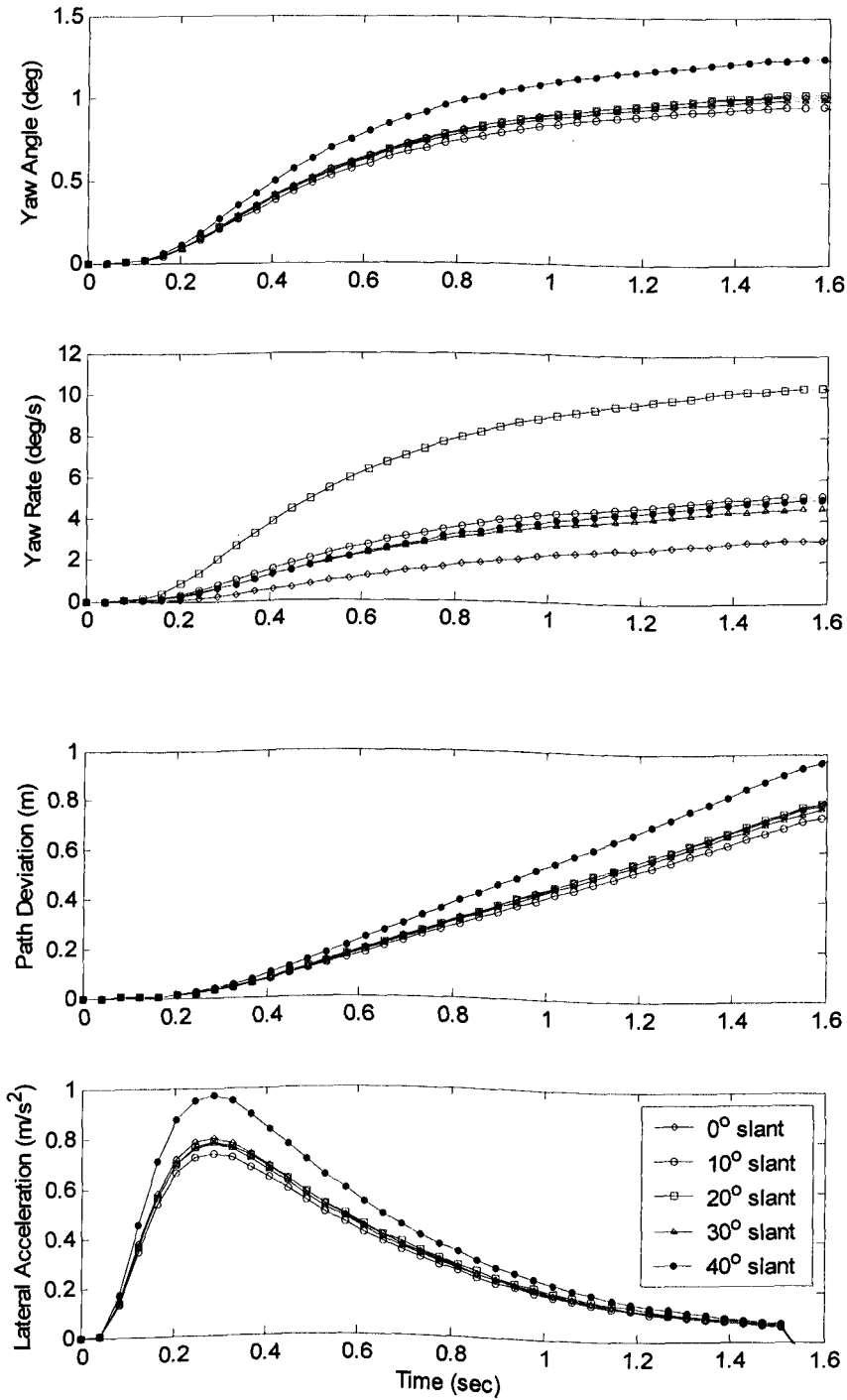
Figure 7.27 Open loop yaw angle, yaw rate, path deviation and lateral acceleration of different rear slant angles.
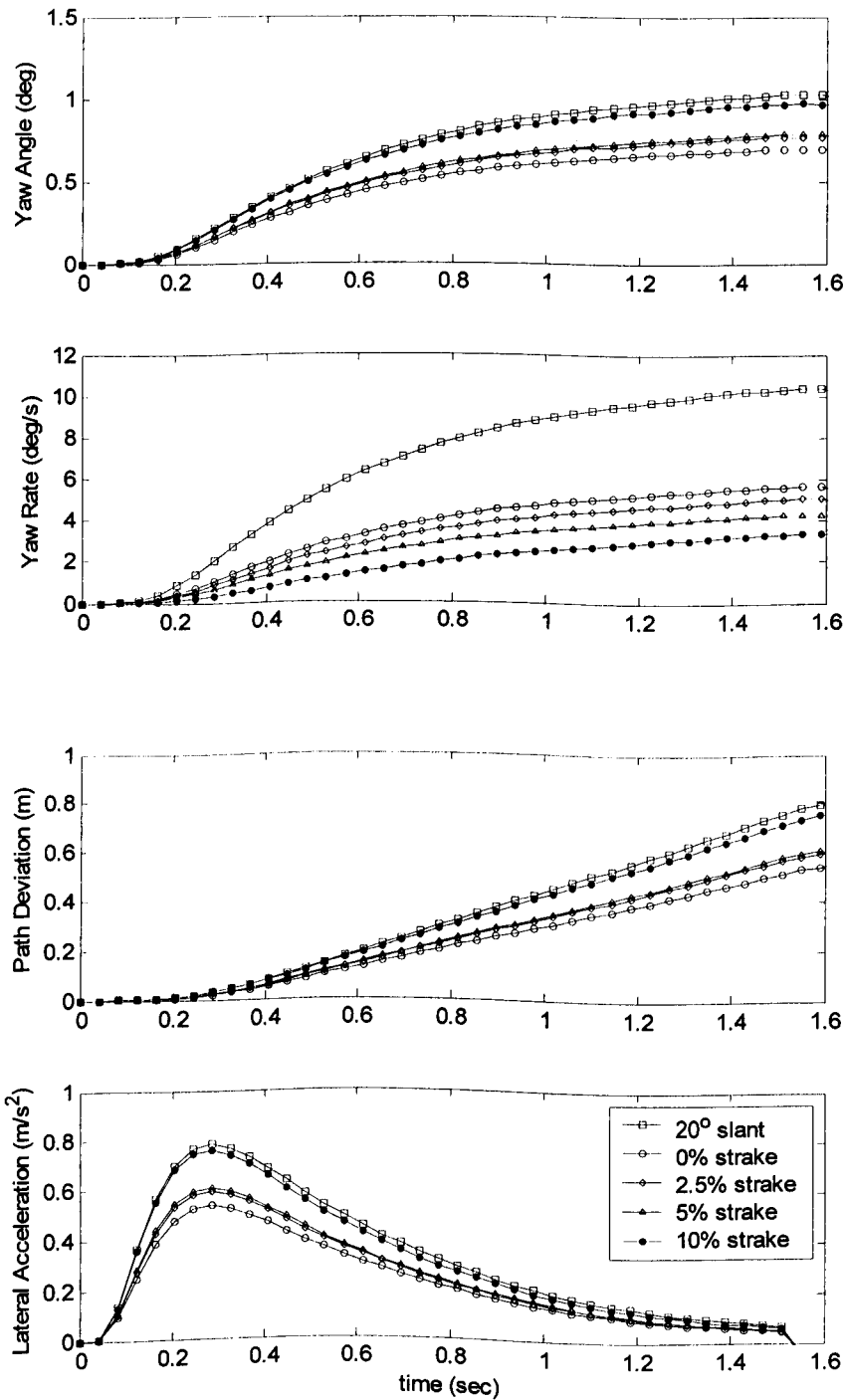
Figure 7.28 Open loop yaw angle, yaw rate, path deviation and yaw acceleration of different height of C-pillar strakes.

This could suggest that for larger strake size the vehicle has less effect on rotational acceleration but has a greater effect on path deviation under a strong crosswind gust.

It has been predicted that the damping derivatives could influenced the vehicle response to crosswind. However, in all cases, the inclusion of the aerodynamic damping derivatives Cy_r and Cn_r in the simulation has no effect on yaw rate and path deviation. It is concluded that the aerodynamic damping is very small compared to the mechanical damping from the vehicle chassis and therefore does not affect the yaw rate and path deviation.

7.4.3 Crosswind Sensitivity Rating

In the evaluation of vehicle response to crosswind the important parameters are the path deviation and yaw rate, Howell [32], [33], Murgai [50], Hiramatsu and Soma [29], Milliken [46]. Volkswagen [25] developed a rating method in an effort to provide summary information from measured responses for vehicles tested using their crosswind facility. The method relies only on the yaw rate response and is given as S_A:

$$S_A = r_{max} * t_{(r_{max})} * r_{(t=1s)} \qquad (7.1)$$

where, r_{max} = maximum yaw rate

$t_{(r_{max})}$ = time of maximum yaw rate

$r_{(t=1s)}$ = yaw rate after 1 sec

The formula can be modified to change the dimension of S_A in deg^2/s to deg.

$$S_B = \sqrt{r_{max} * t_{(r_{max})} * r_{(t=1s)}} * 1s \qquad (7.2)$$

In the test reported the rating parameter is shown to correlate well with subjective assessments of the same vehicles. A higher sensitivity factor indicates that the car is sensitive to crosswind. The results of the crosswind sensitivity rating for various slant angles using the static and average value of the dynamic derivatives from the simulation are tabulated in Table 7.4 and Table 7.5 respectively, while Table 7.6 shows results for various strake heights.

	0° slant SL00	10° slant SL10	20° slant SL20	30° slant SL30	40° slant SL40
Maximum yaw rate (deg/sec)	3.19	4.86	7.39	2.91	3.51
Time at maximum yaw rate (sec)	1.63	1.59	1.55	1.59	1.63
Yaw rate after 1 sec (deg/sec)	2.31	3.98	6.46	2.37	2.62
S_B (deg)	3.47	5.55	8.60	3.32	3.87

Table 7.4 Open Loop Crosswind sensitivity ratings based on static measured derivatives of different slant angles.

	0° slant SL00	10° slant SL10	20° slant SL20	30° slant SL30	40° slant SL40
Maximum yaw rate (deg/sec)	3.07	5.19	10.39	4.60	5.01
Time at maximum yaw rate (sec)	1.63	1.59	1.55	1.59	1.59
Yaw rate after 1 sec (deg/sec)	2.25	4.25	8.99	3.69	3.93
S_B (deg)	3.36	5.93	12.04	5.19	5.59

Table 7.5 Open Loop Crosswind sensitivity ratings based on dynamic measured derivatives of different slant angles.

	0.0 % ST00	2.5 % ST04	5.0 % ST08	10.0 % ST16	20° slant SL20
Maximum yaw rate (deg/sec)	5.65	5.05	4.29	3.35	10.39
Time at maximum yaw rate (sec)	1.55	1.59	1.59	1.63	1.55
Yaw rate after 1 sec (deg/sec)	4.81	4.23	3.52	2.54	8.99
S_B (deg)	6.49	5.83	4.91	3.73	12.04

Table 7.6 Open loop crosswind sensitivity ratings based on dynamic measured derivatives of different height of C-pillar strakes.

By comparison between the static (Table 7.4) and dynamic (Table 7.5) crosswind sensitivity ratings the 30° slant shows the highest increases in crosswind sensitivity rating of 56% followed by 40° (44%), 20° (40%), and 10° (7%) slant angle, while 0° slant shows reduction of 3%.

For all configurations the ratings of the crosswind sensitivity show that yaw moment derivative strongly influences the crosswind sensitivity factor. A 20° slant demonstrates the highest rating of crosswind sensitivity, while zero degree slant exhibits the least. However, removing the C-pillar curvature of the 20° slant reduced the crosswind sensitivity by 45%.

7.5 Conclusion

- In the study of the effect of rear slant angle the results demonstrate that quasi-steady responses are often a poor predictor of the true unsteady performance and they are rarely a conservative estimate.

- The transient derivatives and aerodynamic magnifications are both influenced by the model configuration (i.e. rear slant angle and C-pillar strake). The derivatives show the actual sensitivity of the model and the aerodynamic magnifications shows whether the static test is conservative.

- At low reduced frequency (i.e. less than 0.2) the aerodynamic magnification correlates with the energy ratio. 40° slant has the highest level of energy ratio and therefore the highest levels aerodynamic magnification, while 10° slant exhibits the least.

- The aerodynamic damping seems to dampen the fluctuation in amplitude oscillation during self-sustained oscillation. 10° slant which has the strongest effect in aerodynamic damping demonstrates magnification close to unity and negative energy ratio.

- The unsteadiness in self-sustained oscillations is strongly dependent on rear slant angle. Strakes on the C-pillar are shown to stabilise the flow and reduce the derivative magnification significantly. This would suggest that the level of unsteadiness can be linked to uncertain separation on the C-pillar curvature.

- In the simple vehicle simulation the crosswind sensitivity is determined from yaw rate response. The model with large value of positive yaw moment derivative Cn_β generates high yaw rate thus exhibits higher degree of crosswind sensitivity. The side force derivative Cy_β has strong effects on path deviation. Strakes on C-pillar are shown to reduce crosswind sensitivity. However bigger strake size shows increasing in side force derivative creates larger path deviation in a strong crosswind.

Chapter 8

Conclusions and Recommendations

8.1 Conclusion

Based on extensive experimental results, this thesis attempts to (1) introduce the transient simulation of vehicle unsteady aerodynamic in the wind tunnel using oscillating model rig, and (2) to develop the mathematical model and simulation to analyse the experimental results. A series of experiments have been conducted to measure the steady and dynamic (transient) side force and yaw moment response of a simplified car-type bluff body. In the dynamic tests the input was generated using an oscillating model rig, and the model response determined using angular displacement measurements. Transient data acquired over a range of non-dimensional frequencies were analysed to determine side force and yaw moment aerodynamic magnification factors

Combination of the experimental results and applying assumptions, theory and numerical simulation has allowed an in-depth analysis of the transient cases and the effects of rear slant angle and C-pilllar strakes.

8.1.1 Summary of Experimental Method

A series of experiment have been conducted to measure the steady and transient yawed conditions of a simplified car-type bluff body. The measurements were made over a range of free stream velocities from 10 to 40 m/s, equating to a Reynolds number range from 0.43×10^6 to 1.71×10^6, and a range of reduced frequency from 0.05 to 0.81.

The frequency of oscillation, (synonymous with the frequency of disturbing wind input) was modified by altering the mechanical stiffness of the facility. Analysis of the wind-off and wind-on response allowed the transient aerodynamic loads to be estimated. The aerodynamic magnification factor was determined from the ratio between the dynamic (transient) and the static derivatives.

The effects of wind speed (i.e. Reynolds number) and oscillation frequency were considered and the models exhibited damped and undamped behaviour. The yaw moment derivative was estimated from the frequency ratio determined in each case from the power spectral density. However, the estimation of the yaw damping derivative was only suitable for damped oscillation. For undamped behaviour the energy ratio was employed to quantify the unsteady behaviour of the self-sustained oscillation.

The accuracy (precision) of the estimation is dependent on the repeatability of the measurement of damped frequency and time to half amplitude. The uncertainty of the yaw moment and yaw damping derivatives depends on the model configuration and tunnel free-stream velocity. In the experiment, the mechanical damping is very small, this improves the precision of the oscillating rig in estimating the derivatives.

8.1.2 Simulation Model

A linearised quasi-steady model was developed to analyse the experimental results. The derivation of the linear model was based on the assumption that the aerodynamic loads were acting as stiffness and damping to the model motion and presented as aerodynamic derivatives. The quasi-steady analysis predicted the primary frequency very well but not the self-sustained oscillation and the fluctuation in amplitudes.

Using the same simulation it was shown that the self-sustained oscillation occurs when the aerodynamic damping cancelled out the mechanical damping. Unsteadiness in the oscillation amplitude was reproduced in the simulation by introducing a band-limited white noise. The simulation results were compared using the *power spectral density*, *probability density function* and *phase-plane* plots. It was shown that the intensity of the band-limited white noise is related to the intensity of turbulence within the model wake.

8.1.3 Comparison of Transient and Steady State Measurements

8.1.3.1 Effect of Rear Slant Angles

- In the study of the effect of rear slant angle the results demonstrated that quasi-steady responses are often not a conservative predictor of the true unsteady performance. For all but the 10° rear slant angle the results showed that the transient side force and yaw moment exceeded the predicted steady state data.

- The intensity of the unsteadiness seen in self-sustained oscillations is strongly dependent on rear slant angles. The model with the highest damping (10° slant) exhibited the lowest level of uncertainties. The 40° slant has the greatest energy and therefore the highest levels of unsteadiness.

- The yaw damping derivative was also dependent on the Reynolds number. At low Reynolds number negative damping gave stability to the model, but as the Reynolds number increases, the damping became positive causing the model to exhibit self-sustained oscillation. The positive damping values were thought to reflect the strong likelihood of regular coupled vortex shedding. The self-sustained oscillation would suggest that external effects such as the turbulent wake or asymmetric vortex formation may have excited the model.

8.1.3.2 Effect of C-Pillar Strakes

- The addition of C-pillar strakes is shown to stabilise the flow, with even small height strakes yielding responses well below that of steady state. The removal of C-pillar curvature significantly reduced the yaw moment derivatives and led to a magnification close to one.

- The height of the strakes appeared to be significant in yaw moment data, as progressive increases in the strakes size imparted an additional stabilising effect.

- The effect of strakes on the yaw damping derivative is generally to make the motion more damped. However, they do not alter the speed at which self-sustained motion occurs.

8.2 Crosswind Sensitivity

The effect of the aerodynamic derivatives on a hypothetical vehicle is tested using a simple crosswind simulation. It was shown that the crosswind sensitivity rating is greatly influenced by the magnitude of the aerodynamic yaw moment derivatives rather than by the side force derivative. The zero degree slant (squareback) demonstrates the least susceptibility to crosswind. The high aerodynamic magnification and energy ratio shown by 40° slant shows that it has a significant effect on the lateral acceleration and path deviation parameters. Strakes on the C-pillar are shown to stabilise the flow and lessen the crosswind sensitivity rating.

8.3 Suggestions for Further work

The oscillating model facility proved its worth and ability to produce good and reliable measurements to be applied for the study of unsteady transient aerodynamics. The wind tunnel test programmes supported with the simulation results demonstrated the effectiveness of one degree-of-freedom pure yawing motion in estimating aerodynamic derivatives in transient case. It is hope that this study will stimulate further investigation in the future.

In order to improve the technique, suggestions for further work can be carried out as the following:

- Install additional sensors such as an accelerometer and internal balance inside the oscillating model. This provides direct measurement of transient side force, yaw moment and yaw acceleration for comparison and investigation of the existence of other unsteady modes.

- Investigation of unsteady wake behind the model with flow survey apparatus such as constant temperature anemometer (CTA) or particle image velocimetry (PIV). These results could be useful to correlate the unsteadiness with the energy ratio and turbulent wake properties.

- To include a forced oscillation test in which the input parameters can be controlled with a wider range of frequencies and amplitudes. The comparison between input and output parameters could provide extra information of the transient aerodynamic characteristics such as gain and phase margin. To implement that the existing oscillating rig can be connected to an actuator via the cross-arm in order to oscillate the model, the existing spring arrangements would be retained.

- The relationship between aerodynamic magnification, energy ratio and wake turbulent require further investigation.

References

[1]   Ahmed S R, *"An Experimental Study of the Wake Structures of Typical Automobile Shapes"*, Journal of Wind Engineering and Industrial Aerodynamics, Vol: 9 (1981)

[2]   Ahmed S R, Ramm G, Faltin G, *"Some Salient Features of the Time-Averaged Ground Vehicle Wake"*, SAE 840300, The Engineering Resource for Advancing Mobility, 1984.

[3]   Baker C J, Humphreys N D, *"Assessment of the Adequacy of Various Wind Tunnel Techniques to Obtain Aerodynamic Data for Ground Vehicles in Cross winds"*, Journal of Wind Engineering and Industrial Aerodynamics 60 (1996) 49-68, Elsevier Science, 1996.

[4]   Barnard R H, *"Road Vehicle Aerodynamics Design"*, Addison Wesley Longman, 1996.

[5]   Barlow J B, Rae Jr. R H, Pope A, *"Low-speed Wind Tunnel Testing"*, 3rd Edition John-Wiley & Sons, 1999.

[6]   Beam B H, *"A Wind-Tunnel Test Technique for Measuring the Dynamic Rotary Stability Derivatives at Subsonic and SuperSonic Speed*, Report 1258, NACA 1955.

[7]   Bearman P W, *"Some Observations on Road Vehicles Wakes"*, SAE 840301, Automobile Aerodynamics; Wake, Wind Effects, Vehicle Development, SP-569, 1984.

[8]   Bearman P W, Mullarkey S P, *"Aerodynamic Forces on road Vehicles due to Steady Side Winds and Gusts"*, RAeS Vehicle Aerodynamic Conference, Loughborough, 1994.

[9]   Bearman P W, *"Near Wake flows Behind Two and Three Dimensional Bluff Body"*, Journal of Wind Engineering and Industrial Aerodynamics 69-71 (1997).

[10] Bird J D, Fisher L R, Hubbard S M, *"Some Effect of Frequency on the Contribution of a Vertical Tail to the Free Aerodynamic Damping of a Model Oscillating in Yaw"*, NACA Report 1130, 1952.

[11] Blevin R D, *"Flow-Induced Vibration"*, Van Nostrand Reinhold, 2nd Edition, New York, 1990.

[12] Cartmell M, *"Introduction to Linear, Parametric and Nonlinear Vibrations"*, Chapman and Hall, 1st Edition, London, 1990.

[13] Chadwick A, Garry K P, Howell J P, *"Transient Aerodynamic Characteristics of Simple Vehicle Shapes by the Measurement of Surface Pressure"*, Vehicle Aerodynamics SAE SP-1524, 2000-01-0876, 2000.

[14] Chometon F et al., *"Experimental Study of Unsteady Wakes Behind an Oscillating Car Model"*, SAE 2005-01-0604. SAE International, Warrendale, 2005.

[15] Cooper K R, *"Bluff-Body Aerodynamics as Applied to Vehicles"*, Journal of Wind Engineering and Industrial Aerodynamics, Vol:49, 1993.

[16] Cooper K R, *"Closed-Test-Section Wind Tunnel Blockage Corrections for Road Vehicles"*, SAE SP-1176, 1996.

[17] Darling J, Standen P M, *"A Study of Caravan Unsteady Aerodynamic"*, D11702, IMechE 2003.

[18] Davis J P, *"Wind Tunnel Investigation of Road Vehicle Wakes"*, PhD Thesis, Imperial College of Science and Technology, University of London, October 1982.

[19] Deniz S, Staubli T H, *"Oscillating Rectangular and Octagonal Profile: Interaction of Leading and Trailing Edge Vortex Formation"*, Journal of Fluids and Structures, 11, pg(3-31), 1997.

[20] Facchinetti M, De Langre E, Biolley F, *"Coupling of Structure and Wake Oscillators in Vortex-induced Vibration"*, Journal of Fluids and Structures, 2003.

[21] Fillipone A, *"Advanced Topics in Aerodynamics –Unsteady Aerodynamics "*, Web site http://aerodyn.org/Unsteady/Unsteady.html, 1999-2003.

[22] Fillipone A, *"Unsteady Gust Response of Road Vehicles"*, ASME Vol.125, September 2003.

[23] Fisher L R, *"Experimental Determination of Effects of Frequency and Amplitude on the Lateral Stability Derivatives for a Delta, a Swept, and Unswept Wing Oscillating in Yaw*, NACA Report 1357, 1956.

[24] Garry K P, Cooper K R, *"Comparison of Quasi-Static and Dynamic Wind Tunnel Measurements of Simplified Tractor-Trailer Models"*, Journal of Wind Engineering and Industrial Aerodynamics, No. 22, 1986.

[25] Goetz H, *"Crosswind Facilities and Procedures"*, SAE SP-1109, Warendale 1995.

[26] Hales F D, *"Stability Problems of Road Vehicle"*, 1st Symposium on Road Vehicle Aerodynamic, The City University, London, Nov 1969.

[27] Hemon P, Santi F, *"On the Elastic Behaviour of Rectangular Cylinder in Cross-flow"*, Journal of Fluids & Structures, pg 855-889, 2002.

[28] Hemon P, Noger C, *"Transient Growth of Energy and Aeroelastic Stability of Ground Vehicle"*, Journal C. R Mecanique 332 (2004) pg 175-180, Elsevier 2004.

[29] Hiramatsu K, Soma H, *"Response Parameters for Characterizing Vehicle Behaviour Under Lateral Wind Disturbance"*, C466/009/93, IMechE, 1993.

[30] Hucho W H, *"Aerodynamics of Road Vehicle"*, SAE International, Warrendale, 4th Edition, 1998.

[31] Hucho, W H, Emmelmann, H J, *"Theoretical Prediction of the Aerodynamic Derivatives of a Vehicle in Cross Wind Gusts"*, SAE Paper 730232,1973.

[32] Howell J P, *"Shape Features which Influence Crosswind Sensitivity"*, C466/036/93, IMechE 1993.

[33] Howell J P, *"The Side Load Distribution on a Rover 800 Saloon Car Under Crosswind Conditions"*, Journal of Wind Engineering and Industrial Aerodynamics, 60 (1996) 139-153.

[34] Jakobsen J B, Hjorth-Hansen E, *"Determination of the Aerodynamic Derivatives by a System Identification Method "*, Journal of Wind Engineering and Industrial Aerodynamics, 57 (1995) 295-305.

[35] Kareem A, Gurley K, *"Damping in Structures: Its Evaluation and Treatment of Uncertainty"*, Journal of Wind Engineering and Industrial Aerodynamics, 59 (1996) 131-157, 1996.

[36] Kee J D, Kim M S, Lee J H, *"The aerodynamic Effect on High Speed Stability and Crosswind Stability"*, Hyundai Motor Company, Korea, 2003.

[37] Khalighi B et al., *"Experimental and Computation Study of Unsteady Wake Flow Behind a Bluff Body with a Drag Reduction Device"*, SAE 2001-01B-207, 2001.

[38] Kobayashi N, Minoru Y, *"Stability of a One Box Type Vehicle in a Cross-Wind – An Analysis of Transient Aerodynamic Forces and Moments"*, SAE 881878, 1988.

[39] Krajnovic N, Davidson L, *"Development of Large-Eddy Simulation for Vehicle Aerodynamics"*, IMECE2002-32833, ASME International Congress, 2002.

[40] Lienhard J H, *"Synopsis of Lift, Drag and Vortex Frequency Data for Rigid Circular Cylinder"*, Washington State University, College of Engineering, Research Division Bulletin 300, 1966.

[41] Lock A, *"Using CFD and Wind Tunnels to Predict High-speed and Crosswind Stability "*, Web site http://mira.atalink.co.uk/articles/137.html, Jan.2005.

[42] Macklin A R, Garry K P, Howell J P, *"Comparing Static and Dynamic Testing Techniques for the Crosswind Sensitivity of Road Vehicles"*, SAE 960674, 1996.

[43] Mac Adam C C, *"The Interaction of Aerodynamic Properties and Steering System Characteristics on Passenger Car Handling"*, The Dynamics of Vehicle on Road and Tracks (Vehicle System Dynamics-Vol. 18), 11th IAVSD Symposium, 1989.

[44] Mansor S, Passmore M A, *"Estimation of Bluff Body Transient Aerodynamics Using an Oscillating Model Rig"*, International Colloquium on Bluff Body Aerodynamics and Applications – BBAAV, Ottawa, Canada, July 2004.

[45] Matsuno T, Yokouchi S, Nakamura Y, *"The Effect of Leading-Edge Profile on Self-Induced Oscillation of 45-Degree Delta Wing"*, AIAA-2000-4004.

[46] Milliken W F, Milliken D L, *"Race Car Vehicle Dynamics"*, SAE International, Warrendale, 1995.

[47] Morgenthal G, McRobie F A *"A Comparison Study of Numerical Methods for Fluids-Structure interaction Analysis in Long-Span Bridge Design"*, University of Cambridge, 2001.

[48] Morris A S *"Measurement and Instrumentation Principles"*, Butterworth Heinemann, First Published, 2001.

[49] Mullarkey S P, *" Aerodynamic Stability of Road Vehicles in Side Winds and Gust"*, PhD Thesis, University of London, 1990.

[50] Murgai N, *"Effect of Cross Winds on Road and Rail Vehicles"*, Aerospace Engineering Mechanics, Iowa State University, Ames, 50011, IA, 2002.

[51] Murphy P C, Klein V, *"Estimation of Aircraft Unsteady Aerodynamic Parameters from Dynamic Wind Tunnel Testing"*, AIAA-2001-4016, 2001.

[52] Nelson R C, *"Flight Stability and Automatic Control"*, McGraw-Hill, 2nd Edition,1998.

[53] Newland D E, *"An Introduction to Random Vibration and Spectral Analysis"*, Longman, 2nd Edition, London, 1984.

[54] Passmore M A, Richardson S, Imam A, *"An Experimental Study of Unsteady Vehicle Aerodynamics"*, IMechE Part D Journal of Automotive Engineering, Volume 215 Number 7, July 2001.

[55] Passmore M A, Mansor S, *"The measurement of Transient Aerodynamics using an Oscillating Model Facility"*, SAE 2006 World Congress, April 2006, Detroit, USA.

[56] Roberts J B, Spanos P D, *"Random Vibration and Statistical Linearization"*, John Wiley & Son, England, 1990.

[57] Russell J B, *"Aerodynamic Effects on the Lateral Control and Stability of Motor Vehicles"*, 1st Symposium on Road Vehicle Aerodynamics, The City University, London, Nov 1969.

[58] Rüdinger F, *"Modelling of Estimation of Damping in Non-linear Random Vibration"*, PhD Thesis, Technical University of Denmark, October 2002.

[59] Ryan A, Dominy, R G, *"The Aerodynamic Forces Induced on Passenger Vehicle in Response to a Transient Cross-Wind Gust at a Relative Incidence of 30°"*, Developments in Vehicle Aerodynamics, SAE SP-1381, 980392, 1998.

[60] Ryan A, Dominy, R G, *"Wake Survey Behind a Passenger Car Subjected to a Transient Cross-wind Gust"*, Vehicle Aerodynamics, SAE SP-1524, 2000-01-0874, 2000.

[61] Scanlan R H, *"Some Observation on the State of Bluff-body Aeroelasticity"*, Journal of Wind Engineering and Industrial Aerodynamics Vol:69-71 (1997).

[62] Scibor-Rylski A J, *"Road Vehicle Aeodynamics"*, Pentech Press Limited, London, UK, 1975.

[63] Siegel S G, *"Experimental Investigation of the Wake Behind an Axisymmetric Bluff Body"*, Desertation, University of Arizona, 1999.

[64] Silva W A, Piatak D J, Scott R C, *"Identification of Experimantal Unsteady Aerodynamic Impulse Responses"*, AIAA, 2003-1959, 2003.

[65] Simiu E, Scanlan R H, *"Wind Effects on Structures"*, 3nd Edition, Wiley-Interscience, New York, 1996.

[66] Sims-Williams D B, Dominy, R G, *"Experimental Investigation into Unsteadiness and Instability in Passenger Car Aerodynamics"*, Developments in Vehicle Aerodynamics, SAE SP-1381, 980391, 1998.

[67] Sims-Williams D B, Dominy, R G, Howell J P *"An Investigation into Large Scale Unsteady Structures in the Wake of Real and Idealised Hatchback Car Models"*, SAE 20021-01-1041, 2001.

[68] Thompson S A., Batill S M, Nelson R C, *"Unsteady Surface Pressure Distribution on Delta Wing Undergoing Large Amplitude Pitching Motions"*, AIAA-90-0311, 1990.

[69] Tran V T, *"A calculation Methods for Estimating the Transient Wind Force and Moment Acting on a Vehicle"*, Vehicle Aerodynamic SAE SP-855, 1991.

[70] Tuovila W J, Robert W H, *"Aerodynamic Damping at Mach Number of 1.3 and 1.6 of a Control Surface on a Two-Dimensional Wing by the Free-Oscillation Method"*, NACA RM L56A26a, Washington, May 1956.

[71] Van Oudheusden B W, *"Aerodynamic Stiffness and Damping Effects in the Rotational Galloping of a Rectangular Cross-Section"*, Journal of Fluids and Structures, 14, 1119-1144, 2000.

[72] Watkins S, Toksoy S, Sounders J W, *"On the Generation of Tunnel Turbulence for Road Vehicles"*, 11th Australasian Fluid Mechanics Conference, University of Tasmania, Australia, 1992.

[73] Watkins S, Sounders J W, *"Turbulence Experienced by Road Vehicles under Normal Driving Conditions"*, SAE 950997.

[74] Yamada A, Ito S, *"Computational Analysis of Flow Around a Simplified Vehicle-Like Body"*, Vehicle Aerodynamic SAE 930293, PT-49, Warrendale, 1996.

[75] Yip C K, Crolla D A, Horton D N L, *"The Influence of Aerodynamic Effects on Car Handling"*, IMechE 925043, 1992.

[76] Zan S J, Richard G L, *"Unsteady Aerodynamic Loads on a Helicopter Fuselage In a Ship Airwake "*, American Helicopter 58th Annual Forum, Canada, 2002.

[77] Zhang, X, Brownjohn J M W, *"Time Domain Formulation of Self-Excited Forces on Bridge Deck for Wind Tunnel Experiment"*, Journal of Wind Engineering and Industrial Aerodynamics 91 (2003) 723-736, Elsevier Science Ltd. 2003.

[78] Zhenggi G, Fang G, Jun W, *"Investigation of the Transient State Steering Stability in Side Winds for High-Speed Vehicle"*, Int. Journal of Vehicle Design, Vol.26. No.5, 2001.

Appendix A

A.1 Commissioning of the Dynamic Test Facility

The main objective of this commissioning test was to integrate the whole system and evaluate the performance of the rig. These preliminary test results allow us to understand precisely the capability, limitation and behaviour of the facility. The tests include; determining a suitable range of wind speed, selection of spring stiffness, reduced frequency range, potentiometer calibration, model size and inertia. The quality of the signal from the recorded time response data is evaluated and improved on the basis of optimum sampling rate, data resolution and accuracy, and instrumentation signal to noise ratio. The results are based on a slant of 20° and circular disc as the test models.

A.1.1 Spring Data

Ten springs were used in this experiment. The springs were coded as K1 to K10. The linear stiffness and wind-off natural frequency of each spring are listed in Table A.1-1 All the springs were purchased from Lee Spring Limited, UK. The tolerance on spring stiffness and maximum load is ±10%. All springs have a nominal free length of 69.85 mm with tolerance on free length of ±1 mm. The spring stiffness listed in Table A.1-1 was taken from the catalogue of the company.

Spring Code	K1	K2	K3	K4	K5	K6	K7	K8	K9	K10
Linear Stiffness K_s (N/m)	49	119	214	306	806	1051	1751	2242	2594	3399

Table A.1-1 Spring linear stiffness specified by manufacturer.

All springs were suitable to be used for a speed range from 0 m/s to 10 m/s. However the springs that can be used up to 40 m/s were K5, K6, K7, K8, K9 and K10.

A.1.2 Wind-Off Measurements Using Disc and 20° Slant Model

Figure A.1-1 shows the 20° slant model mounted from the roof of the working section, looking upstream.
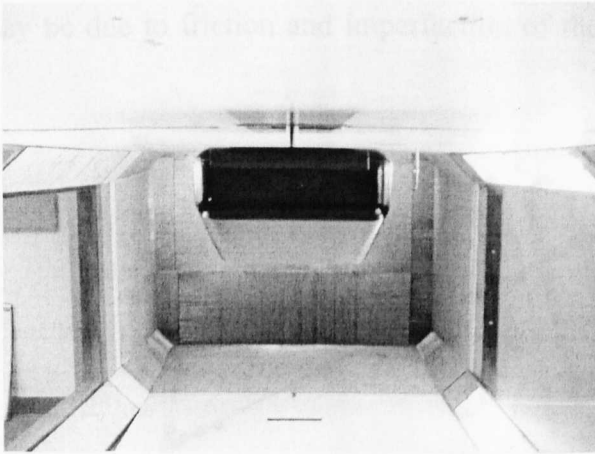
Figure A.1-1 Model mounted from the roof looking up-stream (20° slant model).

The 20° slant model was replaced with a circular disc of 108 mm diameter shown in Figure A.1-2 which enables the measurement of the mechanical properties of the rig. The total weight of the rotating mass (i.e. disc, rod, cross-arm etc) is 5.915 kg.
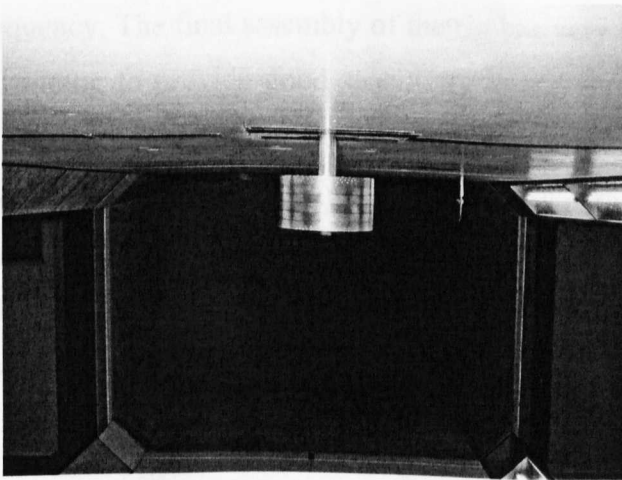
Figure A.1-2 Test using rotating disc to study the mechanical properties of the oscillating rig. The total weight of the rotating mass is 5.915 kg.

Figure A.1-3 shows the gradients of the plots used to determine the moment inertia of the disc and the 20° slant model, which are 0.1013 kgm^2 and 0.0098 kgm^2 respectively. For that, the ratio of $\dfrac{I_{model}}{I_{disc}} = \left(\dfrac{f_{d\,disc}}{f_{d\,model}}\right)^2 = \dfrac{0.1013}{0.0098} \approx 10.3367$

The calculated moment of inertia of the disc by standard formula is:

$$I_{disc} = \tfrac{1}{2}mr^2 = \tfrac{1}{2}(5.915)(0.054)^2 \approx 0.0086 \ \text{kgm}^2$$

The measured moment of inertia is of the order of the theoretical value and the discrepancy may be due to friction and imperfection of the mass distribution of the rotating disc.
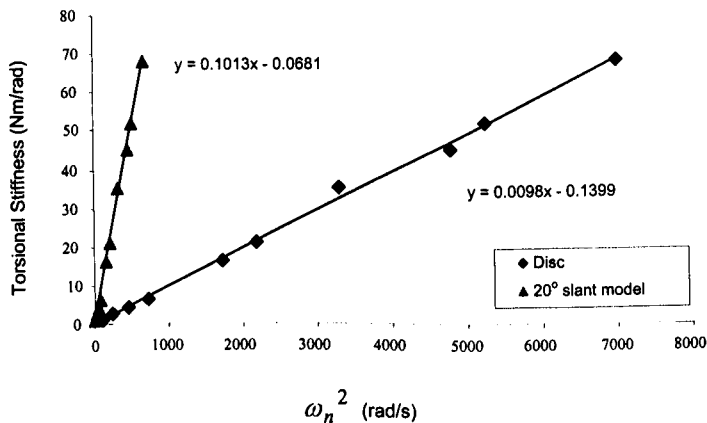
Figure A.1-3 Torsional stiffness against square of wind-off natural frequency of 20° slant model and disc.

Figure A.1-4 shows the wind-off damping ratio for 20° slant model and disc versus oscillation frequency. The final assembly of the rig has very low wind-off mechanical friction and damping to provide good sensitivity to the aerodynamic damping. This improves the accuracy of the estimation of the aerodynamic damping derivative Cn_r. At low frequency (i.e. less than 1 Hz) the measured damping ratio is less than 0.03 and rapidly dropped to less than 0.005 at higher frequency (i.e. more than 1 Hz). It was observed that from the wind-on tests the oscillation frequency of the disc is not affected by the wind speed even at 40 m/s.
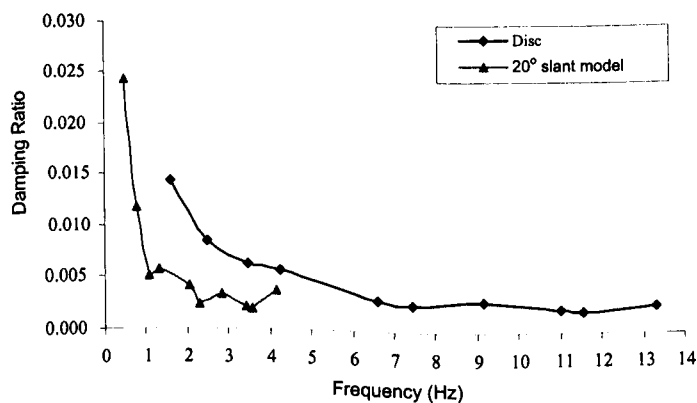
Figure A.1-4 Measured damping ratio for a disc compared to 20° slant model.

A.1.3 Repeatability of Wind–off Data with 20° Slant Model

Figure A.1-5 shows the repeatability of damped frequency versus spring stiffness from two repeat tests (February and April 2004).
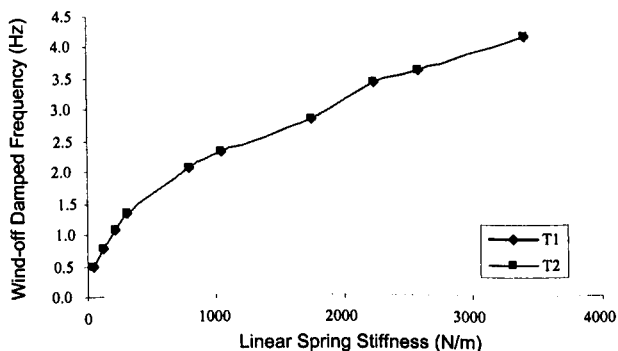
Figure A.1-5 Wind-off damped frequency versus spring stiffness of two repeat tests.

Figure A.1-6 shows the repeatability of the measurement is also very good between two repeat tests. The natural frequency matched the damped frequency due to the very small damping ratio.
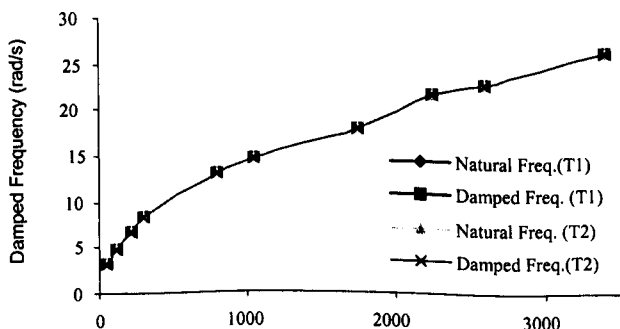
Figure A.1-6 Repeatability of damped and natural frequency of two repeat tests. The natural frequency matched the damped frequency due to the very small damping ratio.

A.1.4 Uncertainty of Measurement Using Disc

Wind-off measurements using circular disc to analyse the mechanical properties and the precision measurement of the oscillating rig.

Data	Disc - Spring K1			Disc - Spring K2			Disc - Spring K3		
	fd (Hz)	ς	$T_{1/2}$ (s)	fd (Hz)	ς	$T_{1/2}$ (s)	fd (Hz)	ς	$T_{1/2}$ (s)
1	1.5913	0.0142	4.8911	2.5089	0.0081	5.4336	3.4538	0.0064	4.9899
2	1.5951	0.0142	4.8751	2.5088	0.0082	5.3713	3.4562	0.0065	4.9097
3	1.6148	0.0145	4.7249	2.5119	0.0086	5.1158	3.4597	0.0066	4.7716
4	1.5884	0.0161	4.3263	2.5132	0.0086	5.0887	3.4548	0.0057	5.6421
5	1.5930	0.0124	5.5834	2.5173	0.0083	5.3104	3.4622	0.0065	4.9016
average	1.5965	0.0143	4.8802	2.5120	0.0084	5.2640	3.4573	0.0063	5.0430
standard deviation	0.0101	0.0013	0.4543	0.0031	0.0002	0.1231	0.0029	0.0004	0.3427
standard deviation (%)	0.6334	9.1976	9.3083	0.1222	2.1637	2.3381	0.0849	5.7288	6.7956
standarad error	0.0041	0.0005	0.1855	0.0013	0.0001	0.0502	0.0012	0.0001	0.1399

Table A.1-2 Wind-off repeatability tests with disc. Spring K1, K2 and K3.

Data	Disc - Spring K4			Disc - Spring K5			Disc - Spring K6		
	fd (Hz)	ς	$T_{1/2}$ (s)	fd (Hz)	ς	$T_{1/2}$ (s)	fd (Hz)	ς	$T_{1/2}$ (s)
1	4.2776	0.0064	4.0052	6.6079	0.0033	5.0793	7.4288	0.003	4.9709
2	4.2652	0.0062	4.1862	6.6118	0.003	5.5367	7.4336	0.0025	5.8839
3	4.2636	0.0054	4.8064	6.6132	0.003	5.6150	7.4333	0.0024	6.1881
4	4.2673	0.0058	4.4729	6.6065	0.0029	5.6900	7.4320	0.0022	6.7249
5	4.2584	0.0048	5.4108	6.5795	0.0028	6.0035	7.4169	0.0024	6.1195
average	4.2664	0.0057	4.5763	6.6038	0.0030	5.5849	7.4289	0.0025	5.9775
standard deviation	0.0035	0.0005	0.4602	0.0137	0.0001	0.1860	0.0070	0.0001	0.3276
standard deviation (%)	0.0825	9.1392	10.0552	0.2069	2.9814	3.3303	0.0940	4.8990	5.4809
standarad error	0.0014	0.0002	0.1879	0.0056	0.0000	0.0759	0.0029	0.0000	0.1337

Table A.1-3 Wind-off repeatability tests with disc. Spring K4, K5 and K6.

Data	Disc - Spring K7			Disc - Spring K8			Disc - Spring K9		
	fd (Hz)	ς	$T_{1/2}$ (s)	fd (Hz)	ς	$T_{1/2}$ (s)	fd (Hz)	ς	$T_{1/2}$ (s)
1	9.1234	0.0034	3.5309	11.0341	0.0023	4.3577	11.5224	0.0019	4.9903
2	9.1286	0.0031	3.8643	11.0330	0.0023	4.3734	11.5190	0.002	4.9080
3	9.1295	0.0029	4.1003	11.0351	0.0023	4.3996	11.5299	0.0019	5.0392
4	9.1279	0.0028	4.2975	10.9727	0.0018	5.5896	11.5698	0.0023	4.0983
5	9.1520	0.0026	4.6540	10.9984	0.0023	4.3769	11.5353	0.0020	4.7590
average	9.1323	0.0030	4.0894	11.0147	0.0022	4.6194	11.5353	0.0020	4.7590
standard deviation	0.0102	0.0002	0.2960	0.0260	0.0002	0.5233	0.0191	0.0001	0.3628
standard deviation (%)	0.1113	6.3131	7.2384	0.2360	9.8543	11.3273	0.1652	7.3558	7.6236
standarad error	0.0042	0.0001	0.1208	0.0106	0.0001	0.2136	0.0078	0.0001	0.1481

Table A.1-4 Wind-off repeatability tests with disc. Spring K7, K8 and K9.

	Disc- Spring K10		
Data	fd (Hz)	ς	$T_{1/2}$ (s)
1	13.3359	0.0023	3.6692
2	13.3360	0.0023	3.6673
3	13.3111	0.0028	2.9147
4	13.2838	0.0025	3.2954
5	13.3553	0.0025	3.3867
average	13.3244	0.0025	3.3867
standard deviation	0.0269	0.0002	0.2710
standard deviation (%)	0.2017	7.3049	8.0033
standarad error	0.0110	0.0001	0.1107

Table A.1-5 Wind-off repeatability tests with disc. Spring K10.

The oscillation frequency is unaffected by the tunnel speed, even with the softest spring of K1, the results shows in Table. A.1-6.

Wind Speed (m/s)	fd (Hz)	ς	$T_{1/2}$ (s)
0	1.5913	0.0142	4.8911
10	1.6077	0.0126	5.4349
20	1.6071	0.0126	5.4549
30	1.5995	0.0132	5.2317
40	1.6063	0.0134	5.1408

Table A.1-6 Wind-on tests with disc has no effect with tunnel speed even with Spring K1.

Appendix B

B.1 Calculation of Scaling Factor

Calculation of Wind Tunnel Model and Scaling Factors

Author: Shuhaimi Mansor, Loughborough University, UK.

Constants

sea level air density (kg/m^3) $\rho := 1.225$ dynamic viscosity (Ns/m^2) $\mu := 1.7894\,10^{-5}$

kinematic viscosity (m^2/s) $v := \dfrac{\mu}{\rho}$ gravity acceleration (m/s^2) $g := 9.81$

Dimension of Working Section   Model Specifications

Tunnel width (m) $Wt := 1.92$ model width (m) $Wm := 0.225$
Tunnel height (m) $Ht := 1.32$ model height (m) $Hm := 0.160$
Tunnel area (m^2) $At := Wt \cdot Ht$ model length (m) $Lm := 0.625$
         $At = 2.534$ height above ground (m) $hm := 0.040$
                            estimated model weight (kg) $Mm := 3$
                            model frontal area (m^2) $Am := Wm \cdot Hm$
                                            $Am = 0.036$

estimated model moment of inertia (kgm^2) $Im := \left(\dfrac{1}{12}\right) \cdot Mm \cdot \left(Wm^2 + Lm^2\right)$ $Im = 0.11$

model side area (m^2) $As := (0.5 \cdot Hm \cdot 0.343) + (0.06 \cdot 0.16) + [0.5 \cdot 0.222 \cdot (0.075 + Hm)]$ $As = 0.063$

Frequency of Interest (Hz)	Lower Limit $fal := 0.2$	Upper Limit $fau := 2$
Motorway Speed (m/s)	$Ua := 30$	
Vehicle Characteristic Length (m)	$La := 4.5$	
Reynold's number	$Rea := \dfrac{(\rho \cdot Ua \cdot La)}{\mu}$	$Rea = 9.242 \times 10^6$
Lower limit vehicle reduced frequency	$Kml := \dfrac{(\pi \cdot fal \cdot La)}{Ua}$	$Kml = 0.09$
Upper limit vehicle reduced frequency	$Kmu := \dfrac{(\pi \cdot fau \cdot La)}{Ua}$	$Kmu = 0.94$
Model blockage (%)	$B := \left(\dfrac{Am}{At}\right) \cdot 100$	$B = 1.4\%$
Working section wind speed (m/s)	$Um := 10, 20 .. 40$	
Model Reynolds number	$Re_{Um} := \dfrac{(\rho \cdot Um \cdot Lm)}{\mu}$	

$Um =$	$Re_{Um} =$
10	$4.279 \cdot 10^5$
20	$8.557 \cdot 10^5$
30	$1.284 \cdot 10^6$
40	$1.711 \cdot 10^6$

Model frequencies in order to achieve the equivalent reduced frequency

Lower limit $fml_{Um} := \dfrac{(Um \cdot Kml)}{\pi \cdot Lm}$ Upper limit $fmu_{Um} := \dfrac{(Um \cdot Kmu)}{\pi \cdot Lm}$

Um =	$Re_{Um} =$	$fml_{Um} =$	$fmu_{Um} =$
10	$4.2787 \cdot 10^5$	0.48	4.8
20	$8.5573 \cdot 10^5$	0.96	9.6
30	$1.2836 \cdot 10^6$	1.44	14.4
40	$1.7115 \cdot 10^6$	1.92	19.2

Model oscillation frequency range (Hz) $fm := 0.5, 1 .. 5$

Equivalent Torsional Stiffness and Damping

To calculate the range of torsional stiffness required to achieve the test frequency range. The rig should be designed to have very small damping ratio.

Damping Ratio $\zeta := 0.05$

Cross-arm length $b := 0.1$ m

Frequency of the model $\omega n(fm) := 2 \cdot \pi \cdot fm$ rad/s

Rig Torsional Stiffness $Kr(fm) := Im \cdot (\omega n(fm))^2$ Nm/rad

Rig Torsional Damper $C(fm) := 2 \cdot \zeta \cdot \omega n(fm) \cdot Im$ Nms/rad

Linear Spring Stiffness Required $Ks(fm) := \dfrac{Kr(fm)}{2 \cdot b^2}$

Reduced Frequency at Various Tunnel Speed

$U10 := 10$ $U20 := 20$ $U30 := 30$ $U40 := 40$

$Km10(fm) := \dfrac{\pi \cdot fm \cdot Lm}{U10}$ $Km20(fm) := \dfrac{\pi \cdot fm \cdot Lm}{U20}$ $Km30(fm) := \dfrac{\pi \cdot fm \cdot Lm}{U30}$ $Km40(fm) := \dfrac{\pi \cdot fm \cdot Lm}{U40}$

fm =	$Kr(fm) =$	$Ks(fm) =$	$Km10(fm) =$	$Km20(fm) =$	$Km30(fm) =$	$Km40(fm) =$
0.5	1.09	54.44	0.1	0.05	0.033	0.02
1	4.35	217.75	0.2	0.1	0.065	0.05
1.5	9.8	489.93	0.29	0.15	0.098	0.07
2	17.42	870.99	0.39	0.2	0.131	0.1
2.5	27.22	1360.93	0.49	0.25	0.164	0.12
3	39.19	1959.73	0.59	0.29	0.196	0.15
3.5	53.35	2667.41	0.69	0.34	0.229	0.17
4	69.68	3483.97	0.79	0.39	0.262	0.2
4.5	88.19	4409.4	0.88	0.44	0.295	0.22
5	108.87	5443.7	0.98	0.49	0.327	0.25

B.2 Design of the Oscillating Rig

Mechanical Engineering Design Calculation

Linear Spring Stiffness, Applied Force and Torque

The schematic of pure-yaw and balance experiment is shown below
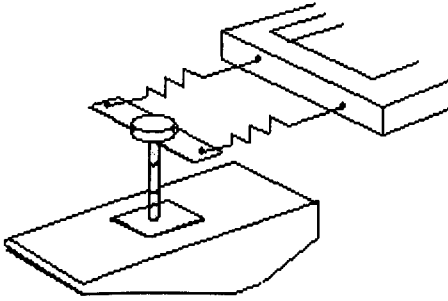
The free-body diagram of the vibration system of pure-yaw motion is shown below
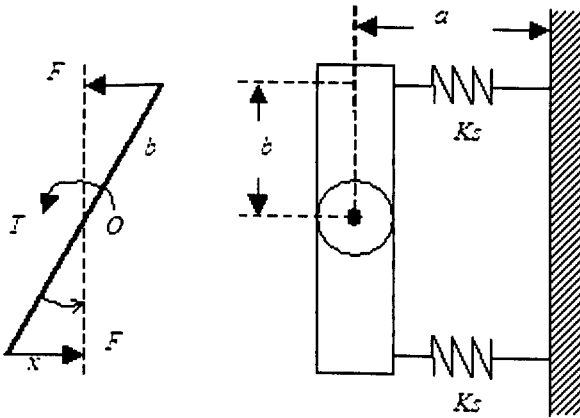
$\Sigma Mo = 0;$ $T = 2\ F\ b = 2\ Ks\ b$ $\Delta x = 2\ Ks\ b\ b\sin\beta = 2\ Ks\ b^2\beta$

Torsional stiffness, $Kr = T\ /\beta = 2\ F\ b\ /\beta = 2\ Ks\ b^2$

Then the linear spring stiffness, $Ks = Kr\ /\ 2\ b^2$

Maximum torsional stiffness required, Ks $Kr(5) = 108.874$ Nm/rad   (at 5 Hz)

Moment arm (m) $b := 0.1$

Arm angle (rad) $\beta := 20 \cdot \dfrac{\pi}{180}$

Linear stiffness (N/m) $Ks := \dfrac{Kr(5)}{2 \cdot b^2}$ $Ks = 5444$

Spring torque (Nm) $T := 2 \cdot Ks \cdot b^2 \cdot \sin(\beta)$ $T = 37.237$

Spring force (N) $F := \dfrac{T}{2 \cdot b}$ $F = 186.186$

Back calculation to check validity of answers

Spring extension (m) $\Delta x := b \cdot \sin(\beta)$ $\Delta x = 0.034$

Maximum spring force at the end of joints (N) $Fs := Ks \cdot \Delta x$ $Fs = 186$

Maximum spring torque (Nm) $Ts := 2Fs \cdot b$ $Ts = 37.237$

$Ts = I \, (d^2\beta/dt^2)$
$-2 \, (Ks)(\beta) = I\beta$
$-2 \, (Ks)(b)(b\sin\beta) = I \, (d^2\beta/dt^2)$
$I \, (d^2\beta/dt^2) + 2 \, Ks \, b^2 \, \beta = 0$
$(d^2\beta/dt^2) + (2 \, Ks \, b^2/I) \, \beta = 0$

$Ks := 49$ Spring linear stiffness (N/m)

$Izz := 0.1012$ Moment of Inertia (kgm^2)

$\zeta := 0.05$ Mechanical damping ratio

Natural Freq. (Hz) $\omega n := \sqrt{\dfrac{2 \cdot Ks \cdot b^2}{Izz}}$ $fn := \dfrac{\omega n}{2 \cdot \pi}$ $fn = 0.4953$ Hz

Damped Freq. (Hz) $\omega d := \omega n \cdot \sqrt{1 - \zeta^2}$ $fd := \dfrac{\omega d}{2 \cdot \pi}$ $fd = 0.4947$ Hz

Sample Calculation From Experimental Data

Measured oscillation period $To := 1.2610$ sec

Measured time half amplitude $t05 := 7.6$ sec

Measured damped frequency $fd := \dfrac{1}{To}$ $fd = 0.793$ Hz

Natural frequency $\omega n2 := \left(\dfrac{4 \cdot \pi^2}{To^2} \right) + \left(\dfrac{0.6931}{t05} \right)^2$ (rad/s)^2

$\omega n := \sqrt{\omega n2}$ $\omega n = 4.9835$ rad/s

$fn := \dfrac{\sqrt{\omega n}}{2 \cdot \pi}$ $fn = 0.355$ Hz

Measured Damping ratio $\zeta := \dfrac{\left(\dfrac{1.3863}{t05} \right)}{2 \cdot \omega n}$ $\zeta = 0.0183$

Estimation of Bluff Body Transient Aerodynamic Loads Using an Oscillating Model Rig

Structural Analysis for Strut and Plate Mounting

Constants

$Ls := 0.300$ shaft length (m)
$ds := 0.020$ shaft diameter (m)
$Lm := 0.625$ model length (m)
$m := 5$ model weight (kg)
$Af := 0.036$ model frontal area (m^2)
$As := 0.063$ model side area (m^2)
$U := 40$ wind speed (m/s)
$\rho := 1.23$ air density (kg/m^3)
$CD := 0.5$ drag coefficient of model
$CL := 0.30$ drag coefficient of model
$Cy\beta := 4.00$ side force derivative (rad^1)
$Cn\beta := 0.60$ yawing moment derivatives (rad^1)
$c := ds$ torsional moment length (m)
$r := \dfrac{ds}{2}$ shaft radius (m)
$\beta := 20 \cdot \dfrac{\pi}{180}$ yaw angle (rad)
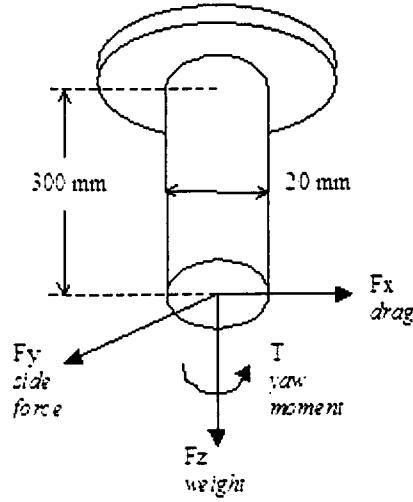
$Fx := 0.5 \cdot \rho \cdot U^2 \cdot Af \cdot CD$ $Fx = 17.712$ N

$Fy := 0.5 \cdot \rho \cdot U^2 \cdot As \cdot Cy\beta \cdot \beta$ $Fy = 86.557$ N

$Fz := m \cdot g + 0.5 \cdot \rho \cdot U^2 \cdot Af \cdot CL$ $Fz = 59.677$ N

$T := 0.5 \cdot \rho \cdot U^2 \cdot Af \cdot \dfrac{Lm}{2} \cdot Cn\beta \cdot \beta$ $T = 2.318$ Nm

Resultant force $F := \sqrt{Fx^2 + Fy^2}$ $F = 88.351$ N

Maximum bending moment $M := Ls \cdot F$ $M = 26.505$ Nm

Shaft area $A := \dfrac{\pi \cdot ds^2}{4}$ $A = 0.000314$ m^2

Shaft second moment area $I := \dfrac{\pi \cdot ds^4}{32}$ $I = 1.571 \times 10^{-8}$ m^4

Bending Stress $\sigma := \dfrac{Fz}{A} + \dfrac{M}{\left(\dfrac{I}{c}\right)}$ $\sigma = 3.394 \times 10^7$ N/m^2

Polar Moment $J := \dfrac{\pi \cdot ds^4}{16}$ $J = 3.142 \times 10^{-8}$ m^4

Torsional Stress $\tau := \dfrac{T}{\left(\dfrac{J}{r}\right)}$ $\tau = 7.38 \times 10^5$

Maximum Shear stress theory based on Mohr's Circle Diagram

$$\tau max := \left[\left(\frac{\sigma}{2} \right)^2 + \tau^2 \right]^{\frac{1}{2}} \qquad \tau max = 1.698 \times 10^7$$

Steel yield stress $\tau ymin := 280 \times 10^6$ $\tau ymax := 1600 \times 10^6$

Minimum Safety factor $SFmin := \dfrac{\tau ymin}{\tau max}$ $SFmin = 16.485$

Maximum Safety factor $SFmax := \dfrac{\tau ymax}{\tau max}$ $SFmax = 94.202$

Shear Connections

Shear force (N) $F = 88.351$
Bolt diameter (m) $d := 0.006$
No.of bolts $n := 4$

Bolt cross-section area (m²) $A := \dfrac{\pi \cdot d^2}{4}$

Average shear Stress (N/m²) $\tau ave := \dfrac{F}{n \cdot A}$

$$\tau ave = 7.812 \times 10^5$$

Safety Factor $SF := \dfrac{\tau ymax}{\tau ave}$

$$SF = 2.048 \times 10^3$$
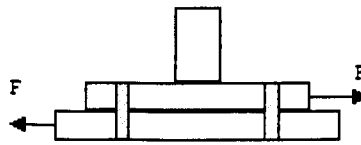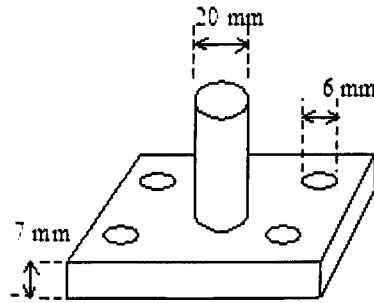
Coil Spring Rate

Modulus of Rigidity $G := 79.3 \times 10^3$ N/mm²

Mean Coil Diameter $D := 1.45$ mm

Wire Diameter $d := 0.15$ mm

Number of Coil $N := 29$ mm

Spring Rate $K := \dfrac{G \cdot d^4}{8 \cdot D^3 \cdot N}$ $K = 0.057$ N/mm

Note: **Mechanical strength properties**

Materials	Yields Stress(MPa)	Ultimate Stress(MPa)	Elongation(%)
Aluminum	20	70	60
Aluminum alloy	35-500	100-500	1-45
Steel	280-1600	340-1900	3-40
Iron (cast)	120-290	69-480	0-1
Iron (Wrought)	210	340	35

Appendix C

C.1 Vehicle Lateral Dynamics

The dynamic response of a vehicle to wind disturbance is governed by its aerodynamic derivatives coupled with the suspension and tyre characteristics. The equation of motion of a car can be formed by equating the inertial reaction to the external forces. Assuming that the car is moving at a steady forward speed, u without pitching and rolling movements and the results are considered by the yaw and sideslip, Milliken [46], Russell [57] and Scibor-Rylsky [62]. Assembling the inertial characteristics and forces in derivative form, then the steering wheel input δ and yaw angle input β is given as follows,

$$m(\dot{v} + ur) = Y_{\beta c}\beta + Y_{rc}r + Y_{\delta c}\delta + Y_A$$
$$I_{zz}\dot{r} = N_{\beta c}\beta + N_{rc}r + N_{\delta c}\delta + N_A$$

$$(C.1\text{-}1)$$

where $\dot{v}$ lateral acceleration, r yaw rate and $\dot{r}$ yaw acceleration. The Y_A and N_A is the aerodynamic side force and yaw moment respectively which can expressed as follows,

$$Y_A = Y_\beta(\beta - \beta w) + Y_r r$$
$$N_A = N_\beta(\beta - \beta w) + N_r r$$

$$(C.1\text{-}2)$$

Where Y_β, N_β are the dimensional static stability derivatives, while Y_r and N_r are the dimensional dynamic stability derivatives and β_w is the crosswind yaw angle. The dimensional expressions for all the derivatives are given below.

$$Y_\beta = \tfrac{1}{2}\rho u^2 A C_{y_\beta} \qquad N_\beta = \tfrac{1}{2}\rho u^2 A\ell C_{n_\beta}$$
$$Y_r = \tfrac{1}{2}\rho u A\ell C_{y_r} \qquad N_r = \tfrac{1}{2}\rho u A\ell^2 C_{n_r}$$

$$(C.1\text{-}3)$$

Substituting Equation (C.1-2) into Equation (C.1-1) and rearrange, yields,

$$m(\dot{v} + ur) = (Y_{\beta c} + Y_\beta)\beta + (Y_{rc} + Y_r)r + Y_{\delta c}\delta - Y_\beta\beta w$$
$$I_{zz}\dot{r} = (N_{\beta c} + N_\beta)\beta + (N_{rc} + N_r)r + + N_{\delta c}\delta - N_r\beta w$$

$$(C.1\text{-}4)$$

The side speed v can be defined as body aerodynamic yaw angle β, for small angle $\beta = \dfrac{v}{u}$ then $v = u\beta$, for that the derivative of v becomes $\dot{v} = u\dot{\beta} + \dot{u}\beta$. For steady motion, $\dot{u} = 0$, then $\dot{v} = u\dot{\beta}$

$$mu\dot{\beta} = (Y_{\beta c} + Y_\beta)\beta + (Y_{rc} + Y_r - mu)r + Y_{\delta c}\delta - Y_\beta \beta w$$

$$I_{zz}\dot{r} = (N_{\beta c} + N_\beta)\beta + (N_{rc} + N_r)r + N_{\delta c}\delta - N_r \beta w$$

$$(C.1-5)$$

The above equation can be simplified to become a reduced order model of yawing motion as follows;

$$
\begin{bmatrix} \dot{\beta} \\ \dot{r} \end{bmatrix} =
\begin{bmatrix}
\dfrac{Y_{\beta c} + Y_\beta}{mu} & \dfrac{Y_{rc} + Y_r}{mu} - 1 \\[3mm]
\dfrac{N_{\beta c} + N_\beta}{I_{zz}} & \dfrac{N_{rc} + N_r}{I_{zz}}
\end{bmatrix}
\begin{bmatrix} \beta \\ r \end{bmatrix} +
\begin{bmatrix}
\dfrac{Y_{\delta c}}{mu} & -\dfrac{Y_\beta}{mu} \\[3mm]
\dfrac{N_{\delta c}}{I_{zz}} & -\dfrac{N_\beta}{mu}
\end{bmatrix}
\begin{bmatrix} \delta \\ \beta w \end{bmatrix}
$$

$$(C.1-6)$$

The above equation is in the form of state-space equation and can written as, $\dot{x}(t) = Ax(t) + Bu(t)$. The transfer function due to crosswind βw (i.e. $\dfrac{\beta}{\beta w}$ and $\dfrac{r}{\beta w}$) can be derived using the expression, $(sI - A)^{-1}.B = \dfrac{adj|sI - A|}{det|sI - A|}.B$. For zero steering angle, putting $\delta = 0$, yields

$$
\begin{bmatrix} \dfrac{\beta}{\beta w} \\[3mm] \dfrac{r}{\beta w} \end{bmatrix} =
\begin{bmatrix}
s - \dfrac{Y_{\beta c} + Y_\beta}{mu} & \dfrac{Y_{rc} + Y_r}{mu} + 1 \\[3mm]
-\dfrac{N_{\beta c} + N_\beta}{I_{zz}} & s - \dfrac{N_{rc} + N_r}{I_{zz}}
\end{bmatrix}^{-1}
\begin{bmatrix} -\dfrac{Y_\beta}{mu} \\[3mm] -\dfrac{N_\beta}{I_{zz}} \end{bmatrix}
$$

$$(C.1-7)$$

$$
\begin{bmatrix} \dfrac{\beta}{\beta w} \\[3mm] \dfrac{r}{\beta w} \end{bmatrix} =
\dfrac{
\begin{bmatrix}
s - \dfrac{N_{rc} + N_r}{I_{zz}} & \dfrac{Y_{rc} + Y_r}{mu} - 1 \\[3mm]
\dfrac{N_{\beta c} + N_\beta}{I_{zz}} & s - \dfrac{Y_{\beta c} + Y_\beta}{mu}
\end{bmatrix}
\begin{bmatrix} -\dfrac{Y_\beta}{mu} \\[3mm] \dfrac{-N_\beta}{I_{zz}} \end{bmatrix}
}{
\left[s - \dfrac{N_{rc} + N_r}{I_{zz}} \right]\left[s - \dfrac{Y_{\beta c} + Y_\beta}{mu} \right] - \left[\dfrac{N_{\beta c} + N_\beta}{I_{zz}} \right]\left[\dfrac{Y_{rc} + Y_r - mu}{mu} \right]
}
$$

$$(C.1-8)$$

The system transfer functions are given by:

$$
\begin{bmatrix} \dfrac{\beta}{\beta w} \\[3mm] \dfrac{r}{\beta w} \end{bmatrix} =
\dfrac{
\begin{bmatrix}
-\dfrac{Y_\beta}{mu}s + \dfrac{(N_{rc} + N_r)Y_\beta}{I_{zz}mu} - \dfrac{(Y_{rc} + Y_r)N_\beta}{mu I_{zz}} + \dfrac{N_\beta}{I_{zz}} \\[4mm]
-\dfrac{N_\beta}{I_{zz}}s + \dfrac{(Y_{\beta c} + Y_\beta)N_\beta}{I_{zz}mu} - \dfrac{(N_{\beta c} + N_\beta)Y_\beta}{mu I_{zz}}
\end{bmatrix}
}{
s^2 - \left[\dfrac{N_{rc} + N_r}{I_{zz}} + \dfrac{Y_{\beta c} + Y_\beta}{mu} \right]s - \left[\dfrac{N_{\beta c} + N_\beta}{I_{zz}} \right]\left[\dfrac{Y_{rc} + Y_r - mu}{mu} \right] + \left[\left(\dfrac{N_{rc} + N_r}{I_{zz}} \right)\left(\dfrac{Y_{\beta c} + Y_\beta}{mu} \right) \right]
}
$$

$$(C.1-9)$$

C.2 Crosswind Angles and Resultant

If the vehicle initially travel at forward speed u with zero yaw angle (i.e. $w=0$), suddenly experiences a crosswind V_w coming at an angle of ψ with the vehicle forward speed, the resultant relative wind speed V_R can be deduced from the vector diagram from Figure C.1-1.
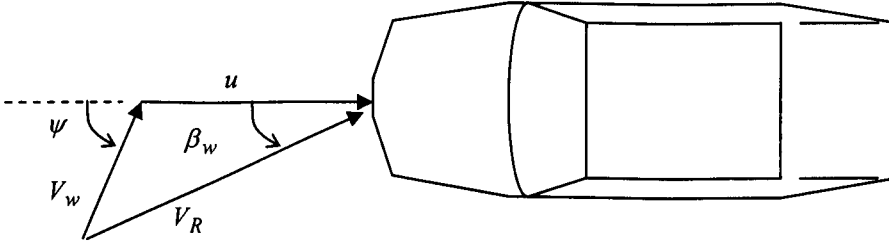
Figure C.1-1 Crosswind angles and resultant.

Where, u vehicle speed
             V_w crosswind speed
             V_R relative speed
             β_w relative crosswind angle
             ψ crosswind angle

The equation for relative speed is given by,

$$V_R{}^2 = (u + V_w \cos\psi)^2 + (V_w \sin\psi)^2 = u^2 + 2uV_w \cos\psi + V_w{}^2 \cos^2\psi + V_w{}^2 \sin^2\psi$$

$$V_R = \sqrt{u^2 + 2uV_w \cos\varphi + V_w{}^2} \qquad\qquad (C.1\text{-}10)$$

The wind yaw angle is given by,

$$\beta_w = \tan^{-1}\frac{V_w \sin\psi}{V_w \cos\psi + u} \qquad\qquad (C.1\text{-}11)$$

For example if $\psi = 90^o$ (i.e. direction of V_w is perpendicular to vehicle forward speed u), then the resultant speed V_R and the wind yaw angle β_w is given by,

$$V_R = \sqrt{u^2 + V_w{}^2} \qquad\qquad (C.1\text{-}12)$$

$$\beta_w = \tan^{-1}\frac{V_w}{u} \qquad\qquad (C.1\text{-}13)$$

Appendix D

D.1 Matlab Codes

```
%_____
% FILPSD.M
%
% M-file used to process the oscillation data. Outputs from the program are the peak amplitude of
% power spectral and correspondence frequency, time to half amplitude, time response, power spectral plots.
%
% Author: Shuhaimi Mansor, Loughborough University, UK. (2006)
%
sr=1000;                          % sampling rate (Hz)
path(path,'c:\phd\dyntest')
datafile=input('Filename= ','s');
load(datafile)
L=length(datafile);
filename=datafile(:,1:L-4);
rawdata=eval(filename);
row=length(rawdata);
maxpoint=row/2;
datcol=length(rawdata(1,:));      % check how many column in the data
if datcol > 1,
    rawyaw=rawdata(:,1);
else
    rawyaw=rawdata;
end
m=mean(rawyaw);                   % mean value
data0mean=rawyaw-m;              % zero mean
betadeg=data0mean*33;           % convert from volts to degrees
%
% Determine the suitable data points for damped oscillation
[betafilt,H,w]=filtdat(betadeg,1e-5,20,sr); % low-pass filter
ymax=max(round(betafilt));
yawinit=11;                       % initial yaw angle (deg)
%
if ymax < yawinit;
    yawinit=ymax;
else
    yawinit=yawinit;
end
yawfinal=1;                       % final yaw angle of decay
%
ndata=1:1:length(betafilt);       % data counts
beta=[ndata' round(betafilt)];    % setup data of yaw angle
% Determine initial data point
  colbetainit=round(betafilt)==yawinit;   % amplitudes equals yawinit
  locndatai=beta(colbetainit);            % list all angles equals to yawinit
  locni=max(locndatai);                   % last data represents yawinit
  betai=betafilt(locni);                  % initial yaw angle from data
% Determine final data point
  colbetafinal=round(betafilt)==yawfinal; % amplitudes equal yawfinal
  locndataf=beta(colbetafinal);           % list all angles equals to yawfinal
  locnf=max(locndataf);                   % last data represents yawfinal
  betaf=betafilt(locnf);                  % final yaw angle
%
if locni > maxpoint               % for self-sustained oscillation
    datapointi=maxpoint;
    datapointf=datapointi+maxpoint;
else
    datapointi=locni;             % for damped oscillation
    datapointf=locnf;
end
%
udecay=betafilt(datapointi:datapointf);
[ttos,tros,betaros,pvos,thalfos]=expdecay(udecay,sr,4);
%
% Determine the maximum point of sample data
if  thalfos > 0
    dmin=locni;                   % initial data for damped oscillation
    dmax=locnf;                   % final data for damped oscillation
```

```
else                                    % for self-sustained oscillation
   dmin=maxpoint;                       % initial data for self-sustained
   dmax=dmin+maxpoint;
   betai=std(betafilt);
end
%
% Find the primary dominant frequency in the time response data
uraw=betadeg(dmin:dmax);
ufilt=betafilt(dmin:dmax);
n=length(uraw);
tmax=n/sr;
t=0:1/sr:n/sr;
t=t(1:length(t)-1);
[praw fraw]=psd(uraw,n,sr);
[fmaxpsd maxpsd]=xymax(fraw,praw);      % frequency at maximum PSD
%
% Comparison Between Filtered and Raw PSD
S=fft(uraw,512);                        % fft the raw data
SF=fft(ufilt,512);                      % fft the filtered data
hz=(0:255)/256*(sr/2);                  % frequency range
%
```
_____

```
%
% FILTDAT.M
% Band-Limited-Filter (Elliptic or Cauer digital and analog filter design)
%
%        function [datafilt]=filtdat(data, lowf, highf, sr)
%           data     - data to filter and must be in single column
%           lowf     - low frequency cut-off (Hz)
%           highf    - high frequency cut-off (Hz)
%           sr       - sampling rate (Hz)

function [datafilt,H,w]=filtdat(data,lowf,highf,sr)
sr=1000;                                % sampling rate (Hz)
[b,a]=ellip(2,0.1,50,[lowf highf]*2/sr);
[H,w]=freqz(b,a,512);                   % low-pass filter bandwidth
datafilt=filter(b,a,data);              % filtered data
%
```
_____

```
%
% EXPDECAY.M
%
% Find peak amplitudes and registered time when they are occurred.
% Polynomial fitting the peak amplitude w.r.t time array in order to estimate the amplitude decay.
%
%function [tt,tr,betar,pv,thalf]=expdecay(d,sr,p)
%       where       sr  - sampling rate (Hz)
%                   d   - data (in single column)
%                   p   - polynomial order (try 4)

function [tt,tr,betar,pv,thalf]=expdecay(d,sr,p);
y=d';
n=length(y);
t=0:1/sr:n/sr;
t=t(1:length(t)-1);
nc=max(size(y));
j=2:nc-1;
% Find Positive Peaks
px=y(:,j-1) < y(:,j) & y(:,j+1) < y(:,j);
% Make Index of x equal p
qx=y(:,j);
% Display Peaks
peakx=qx(:,px);
% New Time Index
tt=t(:,j);
% Setup Data of Time and Responses
datax=[tt;qx];
% Setup Data of Time and Peak
locatex=datax(:,px);
% Calculation
tr=[0 locatex(1,:)];, betar=[max(locatex(2,:)) locatex(2,:)];
dat=[betar' tr'];
pn=polyfit(tr,betar,p);
pv=polyval(pn,tt);
thalf=interp1(pv,tt,max(locatex(2,:))/2);
```

_____

```
%_____
% XYMAX.M
%
% function [xatymax ymax]=xymax(x,y)
% To find x value at maximum value of y

function [xatymax, ymax]=xymax(x,y)
xydat=[x' y'];                    % data of x and y
ymax=max(y);                      % determine maximum y
locymax=y==max(y);                % locate the maximum y
locx=xydat(:,locymax);            % locate x for maximum y
xatymax=locx(1,1);                % print
%_____


%_____
% RMSPDF.M
%
% Calculate root-means-square, probability density function, kurtosis and skewness.
%
% function [er ez pdf rms sigma mew rmspsd p f]=RMSPDF(d,sr);
% Input:        d        - data (in single column)
%               sr       - sampling period (Hz)
% Output:       er       - deviation from mean
%               ez       - normalized deviation
%               pdf      - probability density function
%               rms      - root-mean-square
%               sigma    - standard deviation of rms of deviation
%               mew      - mean data
%               rmspsd   - rms of power spectral density
%               p        - power spectral
%               f        - frequency spectral

function [er,ez,pdf,RMS,sigma,mew,RMSPSD2,P,F,kurtos]=rmspdf(d,sr);
n=length(d);
mew=mean(d);                      % average value
er=d-mew;                         % deviation from mean
VAR=sum(er.^2)/n;                 % variance same as VAR=var(d)
sigma=sqrt(sum(er.^2)/n);         % standard deviation sigma=std(d)=std(er)
RMS=sqrt(sum(er.^2)/n);           % rms=sqrt(var(d)), rms=sigma if mew=0
ez=er./sigma;                     % normalized deviation (sigma=1)
% Probability Density Function
pdf=(1/sqrt(2*pi*sigma^2))*exp(-((d-mew).^2)/(2*sigma^2));
pdfez=(1/sqrt(2*pi*sigma^2))*exp((-ez.^2./2));  % pdf=pdfez
[P F]=psd(d,n,sr);
s1=10;                            % first data
s2=length(P);                     % last data
deltaF=F(2)-F(1);
RMSPSD1=sqrt(sum(P(s1:s2).^2)/s1-s2);
RMSPSD2=sum(P(s1:s2)*deltaF);
%skew=sum((d-mew).^3)/((length(d)-1)*sigma^3);
%kurtos=sum((d-mew).^4)/((length(d)-1)*sigma^4);
skew=skewness(d);                 % matlab command
kurtos=kurtosis(d);               % matlab command
%_____


%_____
% ENSEMBLE.M
% Ensemble Average
%
function [f,p,fav,pav,favatpmax,pavmax,D,pdf,SD]=ensemble(u,elements,sr)

dpoints=length(u); % use data points from FILPSD.M to check no. of rows
sp=round(dpoints/elements);                    % number of blocks
i=0;
j=1:elements;
for count=0:sp-2,
    i=i+1;
    D(j,i)=u(count*elements+1:(count+1)*elements); % setup data blocks
    M(i)=mean(D(j,i));                % mean value
    DE(j,i)=D(j,i)-M(i);             % deviation from mean
    SD(i)=std(DE(j,i));              % standard deviation
    pdf(j,i)=(1./sqrt(2*pi*SD(i).^2))*exp(-((D(j,i)-M(i)).^2)./(2*SD(i).^2));
    Z(j,i)=DE(j,i)./SD(i);
    pdfZ(j,i)=(1./sqrt(2*pi*SD(i).^2))*exp(-((Z(j,i)).^2)./2);
end
```

```
%
colsize=size(D);
col=colsize(:,2);
for c=1:col;
    [p(:,c),f(:,c)]=psd(D(:,c),length(D),sr);
end
%
% Ensemble average of n-blocks
pav=sum(p,2)/col;  % is equals to pav=(p(:,1)+p(:,2)+,...p(:,n))/col;
fav=sum(f,2)/col;
[favatpmax pavmax]=xymax(fav, pav);
%_____
```

```
%_____
% CNBCNR.M
% Program to calculate yaw moment and yaw damping derivatives.

close all
U=input('Wind Speed (m/s)= ');
rho=input('Air Density (kg/m^3)= ');
Izz=input('Model Moment of Inertia (kgm^2)= ');
%
Am=0.036;                          % model frontal area
Lm=0.625;                          % model length
p=4;                               % curve-fit polynomial order
%
% Wind-Off
disp('Wind-Off Filename: ')
filpsd
yo=ufilt;
fdo=fmaxpsd;
[tto,tro,betaro,pvo,thalfo]=expdecay(yo,sr,p);
wno=sqrt((4*pi^2*fdo^2)+(log(2)/thalfo)^2);
zetao=(2*log(2)/thalfo)/(2*wno);
%
% Wind-On
disp('Wind-On Filename: ')
filpsd
y=ufilt;
fd=fmaxpsd;
[tt,tr,betar,pv,thalf]=expdecay(y,sr,p);
wn=sqrt((4*pi^2*fd^2)+(log(2)/thalf)^2);
zeta=(2*log(2)/thalf)/(2*wn);
%
% Estimated Cnbeta and Cnr using frequency ratio and time to half amplitude
if thalf > 0
    Nbeta=-(4*pi^2*fdo^2*((fd/fdo)^2-1)+log(2)^2*((1/thalf^2)-(1/thalfo^2)));
    Nr=-2*log(2)*((1/thalf)-(1/thalfo));
else
    Nbeta=-(4*pi^2*fdo^2*((fd/fdo)^2-1)+log(2)^2*((1/1e10000)-(1/thalfo^2)));
    Nr=-2*log(2)*((1/1e10000)-(1/thalfo));
end
Cnbeta_dyn=(Nbeta*Izz)/(0.5*rho*U^2*Am*Lm);
Cnr_dyn=(Nr*Izz)/(0.5*rho*U^2*Am*Lm*(Lm/U));
%
results=[fdo zetao fd zeta Cnbeta_dyn Cnr_dyn];
disp('   fdo    zetao    fd     zeta   Cnbeta    Cnr')
fprintf('%10.4f',results)
```